2010

Development Of Digital Diagnostics And Measurement Tools For A High Heat Flux Thermal Loop

Jr. Rodward Hewlin

North Carolina Agricultural and Technical State University.

Recommended Citation

Hewlin, Jr. Rodward, "Development Of Digital Diagnostics And Measurement Tools For A High Heat Flux Thermal Loop" (2010). *Theses*. 29.

https://digital.library.ncat.edu/theses/29

DEVELOPMENT OF DIGITAL DIAGNOSTICS AND MEASUREMENT TOOLS FOR A HIGH HEAT FLUX THERMAL LOOP

by

Rodward Lorenzo Hewlin, Jr.

A thesis submitted to the graduate faculty in partial fulfillment of the
requirements for the degree of
MASTER OF SCIENCE

Department: Mechanical Engineering
Major: Mechanical Engineering
Major Professor: Dr. John P. Kizito

North Carolina A&T State University
Greensboro, North Carolina
2010

School of Graduate Studies
North Carolina Agricultural and Technical State University

This is to certify that the Master's Thesis of

Rodward Lorenzo Hewlin, Jr.

has met the thesis requirements of
North Carolina Agricultural and Technical State University

Greensboro, North Carolina
2010

Approved by:

Dr. John P. Kizito Major Professor	Dr. Gary Tatterson Committee Member
Dr. Mannur Sundaresan Committee Member	Dr. Samuel P. Owusu-Ofori Department Chairperson

Dr. Alan Letton
Dean of Graduate Studies

DEDICATION

I dedicate this work to my loving family. To my parents, Rodward Lorenzo Hewlin Sr. and Arnetta L. Hewlin whose patience, nurturing and regard for education held me on a steady course throughout my academic studies. To my sister Brittany Michelle Hewlin, our quarrels to determine who the “smartest” sibling is has definitely contributed to both of our successes as individuals. I am very proud of you, and I expect even greater things from you. I want to mention my brother Cedric Alexander Hewlin, who taught me that life is very precious and that we should enjoy each fulfilling moment. Your presence in my life has taught me so many things. You are a very intelligent individual who I commend for your hard work and efforts. To my great grandmother, Laran E. Jordan, your presence in my life taught me the value of hard work and how far our generation has come over the decades. To my grandmother Flossie Peterson, I love you very much, your sacrifices and love for all of us has taught me to love, be unselfish and understanding. I want to thank my loving uncle and aunt who are also my Bishop and Co-Pastor, Bishop Sheldon McCarter and Co-Pastor Joyce McCarter for showing me love throughout my hardships, and also for providing me with a loving church home and family. I want to mention my loving cousins Xavier, Alana, and Alaya. The ministries of Greater Cleveland Avenue Christian Church also do not go unrecognized. And finally, to my loving Grandfather who is no longer with us Claude Hewlin Sr., I miss you and I love you dearly.

BIOGRAPHICAL SKETCH

Rodward Lorenzo Hewlin, Jr. was born in Rocky Mount, North Carolina on July 17, 1986. He is the son of Arnetta L. Hewlin and Rodward Lorenzo Hewlin, Sr., Owner and CEO of Hewlin Bros. Lumber Co., formerly known as Joseph & Sons Hewlin Lumber Co. est. 1879. Rodward Lorenzo Hewlin, Jr. has served greatly in K-6 Education and Secondary Education. Rodward has served in Guildford County Public School systems as a part of the Bush Administration’s Law “No Child left behind” Title I. K-6 tutor for L&U Contractors. Rodward has also taught undergraduate senior and junior level laboratory courses as part of the Mechanical Engineering curriculum at North Carolina Agricultural & Technical State University College of Engineering’s Mechanical Engineering Program.

As an undergraduate, Rodward enjoyed academic research. Rodward was an accomplice in the *Duke University’s Summer Research Experience for Undergraduates (REU)* in the summer of 2006, where he studied magnetic nanoparticles using a magnetophoresis-based method to obtain particle magnetic susceptibility. Rodward graduated with honors from North Carolina A&T State University in May 2008 with a Bachelors of Science degree in Mechanical Engineering. Subsequent to graduation, Rodward served as a North Carolina Space Grant Scholar for Lord Corporation in Cary N.C., where he studied rheological properties of Magnetorheological (MR) fluids.

ACKNOWLEDGMENTS

I would like to thank the following people for their assistance throughout my academic study. First, I would like to express thanks to my advisor Dr. John P. Kizito for all of his hard work and dedication to obtaining the laboratory space and funding for the present study, for also providing me the opportunity to further my career and study, and for sharing comedic analogies of relating scientific theories to everyday life situations which not only lifted my spirits, but provided a unique and different outlook on life in a scientific way. I would like to thank him for all his guidance, help and insight which strongly contributed to the completion of this work. I would like to express thanks to Mr. Bruce Howe and his shop staff for all of their help in machining parts for my measuring instruments, test apparatus and two-phase heat transfer loop. The efforts and advice of my committee members: Dr. Gary Tatterson and Dr. Mannur Sundaresan whose advice and support do not go unrecognized. I would also like to thank my former advisor of undergraduate research at Duke University, Dr. Benjamin Yellen, for not only motivating me to pursue a graduate degree, but for helping me leave my mark in the knowledge database of science. This project was funded by the United States Air Force, Department of Defense through AFRL in Dayton Ohio.

TABLE OF CONTENTS

LIST OF FIGURES

FIGURES **PAGES**

LIST OF TABLES

TABLES **PAGES**

NOMENCLATURE

A	Amperage, [amps]
A_h	Area of the heater, [m^2]
A_p	Capacitance probe/plate area, [m^2]
A_{pipe}	Pipe area, [m^2]
d	Gap distance, [m]
D	Pipe diameter, [m]
d_h	Heater diameter, [m]
h_{fg}	Latent heat of vaporization, [J/kg]
k	Thermal conductivity, [W/m·K]
L	Characteristic length of the target surface, [m]
P	Pressure, [MPa]
$\dot{m}_f$	Fluid mass flow rate, [kg/s]
Pe	Peclet number Pe=PrRe, [dimensionless]
Pr	Prandtl number Pr =α/ν, [dimensionless]
$\dot{q}$	Heat flux, [kW/m^2]
$\dot{Q}$	Total power, [kW]
$\dot{Q}_f$	Volumetric fluid flow rate, [l/min]
Re	Reynolds number, [dimensionless]

T	Temperature, [^{o}C]
T_s	Surface temperature, [^{o}C]
T_∞	Temperature of the surroundings, [^{o}C]
u, v, w	Velocity components in x, y, z directions, [m/s]
$u_{\text{calibration}}$	Calibration uncertainty
u_{fit}	Uncertainty in the regression
V	Voltage, [volts]
V_{ac}	Alternating voltage, [volts]
V_{dc}	Direct voltage, [volts]
V_{heater}	Heater voltage, [volts]
V_f	Velocity of fluid, [m/s]
W	Work, [J]
Z_c	Output impedance, [ohms]
L/H	Dimensionless distance from impinging point, [dimensionless]

GREEK SYMBOLS

α	volumetric void fraction, [dimensionless]
κ	dielectric constant, [dimensionless]
Ω	Resistance, [ohms]
ε_o	Permittivity of free space, [$C^2N^{-1}m^{-2}$]
ΔP	Measured pressure drop across restriction, [MPa]

ω	Angular frequency, [rad/s]
ρ	Density, [kg/m^3]
ΔT	Excess temperature, [^{o}C]
σ	Surface charge density, [Cm^{-2}]
μ	Dynamic viscosity, [kg/m·s]

LIST OF ABBREVIATIONS

A_{dev}	Device accuracy
A_{pp}	Application accuracy
CHF	Critical heat flux
ERT	Electrical Resistance Tomography
FFT	Fast Fourier Transform
F.S.	Full scale reading
$F.S._{app}$	Application full span
$F.S._{dev}$	Device full scale reading
MPa	Mega-Pascal
PDA	Personal digital assistant
psia	Pounds per square inch absolute
psig	Pounds per square inch gage
T.C.	Thermocouple
QCV	Quick closing valve

ABSTRACT

Hewlin, Jr., Rodward Lorenzo. DEVELOPMENT OF DIGITAL DIAGNOSTICS AND MEASUREMENT TOOLS FOR A HIGH HEAT FLUX THERMAL LOOP. **(Major Advisor: John P. Kizito)**, North Carolina Agricultural and Technical State University.

The ultimate goal of the present study is to enhance high heat flux removal and thermal management using spray cooling techniques. As a result, a two-phase heat transfer spray cooling loop was developed capable of removing high heat fluxes from a 0.0001 m^2 (1 cm^2) heated surface using water. The specific objectives were based on providing the necessary measuring tools and instrumentation for designing an efficient heat transfer loop diagnostics and measuring system. The instruments used consisted of the following measurement device types: flow rate, pressure, temperature, and void fraction. The selection of these devices involved preliminary analyses which were done in order to insure the measuring tool's suitability for measuring quantities and parameters of interest. Two designs of capacitive void fraction sensors were considered.

Over the course of the present study, some of the problems associated with the first void fraction sensor electrode design were identified and a new sensor electrode configuration was developed which provided a more sensitive and repeatable response. Data was collected covering a wide range of void fraction measurements ranging from 0 to 1 for two candidate fluids. The calibration data obtained was nonlinear for the full range of void fraction measurements. The present study also consisted of designing a

thick film resistive high heat flux heater. The design and calibration procedures developed and used for each measuring tool is discussed further in detail.

CHAPTER 1

INTRODUCTION

Thermal design issues are crucial topics in electronic product development at all levels from high powered electronics to military defense systems. Shrinking system size results in an increase of volumetric heat flux and surface heat fluxes in various electronic equipment. Ongoing pressure in manufacturing for cost reduction and high performance capability is also a major concern. These compact system designs have resulted in a major interest in high heat flux removal and thermal management. The following section will discuss the ultimate goal and specific objectives of the present study.

1.1 Specific Objectives

The ultimate goal of the present study is to enhance high heat flux removal and thermal management using spray cooling techniques. By doing so, a two-phase heat transfer spray cooling loop has been developed capable of removing high heat fluxes from a heated surface using water. Designing an efficient diagnostics measuring system for the heat transfer loop was vital in the pursuit of reaching the ultimate goal. Therefore, the specific objectives were based on providing the necessary measuring tools and instrumentation for developing an efficient heat transfer loop diagnostic and measuring system. The specific objectives of the present study were as follows:

1. Design a thick film resistive high heat flux heater capable of producing a heat flux of 10,000 kW/m^2 (1000 W/cm^2) to the heated surface area.

2. Design a diagnostic and measuring system which implements commercially available measuring tools and devices that consist of the following:
    - Temperature measuring devices (thermocouples)
    - Flow measuring devices (flow meters)
    - Pressure measuring devices (pressure transducers)
3. Design a void fraction sensor.

The developed sensor should:

- Be capable of determining a mean value of the phase percentage of liquid/vapor in the two-phase flow field.
- Be capable of measuring the entire range of void fractions.
- Be capable of measuring void fraction with either Water or Novec 7000 as the working fluid.
- Retain high sensitivity for a continuous flow field.
- Be insensitive to vibrations, and be able to withstand the heat transfer loop operating pressure ranges.

1.2 Requirements for Selecting Measurement Tools

The following requirements were considered in determining each measuring tool's suitability for a particular measurement:

- **Range.** The measurement range of the measuring device and data acquisition system should be suitable enough to encompass all the expected magnitudes of the quantity to be measured.

- **Sensitivity**. The measuring device and data acquisition system should produce a sufficient output signal per unit of measured input.
- **Electrical output format.** The electrical form of the measuring device's output signal must be compatible with data acquisition system.
- **Power requirements.** The power supply used should be able to produce the required external excitation for all the electronic measuring devices and the heater.
- **Errors.** The errors inherent in the operation of the measuring device itself, or those errors caused by environmental conditions of the measurement, should be small enough or controllable enough that they allow meaningful data to be taken.

CHAPTER 2

LITERATURE REVIEW

Chapter 2 presents a review of literature on measuring tools and instrumentation used in thermal management systems. A review on measuring system designs from previous spray cooling studies is presented which includes: pressure, flow rate, temperature measuring devices, and high heat flux heater designs. Thorough reviews of quick closing valves, radiation techniques, conductance probes, and capacitive techniques are also presented as one of the techniques used to measure void fraction. The review of literature on measuring system designs focuses on: measuring system design layout, measuring tool/component device types, measurement uncertainty, and high heat flux heater designs. The next section presents an introduction to spray cooling technology.

2.1 Spray Cooling Technology

The topic of spray cooling has been around since the early 1960s; scientific investigations began with the theoretical and experimental (Hosler & Westwater, 1962) study of film boiling. Today, the topic of spray cooling has developed into a technology of increasing high interest for electronic cooling and other high heat flux applications. Spray cooling involves a dispersion of liquid droplets impinging on a heated surface area by single or multiple nozzles. The droplets spread onto the heated surface and evaporate or form a thin liquid film, removing large amounts of energy at low temperatures as shown in Figure 2.1. Spray cooling is capable of uniform heat removal, small fluid inventory, and low temperature overshoots. Spray cooling can be used to transfer relatively large quantities of energy at low temperatures by the working fluids latent heat of vaporization (Horacek, et al., 2004). The energy content in spray cooling is the phase change process which takes advantage of large amounts of latent heat exchange. The latent heat exchange is capable of removing high heat fluxes from the heated surface with low superheat. Heat fluxes up to 10,000 kW/m^2 (1000 W/cm^2) have been demonstrated in spray cooling with water as the working fluid. Elevated heat fluxes in the excess of 10,000 kW/m^2 (1000 W/cm^2) using fluorinert working fluids have also been demonstrated while allowing tight temperature control at low coolant mass flow rates (Silk, et al., 2006).

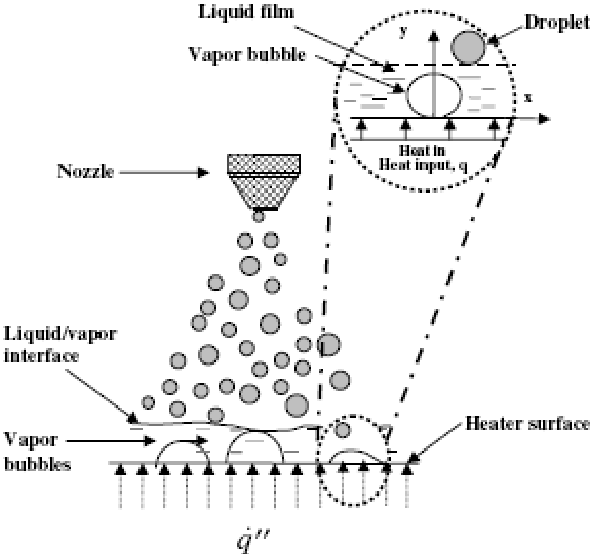

Figure 2.1: Schematic diagram of liquid droplets impinging on a heated surface. Obtained from (Silk, et al., 2008).

Spray cooling technology for high temperature surfaces plays a vital role in space applications, industrial processes, and even dermatologic applications (Svaasand, 2003; Basinger, 2004; Aguilar, 2001; Aguilar, 2001; Su, 2007; Aguilar, 2005). Heat transfer rates much higher than can be attained in pool boiling are possible with spray cooling since there is less resistance in the removal of vapor from the heated surface. Some disadvantages include the need for pumps, filters and the need to transport excess liquid and vapor to a condenser. The overall heat transfer spray cooling loop performance and measurement accuracy is affected by the working fluid, operating conditions, loop components, and selection of measuring tools for monitoring system performance. The ability to accurately measure parameters of interest in an experiment can be a complicated task, and can also be catastrophic if measuring tools and components are not selected properly. The next section provides a review of spray cooling loop measuring system designs.

2.2 Survey of Spray Cooling Heat Transfer Loop Designs

Several heat transfer spray cooling loop measuring system designs have been presented by numerous researchers. The design of a heat transfer spray cooling loop measuring system is contingent upon the operating ranges of the heat transfer loop. The measuring tools and components used should be properly selected for the required measurement range and application accuracy. The review of spray cooling loop measuring system designs will focus on: measuring system design layout, measuring instrument/component device types, measurement uncertainty, and high heat flux heater designs. The following discussion will present a review of previous designs of spray cooling loop measuring systems.

In the study of (Mudawar & Estes, 1996), spray cooling of a heated surface was investigated to determine the effect of nozzle-to-surface distance on critical heat flux (CHF). Full cone sprays of fluorinert FC-72 and FC-87 were used to cool a square 12.7 x 12.7 mm^2 (0.0000127 m^2 x 0.0000127 m^2) heated surface. The heat transfer loop consisted of a magnetically coupled centrifugal pump which forced the fluid from the reservoir positioned beneath the test chamber through the corresponding loop components. The loop components included three flat plate heat exchangers, a carbon filter, a flow-through electrical heater, and a rotameter. A pressure gage was positioned upstream of the spray nozzle and another was connected straight to the test chamber. The test chamber pressure was used as a reference for determining the saturation temperature and associated properties used in obtaining CHF data. The uncertainties in the pressure measurements were determined from the pressure gage manufacturer specifications to be less than 0.5%, which was also confirmed by calibration.

It was reported that the uncertainties in the spray flow rate measurements were due to the following facts. These were the fabrication tolerances, temperature changes on the density and viscosity of the fluid, as well as the expansion and contraction of the rotameter parts. These uncertainties were estimated from the manufacturer specifications at 1.6% which was also validated by calibration. Heat was supplied to the impingement surface by a thick film electrical resistor, which was soldered to the base of the copper block. A schematic of the heat transfer loop is presented below in Figure 2.2.

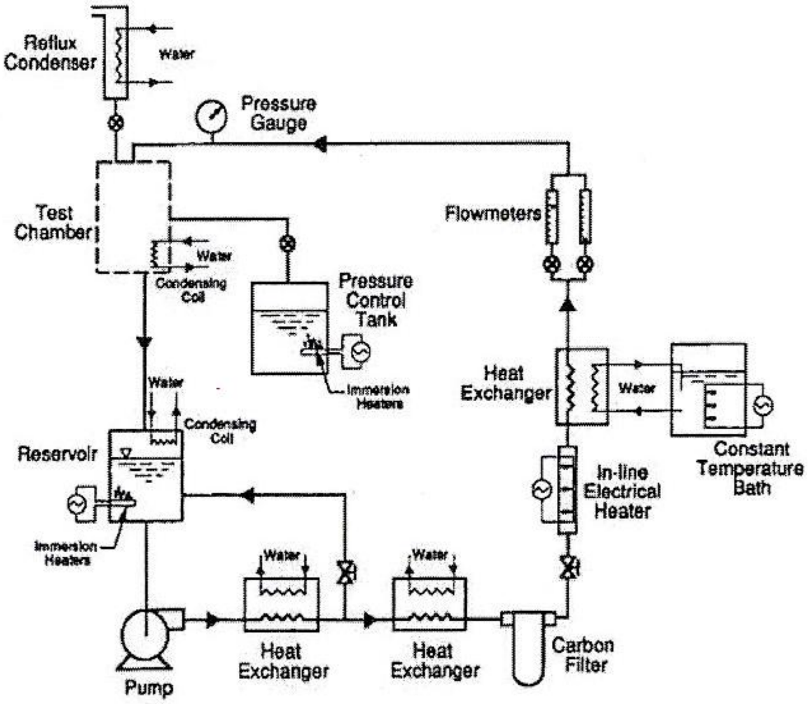

Figure 2.2: Schematic diagram of the heat transfer loop developed and used in the study of (Mudawar & Estes, 1996).

The heater was insulated on all surfaces except the impingement surface with G-7 fiberglass plastic. A schematic of the heater module is presented in Figure 2.3. A schematic of the thick film resistor is presented in Figure 2.4. Uncertainties in the measurement of electrical power input to the thick film resistor and the resistance of the thick film resistor's lead wires was estimated at 1.0%. An additional source of uncertainty in the measurement of heat flux was the heat loss from the boundaries of the heater. From the reported results it is evident that knowing the measurement uncertainty of all the measuring tools and components is vital for data analysis and reduction.

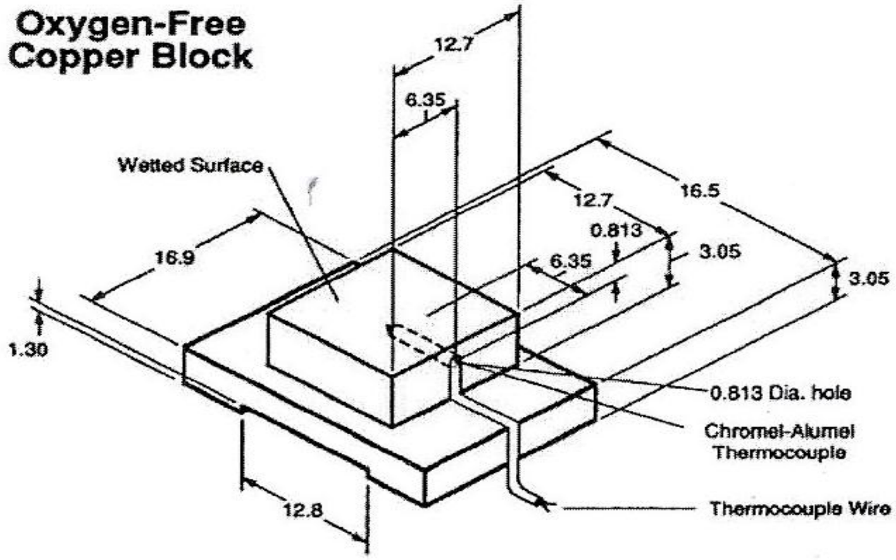

Figure 2.3: Schematic diagram of the heater module developed and used in the study of (Mudawar & Estes, 1996).

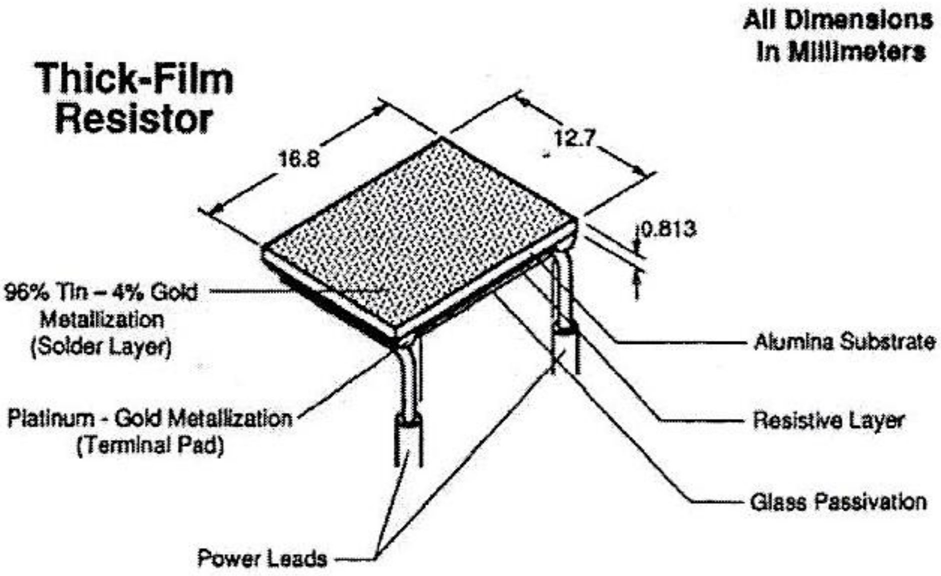

Figure 2.4: Schematic diagram of the heating element developed and used in the study of (Mudawar & Estes, 1996).

In the study of (Ortiz & Gonzalez, 1999), a heat transfer spray cooling loop was developed to study steady-state heat fluxes in spray cooling. The heat transfer spray cooling loop consisted of a copper heater containing a disk-shaped heating surface, a commercial multiple nozzle atomizer system, and a data acquisition system for data recording purposes. The reduction in diameter was reported to have increased the heat flux at the tip of the copper bar. Holes were drilled at one end of the copper bar (the reduced end) and at the other end of the copper bar (three times at three different axial levels to facilitate instrumentation). The holes were separated by 120^o at each level and inserted approximately 0.476 cm (0.00476 m) deep. Nine K-type thermocouples were imbedded into the holes drilled on the reduced-diameter section.

The thermocouple tips were inserted into a 0.0127 cm (0.000127 m) diameter ceramic rod and covered with a conductive resin to avoid air gaps inside the holes. The energy in the copper bar was provided by an electric heating band 10.2 cm (0.102 m) long. A schematic of the heat transfer loop used in the study of (Ortiz & Gonzalez, 1999) is presented in Figure 2.5. The heated surface used in this study consisted of a copper bar with a base diameter of 3.5 cm (0.035 m) and a length of 17 cm (0.17 m). The heater was tapered to reduce one end to 1.25 cm (0.0125 m) in diameter as shown in the schematic presented in Figure 2.6. Spray cooling curves were generated to demonstrate the steady-state boiling process for each parameter considered.

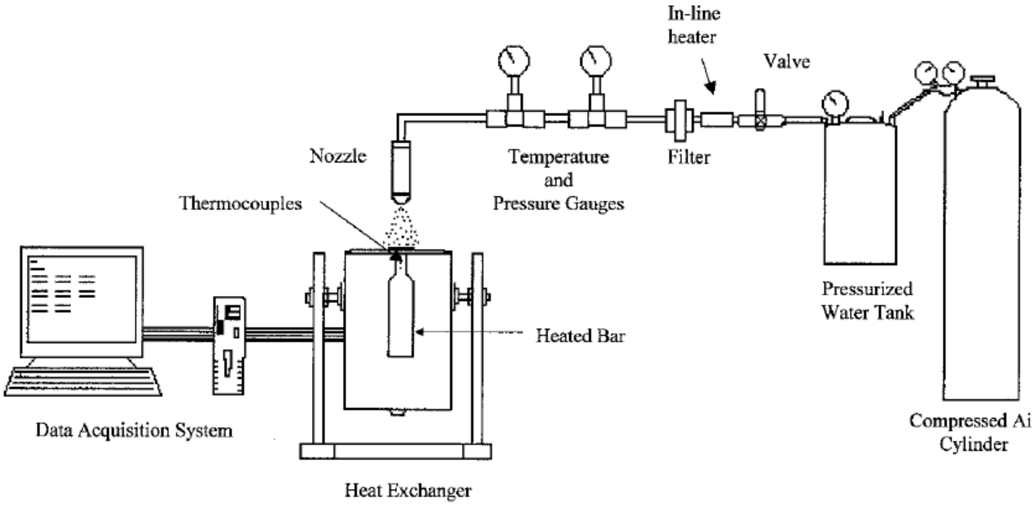

Figure 2.5: Schematic diagram of the spray cooling heat transfer loop developed and used in the study of (Ortiz & Gonzalez, 1999).

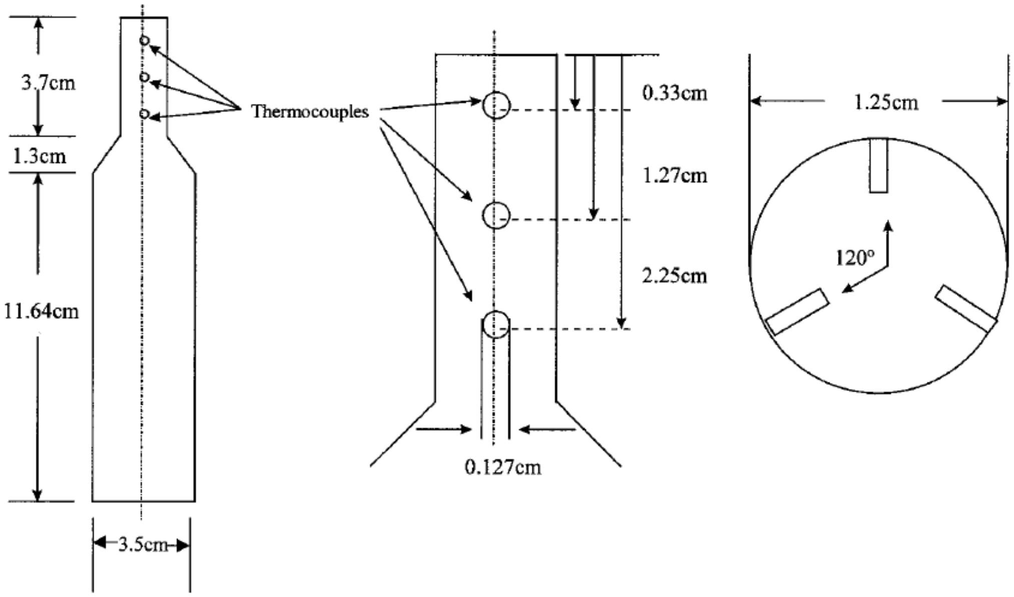

Figure 2.6: Schematic diagram of the copper heated bar developed and used in the study of (Ortiz & Gonzalez, 1999).

The author reported that from the generated curves, it was clear that steady-state high heat fluxes of the order of 500 W/cm^2 (5000 kW/m^2) could be obtained using spray cooling. The heater design reported in the work of (Ortiz & Gonzalez, 1999) is robust compared to the thick film resistor heater design mentioned in (Mudawar & Estes, 1996). Although the heater mentioned by (Ortiz & Gonzalez, 1999) achieves the goal of producing high heat fluxes, a smaller and efficient heater design would be a better alternative when considering space accommodations and instrumentation. The heat flux measurement uncertainty in heaters which incorporate neck regions are a function of the neck length.

(Chen, et al., 2002) conducted a study to investigate the effects of spray parameters (mean droplet size, droplet flux, and droplet velocity) on CHF while varying the spray parameters systematically. The spray cooling heat transfer loop consisted of a heater made of a pure copper block. The heater contained four 500 W cartridge heaters. The copper block was a solid cylinder 12 cm (0.12 m) in diameter and 30.5 cm (0.305 m) in height that tapered off near the top to a 1x1 cm^2 (0.0001 x 0.0001 m^2) surface area. The heater was supported by an aluminum enclosure surrounded by a Durablanket © insulation (thermal conductivity, k=0.013 W/m·K) positioned between the copper and the aluminum enclosure. The entire copper block was insulated except at the crown (i.e., the heater surface). The heater was capable of supplying more than 1500 W (1.5 kW) to the 1 cm^2 (0.0001 m^2) crown surface. A schematic of the heater is presented in Figure 2.7

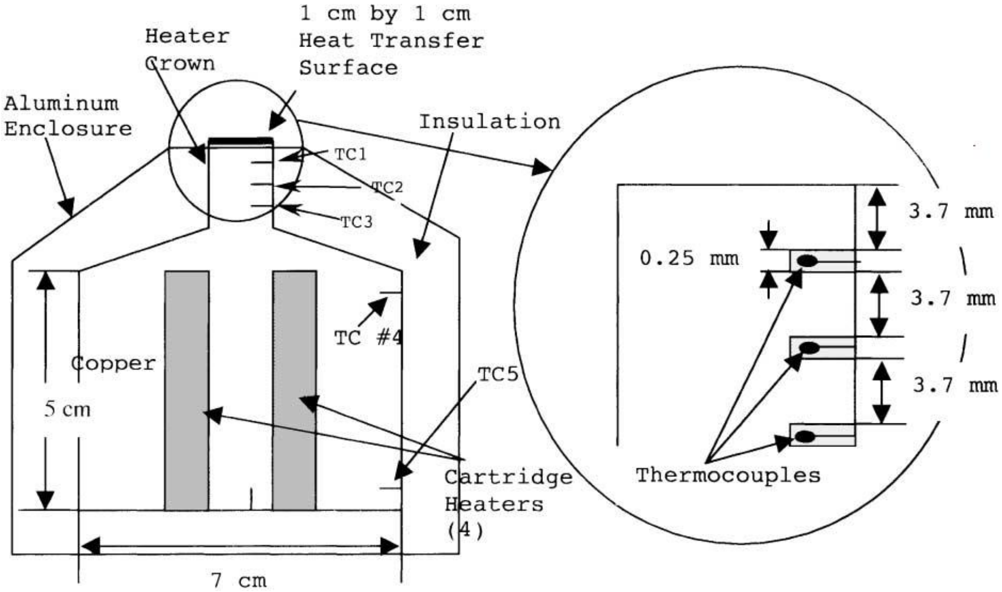

Figure 2.7: Schematic diagram of the copper heater developed and used in the study of (Chen, et al., 2002)

The space between the crown/heater surface and the aluminum enclosure was sealed using a high-temperature silicon rubber sealant so that the water could not reach the copper block. Three K-type thermocouples (TC1, TC2, and TC3) in Figure 2.7, each having a 0.003 in (0.0000762 m) bead diameter were imbedded below the heater surface (in the neck region) to provide the temperature gradient and temperature profile within the neck region. Knowing the temperature difference between these thermocouples and the distance between them 0.37 cm (0.0037 m), it was possible to predict the heat flux using the one-dimensional Fourier's law of heat conduction. The distance between the heater surface and TC1 was also 0.37 cm (0.0037 m). The surface temperature was determined by extrapolation using the measured temperature gradient in the neck region specified by the three thermocouples. Two thermocouples (TC4 and TC5 shown in Figure 2.7) were positioned on the large section of the copper block to monitor the temperatures to ensure that the automatic shut-off of the power could be accomplished when the temperatures approached near the operation limit (i.e. the softening point) of the heater.

A PC recorded the temperature measurements, calculated the heat flux, and measured the surface temperature. The direct measurement of mass flow rates was performed using a graduated cylinder and a stopwatch. The heater design reported in the work of (Chen, et al., 2002) could be improved for size and heat flux measurements. The size and shape of the heater introduces heat flux measurement uncertainty. The heat flux uncertainties can be reduced to negligible values if the design is modified. The design should be modified to incorporate a heating element which focuses the heat directly to the heated surface as a substitute of incorporating neck region which introduces heat flux measurement uncertainty.

In the study of (Zhou & Lee, 2007) a spray cooling heat transfer loop was developed to investigate the fluid flow and heat transfer of a rectangular air jet impinging on a heated flat plate. A schematic diagram of the heat transfer loop is presented in Figure 2.8. A heat exchanger was used to adjust the air temperature to maintain the jet exit temperature within $\pm 0.1^{o}$C of the ambient room temperature. The flow rate was measured with an ASME standard orifice flow meter with ±1% reading accuracy. A circular straight PVC pipe with internal diameter of 0.0523 m and a length of 2.5 m was used.

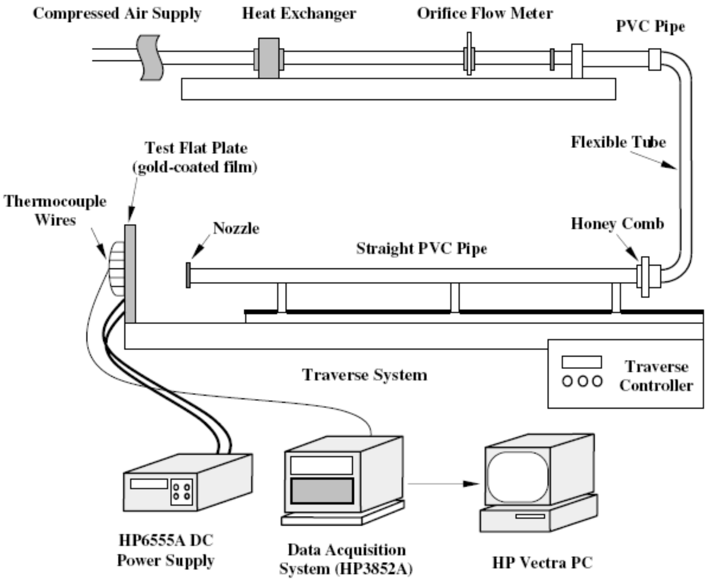

Figure 2.8: Schematic diagram of the heat transfer loop used in the study of (Zhou & Lee, 2007).

The pipe was tightly mounted on a traversing fixture by which the nozzle-to-plate spacing could be adjusted within a resolution of 0.00001 m. A sharp-edged rectangular nozzle was horizontally attached at the downstream end of the long pipe as shown in Figure 2.8. One thermocouple was installed using a feed-through hole at 0.20 m upstream from the nozzle exit to measure the jet temperature. An additional thermocouple was placed near the impingement region to monitor the ambient air temperature. The heated impingement plate was composed of a plexiglass flat plate, a gold-coated film, thirty-three T-type thermocouples and two copper electrodes.

The plexiglass plate of 303 x 303 mm^2 (0.000303 x 0.000303 m^2) was 0.0127 m thick and had a low thermal conductivity. The transparent vacuum-deposited gold-coated film, 0.120 m long by 0.040 m wide, had a thickness of 127 µm (0.000127 m) and was glued to the plexiglass plate. Two copper-foil strip electrodes with a thickness of 100 µm (0.0001 m) were attached to the film. Silver paint was then applied to establish a good electrical contact between the electrode and the upper surface of the film. The electrodes were connected to a DC power supply (HP6555A) in series with a shunt, rated 50 mV and 5 A, allowing adjustable DC voltage to the electrodes.

A DC electric current was applied to the film, and a nearly uniform wall heat flux boundary condition was established. A HP3852A data acquisition system was used to measure the electric voltage drop across the film, current input to the shunt register and the temperatures of all the thermocouples. The uncertainties in the study of (Zhou & Lee, 2007) was estimated using the method suggested by (S.J Kline, 1953) within a 95% confidence level. The wall temperature was reported to have an uncertainty in the range of 1.57–2.25%. The measurement uncertainty for the mean velocity and the turbulence intensity was estimated to be less than 1.4% and 3.5%, respectively.

In the study of (Bostanci et al., 2009), an investigation on spray cooling with micro-structured surfaces was performed. Tests were performed in a closed loop system with ammonia as the working fluid using RTI's vapor atomizer spray nozzles. Thick film resistors were used as the heating source. Heat fluxes up to 500 W/cm^2 (5000 kW/m^2) (well below the critical heat flux limit) were removed. Two nozzles each spraying 1 cm^2 (0.0001 m^2) of the heater area used 96 ml/cm^{2}min (9.7 gal/in.^{2}h) liquid and 13.8 ml/cm^{2}s (11.3 ft^3/in.2h) vapor flow rate with only 7 psi (48 kPa) pressure drop.

Figure 2.9 presents a schematic of the heat transfer loop. The main components of the loop are: a reservoir, 1x2 nozzle array, sub-cooler, condenser, and pump. The reservoir supplies ammonia liquid and vapor to the nozzle array. The liquid and vapor is mixed in the atomizer nozzles, and then the resulting spray cools a 1x2 cm^2 (0.0001 x 0.0002 m^2) thick film resistive heater. The exhaust from the 1x2 nozzle array slightly sub-cools the incoming liquid supply in a small heat exchanger prior to flowing into the larger heat exchanger to condense.

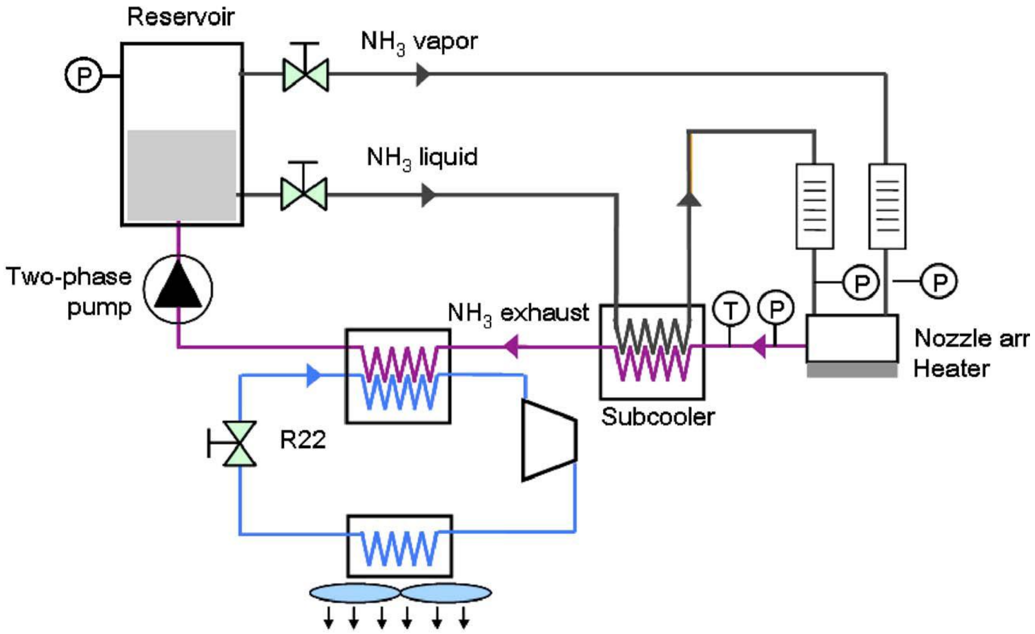

Figure 2.9: Schematic diagram of the heat transfer loop developed used in the study of (Bostanci et al., 2009).

The heat transfer loop allows control of flow rates and pressures across the nozzle array and is equipped with computer controlled data acquisition system for accurate data recording. The uncertainties for the heat flux and temperature measurements were estimated and reported. The error reported in the heat flux measurement involved variations in voltage, current, and area. The error was reported to be ±2.3% at 500 W/cm^2 (5000 kW/m^2). The error in temperature measurements from the embedded thermocouples in the heater wall (considering thermocouple and data acquisition system specifications) was calculated to be ±1.0^{o}C. The spray surface temperature was reported to have had a slightly higher uncertainty at ±1.1^{o}C. Heat transfer coefficients included ±5.5%, 7.7%, and 10.3% uncertainties at 500 W/cm^2 (5000 kW/m^2) for smooth, micro-i, and micro-p surfaces, respectively. The heat loss from the thick film resistors to the surrounding was reported to be negligibly small (<1 W) based on calculations considering natural convection and black body radiation form 100^{o}C heater surface to 20^{o}C ambient air.

The heater design presented in the work of (Bostanci, et al., 2009) was reported to achieve the goal of removing high heat fluxes up to 500 W/cm^2 (5000 kW/m^2). The main advantage listed in the work of (Bostanci, et al., 2009) is the heat flux measurement uncertainty values. Uncertainty values in heat flux measurements are vital, as they represent the amount of heat flux measurement error. Heat flux measurement uncertainty should be reduced as much as possible. From the review of literature on measuring system designs, it appears that thick film resistive heaters are more efficient heating elements due to their size. It is also evident that measurement uncertainty is a vital quantity and should be afforded much attention. The next section will discuss spray cooling parameters.

2.3 Spray Cooling Parameters

In support of studying spray cooling data, the spray cooling “curve” is represented by heat flux vs. wall temperature. The spray cooling curve tends to be linear in nature for low wall temperatures. The linear trend for low wall temperatures indicates that the heat transfer is dominated by single-phase convection, although some evaporation may occur. Generally, the supply of incoming cold liquid is relatively high in order to maximize heat transfer. In this instance, there is a small amount of time for the heater to increase the local temperature. As a result, the liquid is swept away by fresh cold liquid before it can heat up enough to generate a bubble. High wall temperatures are required to begin significant bubble nucleation. Droplet impact onto the liquid film can also provide significant agitation, increasing the amount of heat transfer.

The energy content in spray cooling is the working fluids latent heat of vaporization. During a vaporization process, the fluid appears as part liquid and part vapor. That is, it is a mixture of both saturated liquid and saturated vapor. As a result this introduces a new quantity of interest, vapor quality. To measure quality, the portions of the liquid and vapor present in the mixture must be known. Quality is defined as the ratio of the vapor to the total mass of the mixture. Quality has significance for saturated mixtures and can serve as one of the two independent properties needed to describe the state of the flow. Similar to spray cooling, in micro-channel research, quality should be controlled to prevent dry-out. Table 2.1 presents a review of researchers that report that the heat transfer coefficient is a function of quality, mass velocity, and wall heat flux etc.

Table 2.1: Summary of mini and micro-channel studies.

Author(s)	Fluid	Heat Flux q''	Vapor Quality	Remarks
(Lazarek & Black, 1982)	R-113	1.40-38.0	<0.0-0.60	The heat transfer coefficient was found to be a function of heat flux and nucleation is the dominant mechanism controlling the wall heat transfer process in all tests. As a result, heat flux is independent of vapor quality and mass flux.
(Wambsganss, et al., 1993)	R-113	0.88-9.08	0.0-0.90	The heat transfer coefficient was found to be a function of heat flux and nucleation is the dominant mechanism controlling the wall heat transfer process in all tests. As a result, heat flux is independent of vapor quality and mass flux.
(Tran, et al., 1996)	R-12	3.60-12.9	0.0-0.96	The heat transfer coefficient was found to be a function of heat flux and nucleation is the dominant mechanism controlling the wall heat transfer process in all tests. As a result, heat flux is independent of vapor quality and mass flux.
(Kew & Cornwell, 1997)	R-141b	0.97-9.00	0.0-0.95	The heat transfer coefficient was found to be a function of the heat flux and vapor quality. Also, nucleate boiling and convective boiling are important quantities.
(Ravigururajan, 1998)	R-124	8.00-65.0	0.0-0.50	In this case, the heat transfer coefficient is a function of the heat flux and vapor quality. The heat transfer coefficient was found to increase with increasing vapor quality.
(Yan, et al., 1999)	R-134a	0.50-2.00	0.1-0.90	In this case, the heat transfer coefficient was found to be a function of the heat flux and vapor quality. The heat transfer coefficient was found to increase with increasing vapor quality and saturation temperature.
(Bao, et al., 2000)	R-11 and R-123	0.50-2.00	<0.0-0.90	The heat transfer coefficient was found to be a strong function of heat flux, but almost independent of mass flux.
(Lee, et al., 2001)	R-113	0.30-1.58	0.15-0.750	The heat transfer coefficient and convective boiling was found to be the dominant heat transfer process. As a result the heat transfer coefficient increases with vapor quality, and heat flux has a minor effect.
(Lin, et al., 2001)	R-141b	0.18-7.20	<0.0-1.00	The heat transfer coefficient was found to increase with heat flux for vapor qualities of up to 0.4 but fell gradually decreased.
(Yu, et al., 2002)	Water-ethylene glycol, FC84	10.00-30.00	0.0-1.00	The heat transfer coefficient is a function of heat flux and nucleation is the dominant mechanism controlling the wall heat transfer process in all tests. As a result, heat flux is independent of vapor quality and mass flux.
(Warrier, et al., 2002)	Water	0.00-5.99	<0.03-0.50	For vapor qualities less than 0.3, the heat transfer coefficient decreases rapidly with increasing quality, while at higher values of above 0.3,the heat transfer coefficient becomes independent of vapor quality.
(Wen, et al., 2004)	Water	2.60-16.0	0.0-0.30	In this case the heat transfer coefficient is proportional to heat flux. As a result nucleate boiling and convective boiling are an important quantity.
(Bertsch, et al., 2009)	R-134a and R-245fa	0.00-22.0	-0.2-0.90	The heat transfer coefficient is found to vary significantly with heat flux and vapor quality, but only slightly with saturation pressure and mass flux for the range of values investigated
(Wang, et al., 2009)	Water	2.10-5.00	<0.0-0.30	The heat transfer coefficient is dependent upon mass flux, heat flux, saturation pressure, and vapor quality are dependant properties
(Ong, et al., 2009)	R-134a, R-236fa and R-245fa	0.23-2.50		The heat transfer coefficient for all three fluids tested was dependent on heat flux at low vapor qualities whilst convective boiling seems to dominate at higher vapor qualities.

For two-phase flow applications, it is not practical to design for absolute evaporation. This is due to the fact that dry-out will occur before total vapor quality (i.e. 100 percent vapor) is attained, which will result in extensive surface overheating. In a sensible system, flow instabilities and uneven heating should not exist. As a result, there have been numerous techniques of studying phase percentages of vapor and liquid in two-phase flows. Several studies have used flow maps as a technique of describing two-phase flows. In order to predict the flow regime of a two-phase flow by flow mapping techniques the mass velocities, mass flow rates, and superficial velocities of the gas and the liquid must be known. There have been numerous attempts to create transition boundaries between these regimes based on theoretical assumptions (Taitel, et al., 1976 ; Taitel, et al., 1978). These techniques are based on empirical correlations.

The accuracy of these correlations is within a range of 0 to 100%. Flow maps are useful to provide an initial basis of the type of flow regimes that one would expect to see under given operating conditions. However, in order to gather quantitative and more objective information about the nature of the two-phase flow, an experimental measurement is appropriate. Several studies have proposed void fraction as a means of studying the phase percentage of two-phase flows. There are several methods available for measuring void fraction. Some of these methods are: quick closing valves (QCV), radiation attenuation, conductance probes, capacitance probes and many other techniques. The next section presents an introduction to techniques of measuring void fraction.

2.4 Survey of Void Fraction Measurement Techniques

There has been a great deal of attention in the development of precise and accurate techniques of measuring void fraction. As mentioned earlier in section 2.4, these methods include: quick closing valves (QCV), radiation attenuation, conductance probes, capacitance probes and many other techniques. A review of reports consisting of the design, characterization, operation, and theory are presented. When liquid-vapor phase mixtures enter a conduit, the phases of the flow may distribute into a mixture of patterns. The particular pattern one observes depends on a number of parameters including flow rate, the fluid properties and the tube size (Taitel, et al., 1980). Figure 2.10 presents an illustration of the different types of flow patterns.

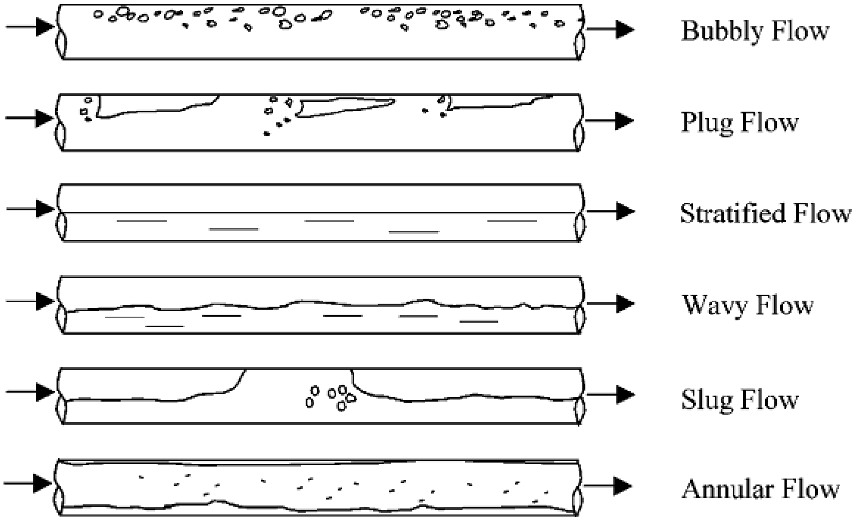

Figure 2.10: Schematic diagram of various flow regimes obtained from (Oddie & Pearson, 2004).

Depending on the liquid and gas flow rates, fluid properties, tube size, and the flow field, the flow will assume: bubbly flow (where the gas flows are discrete bubbles in the liquid medium), slug flow (where the gas is contained in long Taylor bubbles separated by liquid slugs), and annular flow (where the liquid forms an annulus around the circumference of the tube and the gas flows uninterrupted through the core).

2.4.1 Quick Closing Valves (QCV)

Due to the transient behavior of two-phase flows, the majority of void fraction measuring techniques involve a collected average of data obtained from a control volume at the same flow conditions, or by time-averaged measurements. Quick-closing valves (QCV) are one of the oldest and simplest techniques used to measure void fraction. The QCV method involves flow entering a control volume or "test section" in which two electromagnetic valves separate the analyzed stationary flow from the moving flow. After steady-state flow is achieved in the two-phase flow test section, the valve switches are activated and the valves are closed simultaneously. The void fraction is then determined by visual observance of the volume occupied by the gas in the "test section" to the total volume of the test section. Several studies have been done in order to study void fraction of two-phase flows by QCVs.

(Dounan Jai, et al., 1985) conducted an experimental study in vertically upward and downward air-water two-phase flows in order to minimize errors in void fraction measurements, and concluded that the closing/entrapment time for the (QCV) must be short when two-phase flow is entering the heater. This was due to the vapor quality gradually increasing throughout the test section. The experimental errors were reduced to negligible values. In the case of adiabatic two-phase flow when the quality is constant, the entrapment time does not require short entrapment time, yet both valves still must close concurrently.

(Gao H. H. & Chen, 1985) also used quick closing valves and obtained an entrapment switching time of 0.03 seconds at the inlet and outlet of the test section. The variation in entrapment time between the inlet and outlet valves was 0.009 seconds. The author used QCV's in addition to the conductance probe method and obtained satisfactory results for horizontal and vertical flows. (Jiang & Rezkallah, 1993) performed a study on void fraction in a small diameter tube (9.525 mm) for vertical upward and downward gas-liquid flows using a single beam gamma densitometer. The gamma densitometer was calibrated against the reading from the quick-closing valve setup. (Govier & Omer, 1962) also used quick closing valves in order to measure the void fraction of air and water in a horizontal pipeline flow.

2.4.2 Survey of Radiation Attenuation Techniques

Radiation attenuation methods have also been used to measure void fraction. There are two separate detection technique setups used in radiation attenuation. In the simplest setup, the source and detector are located on the outer perimeter of pipe, and the measurement is composed of an average reading across the width (diameter) of pipe from the source to the detector as shown in Figure 2.11. In a more elaborate setup, a transversing mechanism is used to vary the relative location of the source, the detector and the pipe. In this manner, an average reading over a selected chordal distance can be obtained, and the measurement more closely approximates a local reading. In most cases a multiple beam approach is utilized.

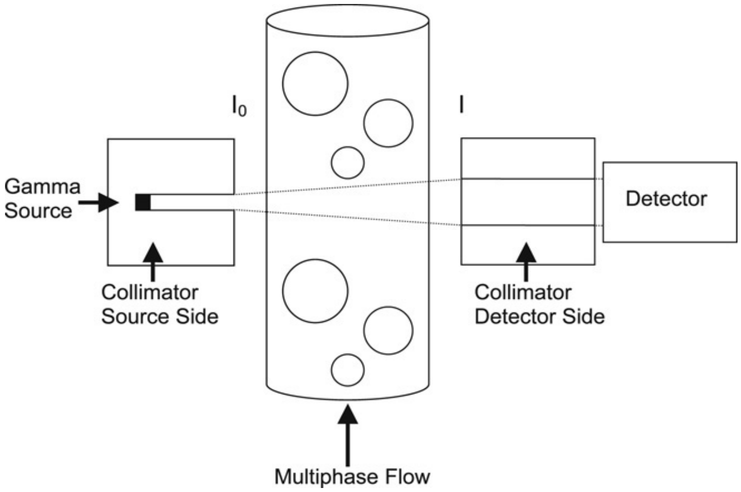

Figure 2.11: Schematic diagram of a radiation attenuation detector setup.

In these cases different chordal positions can be used to identify the flow regime via void fraction measurements. Photon beams (γ-rays, β-rays, and x-rays) are attenuated when they penetrate through a two-phase flow section. The attenuation rate increases with increasing density. Thus, from the attenuation rate and the density of the medium, a void fraction measurement can be obtained. Gamma densitometers have been used extensively to study void fractions in two phase flows. A gamma-densitometer consists of a gamma source and a detector. The source is a radio-nuclide, which emits and decays mono-energetic photons, thus gamma-radiation. The source is shielded and has typically has one opening equipped with a collimator to generate a gamma-beam. The next section provides a review of conductance and impedance methods of measuring void fraction.

2.4.3 Survey of Conductance and Impedance Probes

Void fraction measurements can also be obtained by conductance or impedance techniques. A conductance probe can be mounted flush with the wall of the conduit or it may be an intrusive probe. The conductance technique is based on electrodes which contain a voltage potential. The resulting current through the two-phase mixture is passed through a resistor and the voltage drop across this resistor is measured. The change in voltage gives information about the phase percentage of liquid-vapor phases present in the cross-sectional area of the conduit. If its resistivity is high, some electrolytes are added to raise the conductivity.

The shape of the conductance-time curve provides a means for flow regime identification or the duration frequency of bubble passage which provides information about void fraction. Impedance probes have also been used to measure void fraction. A list of previous studies using impedance probes to measure void fraction is listed in Table 2.2. (Costigan & Whalley, 1997) investigated flow regime identification by using a conductance probe. The experiment consisted of a 32 mm diameter tube with air and water as the two-phase flow mixture.

Table 2.2: Previous studies of void fraction measurements by impedance probe techniques.

Author(s)	Electrode Config.	Flow Patterns	Orientation	Fluid	Calibration Tech.	Results/Remarks
(Lamarre & Melville, 1992)	Parallel stainless steel electrodes	Wavy flow and Bubbly	N/A	Air-water	Calibrations were performed in a bubble tank with adjustable bubble size and air flow rates.	For annular flows where the phases are not radially symmetric indicate that each electrode should subtend to an angle of 90 degrees to properly measure void fraction.
(Das & Pattanayak, 1993)	Two intrusive 0.3 mm diameter stainless steel electrodes coated with Teflon, except at the Tips.	Bubble-to-slug Slug-to-churn flow churn-to-annular	Vertical	Air-water		The criteria for different flow transitions are not similar. Therefore for each transition, a separate scheme of measurements has to be implemented. Cavitations extended a considerable length behind the probe.
(Devia & Fossa, 2003)	Ring-shaped & half-ring-shaped with different geometrical parameters	Annular, dispersed, and stratified flow		Air-water	N/A	A single electrode assembly proves to be suitable for producing a response for all flow regimes. Particle size strongly affects the probe response. The spatial resolution in this study was deduced.
(Cho & Ceccio, 2005)	Two flush mounted circular brass electrodes separated by a PVC substrate.	Stratified bubbly	Horizontal	Air-water	(Static & Numerical) Static test consisted of a water tank, and measured increasing liquid levels.	At least two electrodes must be used to determine the thickness of the liquid layer and the void fraction, although some a priori knowledge of the dimension of the layer is needed to set the electrode geometry. It is preferred to use impedance tomography techniques for more complex flow distributions.

In this experiment the study of the void fraction traces and their probability distribution functions facilitated the identification of six flow regimes: discrete bubble flow (consisting of a distribution of small size and spherical shaped bubbles), spherical cap bubbly flow (transition from bubbly to slug), stable slug flow (aerated slug flows separated by Taylor bubbles), unstable slug flow, churn flow (annular in nature with waves that bridge the tube wall) and annular flow. The electrical impedance technique of two-phase mixture can be obtained by measuring the difference in dielectric constant or electrical conductivity of each phase (Ming T Shu & Young, 1982). Impedance probes may be calibrated by using a pressure drop measurement or a quick closing valve system.

One important factor when using impedance probes is that drift will occur if the liquid conductivity changes. This was noted by (Geraets & Borst, 1988). If water temperature, for example, increases from 25 to 50°C, conductivity doubles while the relative permittivity decreases by approximately 15%. It was also mentioned that drift can be reduced by operating at a frequency high enough to give dominance to capacitance. The authors used a Boonton 72BD capacitance meter, capable of phase detection, operating at a frequency of 1 MHz. (Kelessidis & Dukler, 1989) have done extensive research on identification of flow regimes in air-water flows which is also worth mentioning. The next section presents a review on capacitance sensors used to measure void fraction.

2.4.4 Survey of Capacitance Sensors

Capacitance sensors have been used in numerous studies of measuring void fraction in two-phase flows. Capacitance sensors provide time-averaged void fraction measurements, and its time varying signal can be also used for flow pattern identification.

Given that the area of the plates and the gap distance is constant, the only input to a change in capacitance is due to a change in dielectric in the proximity of the electrode's electrostatic field. For two-phase flows, the dielectric consists of liquid-gas phases. The measured capacitance represents the amount of phases and configuration of the phases within the pipe. The first attempt to obtain useful information about a two-phase flow based on the difference in electrical permittivity was first explored at the beginning of the 1980s by (Abouelwafa, 1980). (Keska, 1999) made a comparison of four dynamic flow pattern techniques for multiphase flows. Both authors concluded that capacitive measurements have a high potential for flow pattern identification. A great deal of research on capacitance measurement techniques has focused on the design of void fraction sensors and transducers. In support of that principle, calibration techniques were desired to obtain calibration curves. Table 2.3 presents a summary of the list of electrode configuration studies and applications tested in atmospheric conditions for several orientations and for zero gravity conditions (Elkow, 1996; Elkow, 1997).

To reduce or eliminate the effect of asymmetric distribution, the helical electrode sensor has proven to be the most linear in calibration for concentration measurements from the list of researchers provided in Table 2.3. For local approach void fraction measurements of two-phase flows, measurements of liquid level data are required for developing correlations. A local approach void fraction measurement can be made by measuring the change in capacitance with a change in liquid level in the gap between the plates.

Table 2.3: Previous studies of void fraction measurements by capacitance techniques.

Author(s) by Reference	Electrode	Approach	Orientation	Diameter (mm)	Test Conditions	Calibration Technique
(Abouelwafa & Kendall, 1979)	Concave	Volume	N/A	25.00	Simulations & test	N/A
(Abouelwafa & Kendall, 1980)	6 configurations	Volume	N/A	12.5-5000	Water, gas, and oil	
(Ming T Shu & Young, 1982)	Concave	Volume	Horizontal	10.20		(QCV) and simulated stratified flows calibrated by cylindrical rods with similar dielectric properties
(Elkow, et al., 1996)	Helical	Volume	Vertical	9.53	Atmospheric	(QCV)
(Elkow, et al. 1997)	Helical and Concave	Volume	Vertical	9.53	Atmospheric and microgravity	(QCV)
(Tollefsen, et al. 1998)	Helical and Concave	Volume	Horizontal	42.00	Simulation & test	N/A., Poisson’s (FEM) method
(Lowe et al., 1999)	Concave	Local	Vertical	9.525	Micro-gravity	(QCV)
(Keska et al., 1999)	Concave	Local	Vertical	35.00	Atmospheric	Online calibration using a mixing chamber
(Jaworek, et al. 2004)	5 configurations	Local	Vertical	40.00	Atmospheric	Reference quartz frequency generator
(Dos Reis, et al. 2005)	Concave	Volume	Vertical and Horizontal		Atmospheric	Static calibration by incrementally adding liquid.
(Ahmed, et al. 2006)	Ring-Type and Concave	Volume	Horizontal	12.70	Oil and air	Canvas based phenolic rods
(Caniere, et al. 2007)	Concave	Local	Horizontal	9.00	Atmospheric	Calibrated with a high speed camera
(Golnabi et al., 2008)	Cylindrical probe	Local	N/A	12.00	Water	Reference capacitor
(Caniere et al., 2008)	Concave	Volume	Horizontal	9.00	Water and air	Calibrated with a high speed camera

The medium separating the plates is a composite of air and the dielectric fluid. Therefore the change in the liquid level in the composite made up of the dielectric fluid and the air in the sensing volume will result to a change in volume of both substances and a change in the overall capacitance. Various local approach experiments have been used to develop correlations between output signals and liquid level measurements.

It has been noted from previous experiments of measuring void fraction by capacitive sensors that the electrodes should be short in the longitudinal direction of the pipe (Caniere, et al. 2007; Jaworek, et al. 2004). This means that the electrode length should not exceed the diameter of the pipe. In this case, the capacitance is dependent upon the distribution of the vapor in the cross-section of the pipe. Several problems including stray capacitance, baseline drift, stability, and sensitivity have motivated the development of new transducers and measuring systems (Golnabi & Azimi, 2008). To improve some of the issues that exist in this field, a variety of capacitive sensor systems have been developed and reported. In this respect, for example the effects of guard ring electrode on the operation of a capacitive transducer have been investigated and have proven to have eliminated the effect of fringing effects to nearly negligible values.

CHAPTER 3

METHODS AND MATERIALS

In Chapter 3, the measuring tools, loop components, design requirements, and calibration techniques developed and used in the present study is discussed. It is important to know what a measuring tool cannot do as well as what it can do before a final selection is made. Each measuring tool has advantages and disadvantages, and the degree of performance is directly related to how well a measuring tool's capabilities and shortcomings are matched to the working environment and application. A thorough explanation of the selection of each measuring tool is provided in addition to decision matrices which were developed and used as a down selecting tool in the design process. The design requirements for the high heat flux heater developed for the present study is presented. The heater developed is not only a component for driving the loop, but it is also a measuring tool for surface temperature. The process developed for designing and calibrating the void fraction sensor is also presented. The next section presents a discussion on the layout of the loop diagnostic and measuring system developed and used in the present study.

3.1 Loop Measuring and Diagnostic System Design

The schematic presented in Figure 3.1 is a representation of the heat transfer spray cooling loop measuring and diagnostic system developed for the present study. The loop may operate without measuring tools. However, the purpose of the loop is to provide information about the physical behavior of the heated surface subjected to spray cooling. To obtain this information, one must incorporate adequate measuring tools at sufficient locations of the loop to measure system parameters. The measuring tools are digital measuring devices.

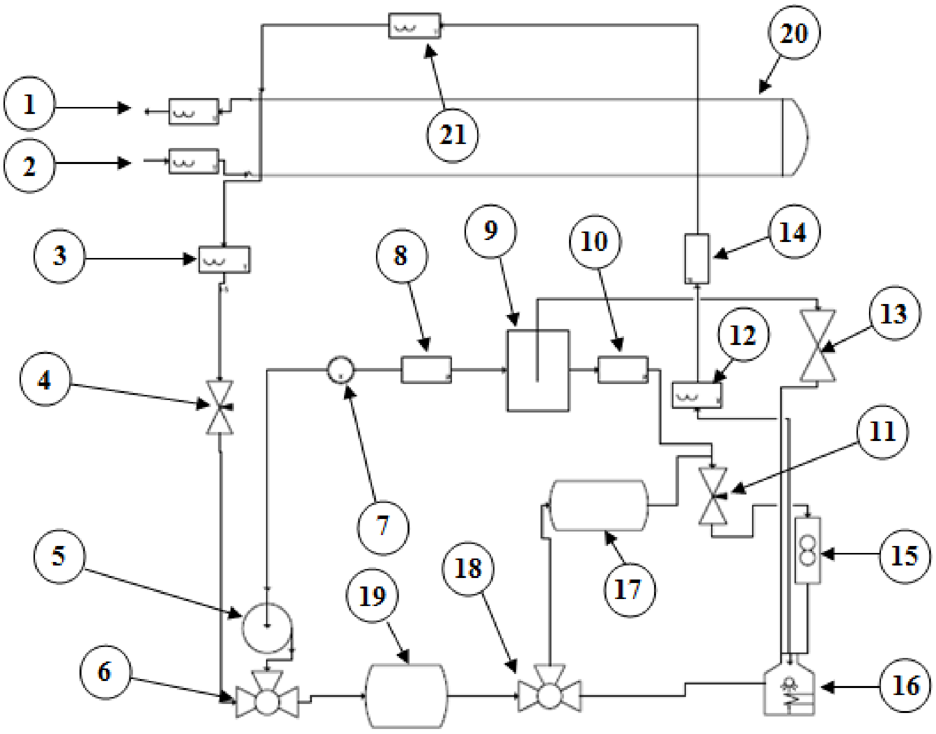

Figure 3.1: **Schematic of the measuring and diagnostic system for the heat transfer loop developed and used in the present study. (1, 2, 3, 12, and 21) are the thermocouples, (5) is the rotary pump, (7) is the void fraction sensor, (8, 10, and 14) are pressure transducers, (4, 6, 11, 13, and 18) are control valves, (15) is the flow meter, (16) is the high heat flux heater, (17 and 19) are liquid storage tanks, and (20) is the heat exchanger used.**

Each component and measuring tool is numbered in Figure 3.1. As shown in Figure 3.1, the loop consists of a variable rotary speed pump (5) which forces the two-phase liquid through a cyclone two-phase separator (9). The separator consists of a void fraction sensor (7) and a pressure transducer located at the entrance (8), as well as a pressure transducer at the outlet (10). The first pressure transducer (8) is located 0.114 m from the entrance of the separator and the second (10) 0.114 m from the exit. The void fraction sensor is positioned on the pipe line that routes the two-phase liquid from the pump to the separator. During a vaporization process the mixture appears as part liquid and vapor. Vapor quality has significance for saturated mixtures. Quality is one of the two independent properties needed to describe the state of the flow. As a result, the void fraction sensor is used to determine the state of the fluid flow.

The function of the separator is to separate the two-phase flow back into a single-phase liquid and vapor flow. The separator is designed to separate the phases by centrifugal force. The purpose of placing pressure transducers at the inlet and outlet of the separator is to monitor the pressure difference across the separator. The pressure difference is monitored to assure that the required pressure drop is achieved to separate the phases. A flow meter (15) is placed on the single-phase fluid flow pipeline to monitor the volumetric flow rate of the supply of fluid to the heater (16). When the fluid exits the separator, the flow passes into the heater and then through the heat exchanger (20) and chiller before returning to the pump and separator. Before the fluid reaches the heater, two liquid reservoir tanks (storage tanks) (17 & 19) were used to ensure sufficient supply of liquid to the loop. The function of the heater is to supply the required heat flux to the spray impingement surface. A thermocouple is used inside the heater chamber to monitor the ambient temperature of the chamber control volume. An additional thermocouple is also used to monitor the surface temperature of the heater. The purpose of using thermocouples in the heater is to measure the ambient temperature of the control volume and surface temperature of the heated surface to obtain the excess temperature. The excess temperature is defined as the difference of the surface temperature and the ambient temperature of the heater control volume. The heat exchanger used is a shell in tube heat exchanger. As the name implies, the function of the heat exchanger is to exchange heat between two fluids without mixing. A schematic representation of the heat exchanger is presented below in Figure 3.2.

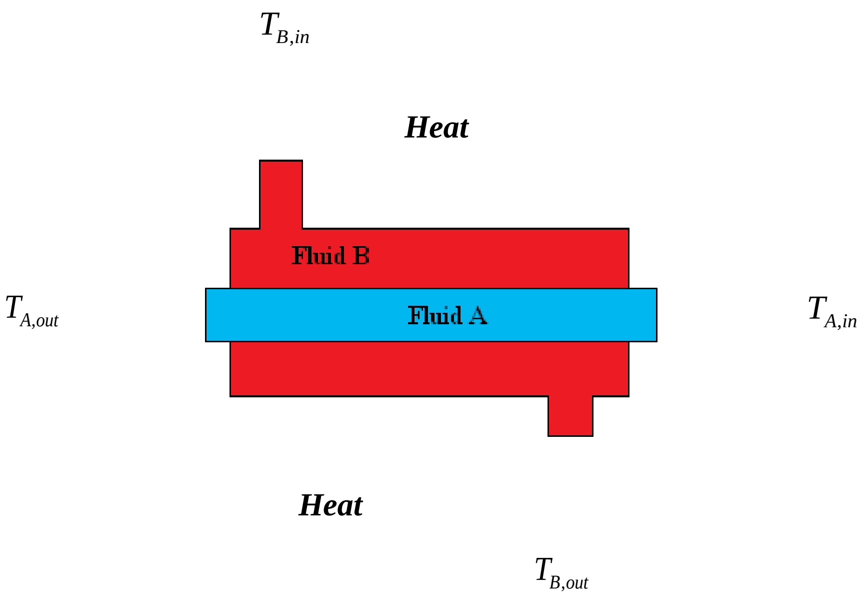

Figure 3.2: Schematic of the heat exchanger used in the present study.

The working fluid of the heat transfer loop passes within the annular tube of the heat exchanger and the fluid surrounding the annular tube is supplied by the chiller which removes heat from the fluid. Four thermocouples embedded in thermowells were used to monitor the performance of the heat exchanger. Two of these thermocouples were used to monitor the temperature of the working fluid entering and leaving the outer pipe surrounding the annular core of the heat exchanger (3 & 21). The remaining two thermocouples were used to monitor the temperature of the fluid supplied by the chiller entering and leaving the annulus of the heat exchanger (1 & 2). The flow rate is controlled by a series of valves (4, 6, 11, and 18) and the rotary pump.

3.2 Power Supply

There were two power supplies used in the present study. The power supply used to power the heater was a GPR-6015 HD DC power supply. The GPR-6015 power supply was not sufficient in supplying the required power to achieve a heat flux of 10,000 kW/m^2 (1000 W/cm^2) at the heater surface. The maximum output power that the GPR-6015 power supply could produce was 0.328 kW (328 W). As a result an Agilent Technologies 6030A power supply was purchased which is capable of producing the power required to achieve a heat flux of 10,000 kW/m^2 (1000 W/cm^2) at the heater surface. The Agilent Technologies 6030A power supply was not used in the present study because the AC power cord isn't a standard power input terminal. Modifications have to be done on one of the power outlets in the lab to accommodate the AC power cord for the Agilent Technologies 6030A power supply. Due to the time constraints on the completion of the present study, the GPR-6015 power supply was used to supply a generic power range for the heater. For future studies, the Agilent Technologies 6030A power supply will be used to power the heater and the corresponding electrical loop components. A photograph of the Agilent Technologies 6030A power supply is presented in Figure 3.3.

Figure 3.3: Photograph of the Agilent Technologies 6030A power supply.

The second power supply is an Integrated Power Designs SRW series power supply. The SRW series power supply was used to power the flow meter and pressure transducers. The SRW series power supply unit is enclosed in a vented 0.197 x 0.098 x 0.038 m metal case, and is cooled by free air convection. The SRW series power supply requires a 100-240 V_{ac} input and provides an adjustable output voltage range of up to 24 V_{dc}. A photograph of the power supply integrated into the heat transfer loop is provided in Figure 3.4. The next section presents a discussion on the data acquisition systems used.

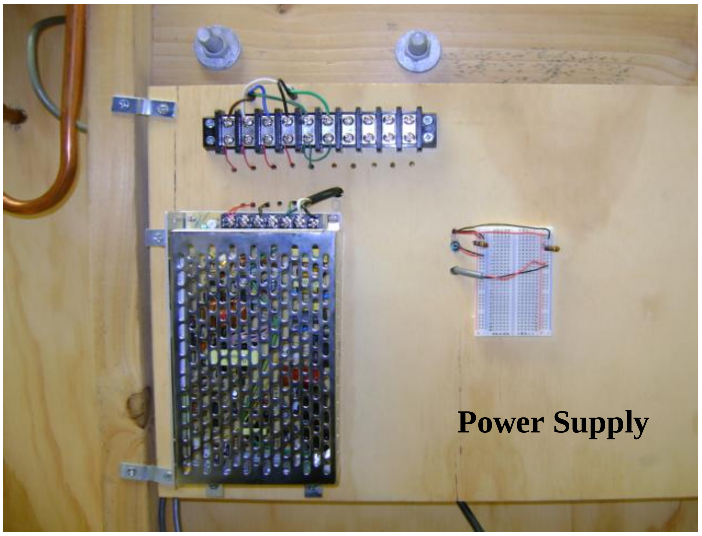

Figure 3.4: Integrated Power Designs SRW series power supply.

3.3 Data Acquisition System

There were two data acquisition systems used in the present study. The first data acquisition system used was a ChartScan/1400 data acquisition system. The ChartScan/1400 is a simple to use advanced hybrid strip chart data recording system. In addition to chart and spreadsheet displays, the ChartScan/1400 can easily display data in digital, analog, and bar graph format displays. The ChartScan/1400 does not require external signal conditioning or the use of multiplexers. The Chartscan/1400 is equipped with a 500 V isolation range for voltage measurements and 200 V for thermocouples which requires channel-to-channel isolation. The ChartScan/1400 can obtain data at a rate of up to 147 channels per second and includes a single channel burst mode for digitizing waveforms at rates up to 20 kHz. The Chartscan/1400 includes Chartview, a software program which provides a windows-based graphical-user-interface approach to obtaining data collection and data display. Figure 3.5 presents a screen capture of the data collection mode of Chartview. The Chartscan/1400 data acquisition system was used for data collection during the calibration stages of each measuring tool in the present study.

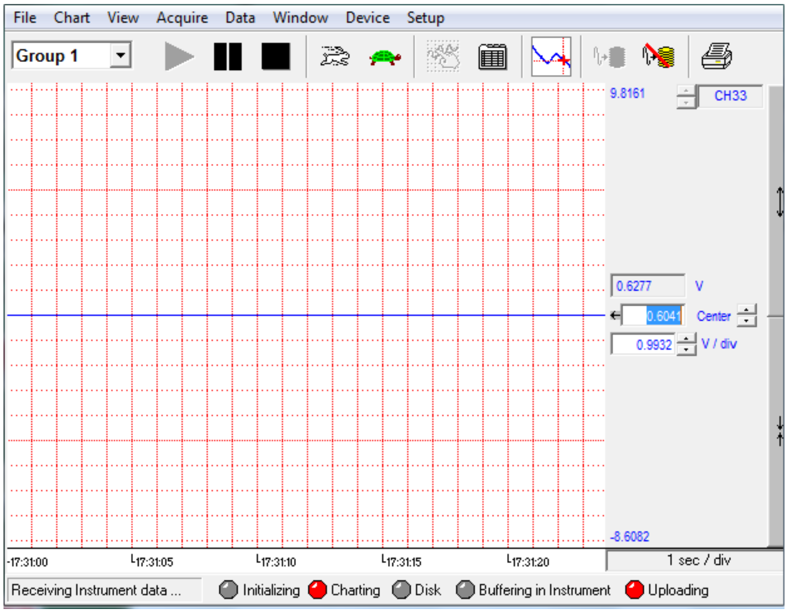

CH33

0.6277 V

0.6041 Center

0.9932 V / div

1 sec / div

Receiving Instrument data ...

Figure 3.5: Screen capture of Chartview software in charting data collection mode.

During the final stages of the present study, migration to an IOtech Data acquisition system was done for advanced data collection. The software used in the present study was Encore. Encore is the standard data acquisition software package that is included with each IOtech 6000 series module. In the present study, basic acquisition and generation options such as channel selection, acquisition rate, number of sampling points, and input range, and start and stop triggers were programmed for the loop measuring system. In addition channel mode selections were made within the channel view table which allowed the selection of measurement type, logging modes, regression calculation, and signal analysis. The IOtech Data Acquisition system is composed of two separate data collecting modules. These modules are a 6224 voltage module and a 6222 thermocouple module. The IOtech 6224 module is a twelve-channel, 24-bit resolution voltage measurement device which can be connected to the host PC's Ethernet port and can be synchronized with other IOtech 6000 series devices. The signal input module is composed of a set of twelve 2-position screw-terminal connectors located on the unit's front panels. Each of the twelve channels has its own internal circuitry that keeps the voltage source within the common-mode range.

The IOtech 6222 is a twelve-channel, 24-bit resolution thermocouple input module device. Up to twelve thermocouple inputs can be connected to each unit by the front panel removable screw-terminal connectors. Each of the channels has a TC+ and TC- connection. Each supports four thermocouple channels; and each module has a common terminal (COM) that is internally connected to an isolated ground reference. Within a module channel to channel can be within 1.5 V of each other and within 250 V to ground and within 250 V to one of the other two modules. The hardware provides the signal conditioning and acquisition engine, and the software defines the specific configuration and analysis aspects of the system. A photograph of the IOtech data acquisition system and the PC used is presented in Figure 3.6. The instrument panel was displayed with the drag-and-drop interface data view window. The data view window only allows three instrument panels to be viewed consecutively. Also, data can be exported to other formats including Excel and ASCII. The IOtech data acquisition system collected data for the flow meter, pressure transducers, thermocouples, and the void fraction sensor. The next section presents a discussion on the chiller used. Figure 3.7 presents a photograph of the data acquisition instrument panels. The instrument panels generated in the data acquisition software allow the user to monitor and record data from the system.

P.C.

IOtech data acquisition system

Figure 3.6: Photograph of the IOtech data acquisition and pc used in the present study.

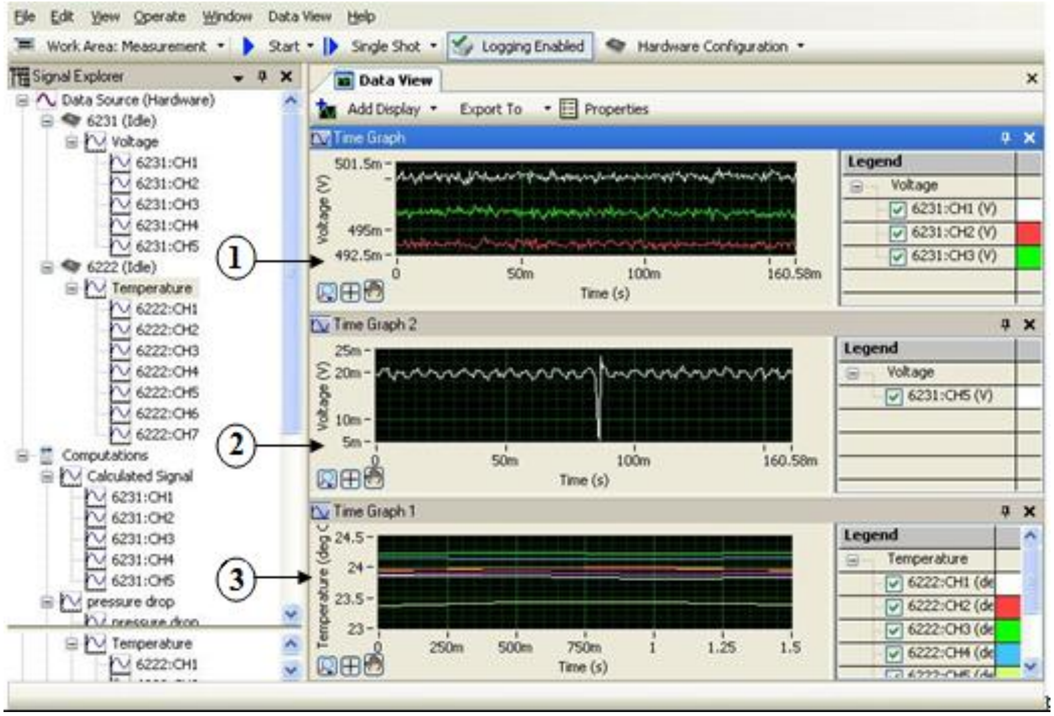

Figure 3.7: Data acquisition instrumentation panel: (1) pressure instrument panel, (2) flow meter instrument panel, and (3) temperature instrument panel.

3.4 Cornelius REMCOR CH750-A Chiller

The chiller used is a programmable Cornelius REMCOR CH750-A series chiller. The Cornelius CH750-A chiller is used to supply cooled liquid to the heat exchanger. Figure 3.8 presents a photograph of the chiller. The options of the chiller include a reservoir, temperature controls, and pump to provide a self contained liquid cooling/circulation system. The control temperature is sensed on the outlet of the chiller. The next section presents a discussion on the high heat flux heater and the design process developed and used.

Figure 3.8: Photograph of the Cornelius REMCOR CH750-A series chiller used in the present study.

3.5 High Heat Flux Heater Design Requirements

The present study consisted of three heater designs: designs A, B, and C. Design A was developed by (Davis, 2010). Design A consisted of a pure copper block imbedded with cartridge heaters. A CAD drawing of design A is presented in Figure 3.9. Design A was observed to present large heat losses and heat flux measurement uncertainties. As a result, the shortcomings mentioned for design A provided the design requirements for the heater developed for the present study. The following discussion will present the design requirements for the high heat flux heater developed for the present study.

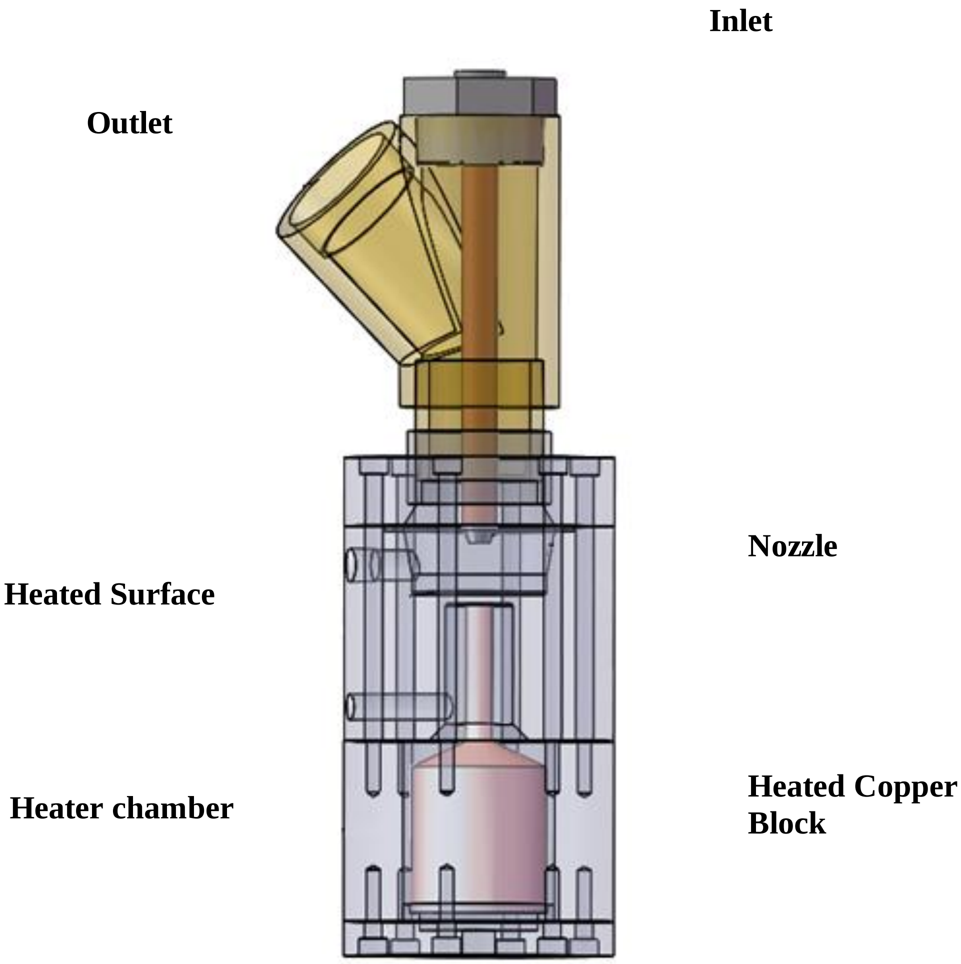

Figure 3.9: CAD drawing of heater Design A consisting of a pure copper block with cartridge heaters as the heating source, developed by (Davis, 2010).

The design requirements for the heater were as follows:

1. The heated surface area was to be 1 cm^2.
2. The desired maximum heat flux was to be 1000 W/cm^2.
3. The distance from the heating source to the heated surface area was to be small to minimize heat losses, therefore eliminating the need for a neck region (heat focusing block).

4. The heater was required to be a measuring tool for surface temperature.

3.6 Thick Film Resistors

Given that design A was large in size and incorporated cartridge heaters as the heating source, thick film resistive heaters were used as an alternative heating source due to their small size and heating time. Thick film resistors are much smaller and the heating time is much less when compared to cartridge heaters. The size of heating sources is a vital factor in the design of high heat flux heaters when considering heat losses for the size of the heating area/volume. Heating time is important when considering start up and shut down time between loop runs. Thick film resistors are cheap in cost compared to cartridge heaters.

Thick film resistors are available in a range of types. These types are chip, leaded, and flanged. Thick film resistors also vary in surface areas from 0.0001 m^2 to 0.0006 m^2 (1 cm^2 to 6 cm^2). In heater applications, the backside of thick film resistors are faced toward the unheated surface and the power input leads. The most common type of thick film resistor has a metallic bottom because the backside of the resistor can be soldered onto the cooling substrate. Soldering the electrical leads onto a thick film resistor can be a tedious task, because the resistor's contact pads are fragile. Soldering an array of thick film resistors can also be difficult. A photograph of a thick film resistor is presented in Figure 3.10.

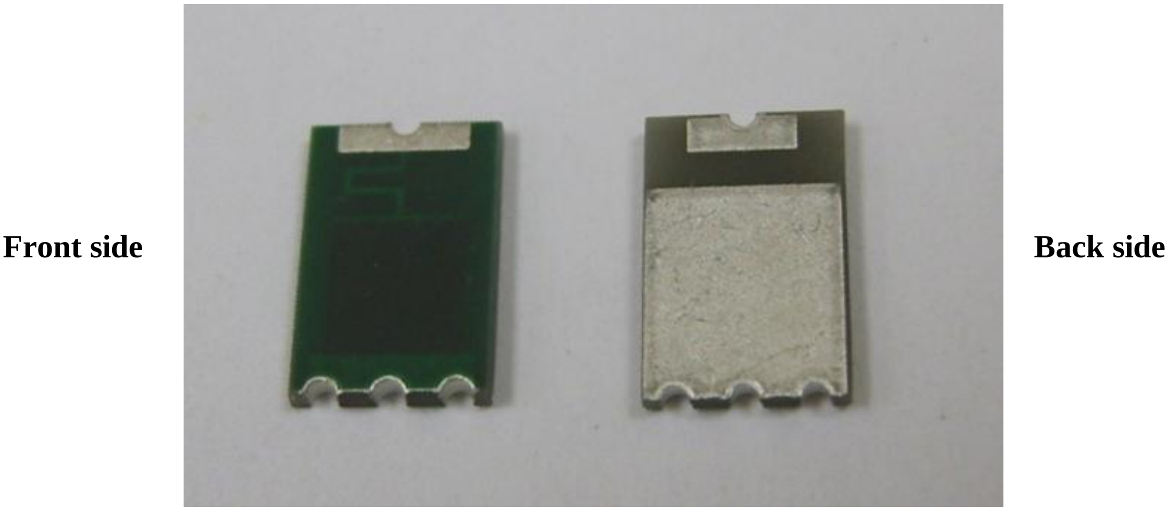

Figure 3.10: Photograph of a thick film resistor.

If thermocouples are used for measuring temperature differences in the heater, the thermocouples cannot touch the green resistor film or they will become energized and burn out. Also thick film resistors have a small operational window. Thick film resistors can’t operate in the range above 110 to 200°C or they will fracture. Thick film resistors operate well with coolants that have boiling points below 60°C and poorly for ones that have boiling points above 100°C like water. The next section presents a discussion on the methodology for the heater design.

3.7 Surface Material Selection for the Heater

Once the maximum heat flux has been identified, the heated surface material can be selected. This requires knowledge of the temperature rise of thermal conductive materials based on the desired maximum heat flux. Table 3.1 was generated to express the temperature increase of thermal conductive materials as a function of heat flux. Table 3.1 lists the temperature increase of various thermal conductive materials at a heat flux of 10,000 kW/m^2 (1000 W/cm^2). Eqn. 3.1 was used to calculate the temperature increase of the conductive materials. The material properties were obtained from (F.P. Incropera, 2007).

$$\Delta T = \frac{\dot{Q}\,X}{k} \tag{3.1}$$

From Table 3.1, copper deems to be the most suitable surface heating material for a maximum heat flux of 10,000 kW/m^2 (1000 W/cm^2). As a result, copper was used as the heating material for the heater developed in the present study. The next section presents a discussion on the heater design used in the present study.

Table 3.1: List of temperature required to give 10,000 kW/m^2 for various materials.

Heat Flux (kW/m^2)	**Metal**	**Melting Point (K)**	**Conductivity (W/m·k)**	**Distance (m)**	**Temp Increase (K)**	**Overheated**
10,000	Pure Copper	1358	401	0.01	249	No
10,000	Pure Aluminum	933	237	0.01	422	No
10,000	Aluminum 1100	913	220	0.01	455	No
10,000	Red Brass	990	160	0.01	625	No
10,000	Stainless Steel	1670	15	0.01	6667	Yes

3.8 Heater Designs

For the heating element used in the present study, a high temperature 0.0254 m diameter glass mica ceramic base was used to house the resistors and power input leads. The glass mica also served as a thermal insulator. A CAD drawing of the heating element developed is presented in Figure 3.11. Four thick film resistors arranged in a parallel were used as the main heating source. Each of the thick film resistors has a surface area of 0.00006 m^2 (0.6 cm^2), a power output rating of 0.15 kW (150 W), an electrical resistance of 50 Ω, and maximum operation temperature of 100°C. The four resistors arranged in parallel provide a maximum heat flux of 10,000 kW/m^2 (1000 W/cm^2) and an equivalent resistance of 12.5 Ω. As shown in Figure 3.11a, three copper electrode leads were used to provide the input power to the resistors. Figure 3.11c depicts the electrical wires coming from the base of the ceramic housing.

Design B consisted of the heating element enclosed in a stainless steel bolt. The resistors were mounted in the resistor reservoir between the ceramic base and the heated surface in a compression fit manner as shown in the cutaway view in Figure 3.12. Design B was not used because during testing it was observed that the resistors caused heat to spread across the stainless steel surface, and as a result heat traveled down the sides through the threads providing rigorous heat losses. A CAD drawing of design C is presented in Figure 3.13. Design C consisted of mounting the heating element on top of the stainless steel bolt, and incorporated a thin 0.00254 m copper disc with a protruding 0.0121 m diameter heating surface, providing a heating surface area of 0.0001 m^2 (1 cm^2). This is a much more effective approach because the heat is focused directly to the 0.0001 m^2 heated surface area and the maximum power supplied by the resistors is 10,000 kW (1000 W). A machined rectangular hole was placed on the side of the heater to accommodate a thermocouple for monitoring surface temperature.

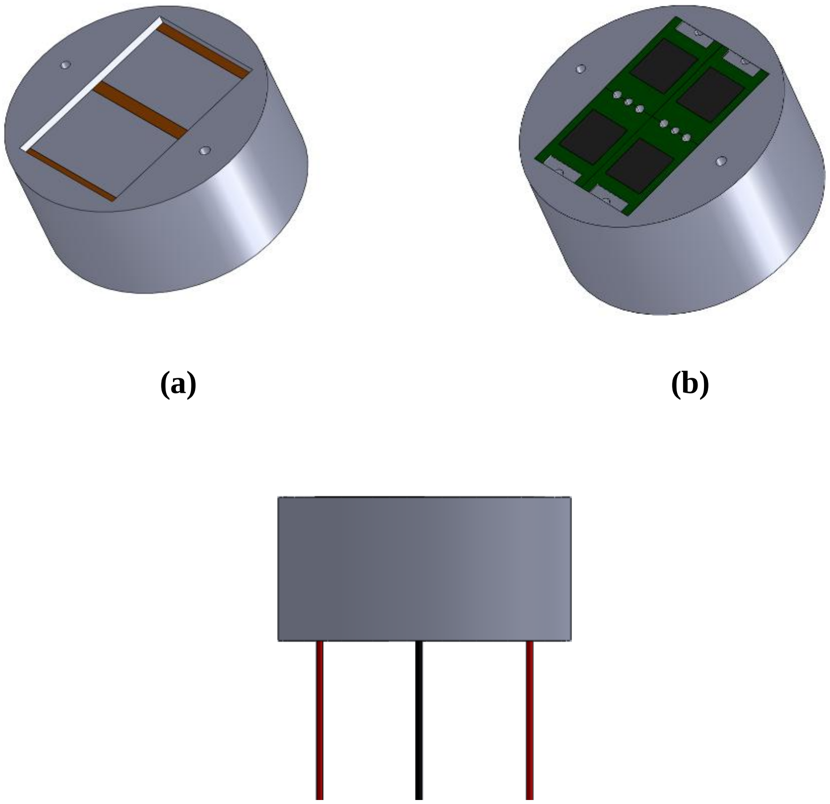

(a)

(b)

(c)

Figure 3.11: CAD drawing of the thick film resistive heater element developed and used in the present study. (a) Ceramic base with copper power leads. (b) Ceramic base with thick film resistors mounted in place. (c) Side view of the full assembly with the electrical wires.

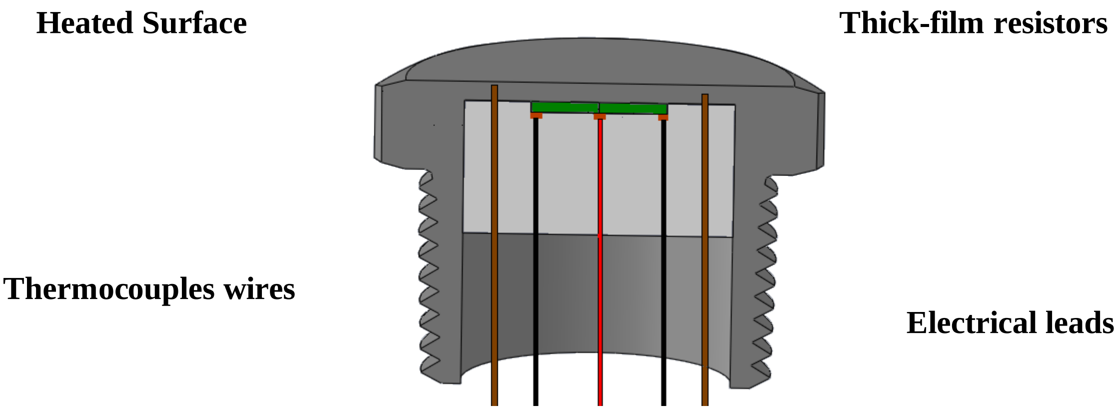

Figure 3.12: Cutaway view of heater Design B.

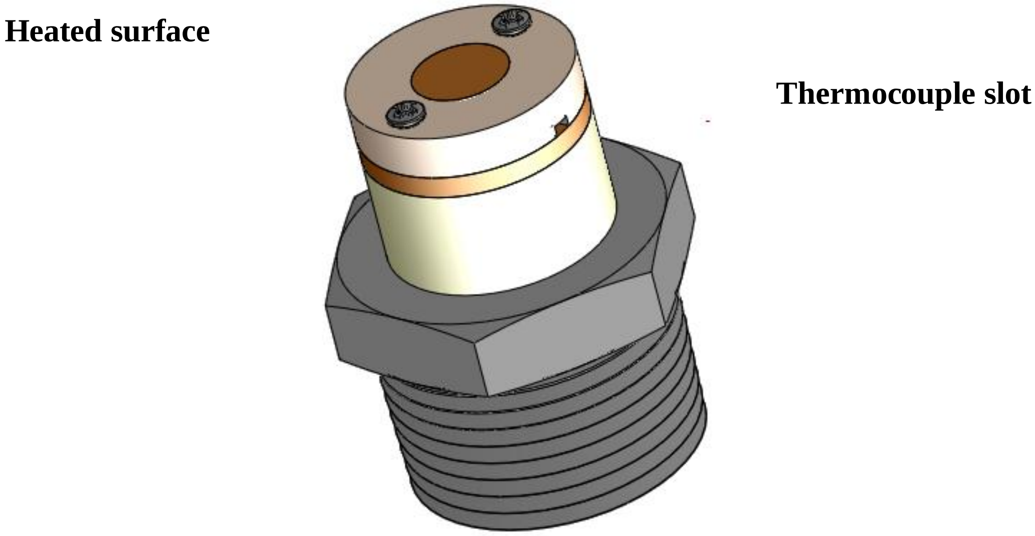

Figure 3.13: CAD drawing of heater Design C.

By using design C, one can easily and effectively obtain a heat flux of 10,000 kW/m^2 (1000 W/cm^2). It can also be assured that since the heat is directed straight to the top surface, an even temperature distribution exists. This can be verified by scaling and a finite element or finite volume analysis. Regardless of the heater design, a preliminary scaling analysis should be done on the equations which describe the physics of the system. This is done in order to validate whether a finite element or finite volume analysis should be done to study the temperature distribution in the conducting material before the design is finalized. Figure 3.14 presents a schematic of the heated surface and the coordinate system used in the scaling analysis. The x and z-direction are taken to lie on the same coordinate plane, and are symmetric about the y axis. Therefore the z-direction can be neglected, leaving only the x and y-direction. The problem is therefore reduced to a 2-D problem. The next section will discuss the heater scaling analysis.

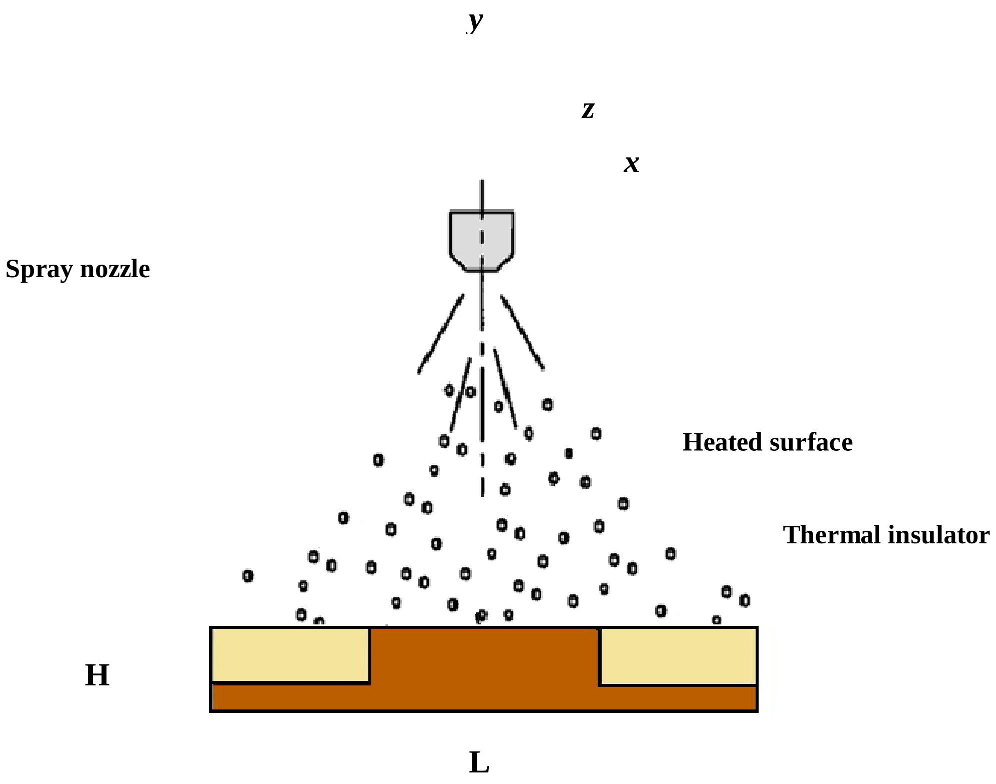

Figure 3.14: Schematic of the heated surface used in the present study subjected to spray cooling.

3.8.1 Heater Scaling Analysis

Scaling analysis is a procedure for obtaining the appropriate dimensionless groups for the basic equations which describes the physiological nature and behavior of the system to be analyzed. The equations which describe the physics involved with the performance of the heater design are: the continuity, x-momentum, and energy equation:

$$\frac{\partial u}{\partial x}+\frac{\partial v}{\partial y}=0 \tag{3.2}$$

$$\rho\left(u\frac{\partial u}{\partial x}+v\frac{\partial u}{\partial y}\right)=-\frac{\partial P}{\partial x}+\mu\left(\frac{\partial^2 u}{\partial x^2}+\frac{\partial^2 u}{\partial y^2}\right) \tag{3.3}$$

$$\rho c_p\left(u\frac{\partial T}{\partial x}+v\frac{\partial T}{\partial y}\right)=k\left(\frac{\partial^2 T}{\partial x^2}+\frac{\partial^2 T}{\partial y^2}\right) \tag{3.4}$$

The final form of Eqns. 3.2, 3.3 and 3.4 after scaling is:

$$\frac{\partial u^*}{\partial x^*}+\frac{\partial v^*}{\partial y^*}=0 \tag{3.5}$$

$$\frac{1}{A^2}\left(u^*\frac{\partial u}{\partial x}+v^*\frac{\partial u}{\partial y}\right)=-\frac{\partial P^*}{\partial x^*}+\frac{1}{\mathrm{Re}}\left(\frac{1}{A^2}\frac{\partial^2 u^*}{\partial x^{*2}}+\frac{\partial^2 u^*}{\partial y^{*2}}\right) \tag{3.6}$$

$$\frac{1}{A^2}\left(u^*\frac{\partial T^*}{\partial x^*}+v^*\frac{\partial T^*}{\partial y^*}\right)=\frac{1}{Pe}\left(\frac{1}{A^2}\frac{\partial^2 T^*}{\partial x^{*2}}+\frac{\partial^2 T^*}{\partial y^{*2}}\right) \tag{3.7}$$

A more detailed explanation of the scaling process can be found in Appendix E. The numerical value of the aspect ratio $A=L/H$ is 14.11. The aspect ratio serves to diminish the forces which have a minimum effect on the system, and indicate which forces are dominant. In this analysis, it is apparent that the viscous forces in the x-direction are negligible for the x-momentum equation, Eqn. 3.6. Similarly, the temperature gradient in the x-direction is also negligible in the x-direction for the energy equation compared to the y-direction. As a result, excluding the x-direction terms for both equations reduces the problem to a 1-D analysis, indicating that the gradients in the y-direction are dominant. Therefore, a finite volume analysis on the system was not necessary. A more conclusive explanation is that the temperature distribution on the heated surface is uniform due to the heat being focused directly to the top.

3.8.2 Heater Testing

Figure 3.15 presents a photograph of the heater setup for testing the heater in open atmosphere. After the heater parts were fabricated and assembled, two tests were conducted on the heater. The first test was conducted to obtain the equivalent resistance of the resister arrangement in the heater. A multimeter was used to measure the resistance across the electric power leads of the heater. The equivalent resistance of the four unused resistors in the heater was 12.5 Ω. The second test consisted of testing the heater in open atmosphere to obtain an expression for surface temperature as a function of power.

The resistors discolored after multiple uses as shown in Figure 3.16. After the resistors operated over time and beyond their operational temperature limit, the equivalent resistance of the resistors changed. After testing the heater at temperatures beyond 100°C for long periods of time the equivalent resistance of the resistor arrangement changed to 22 Ω. This was found to be due to excessive usage and age of the resistors. It can be said that if the resistors are operated beyond their operational temperature limit, the performance of the heater is affected by a change in resistance. Also, during the second test the voltage and corresponding electric current was measured using a multimeter and recorded as the power was increased.

Figure 3.15: Photograph of heater testing setup.

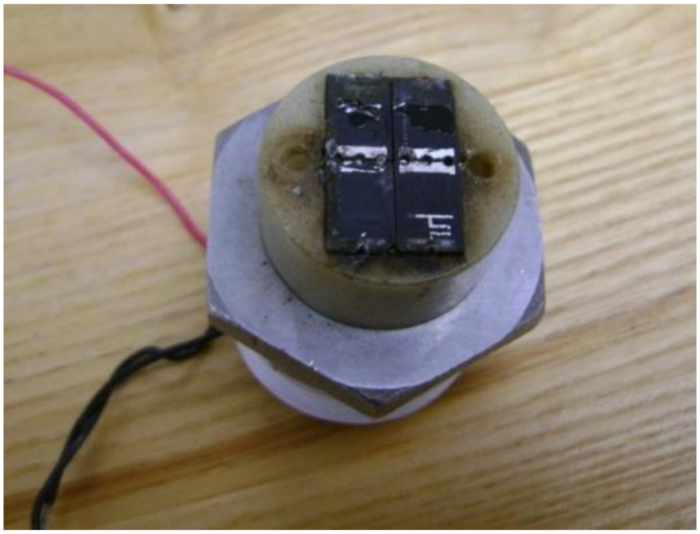

Figure 3.16: Photograph of aged and discolored thick film resistors in the heater.

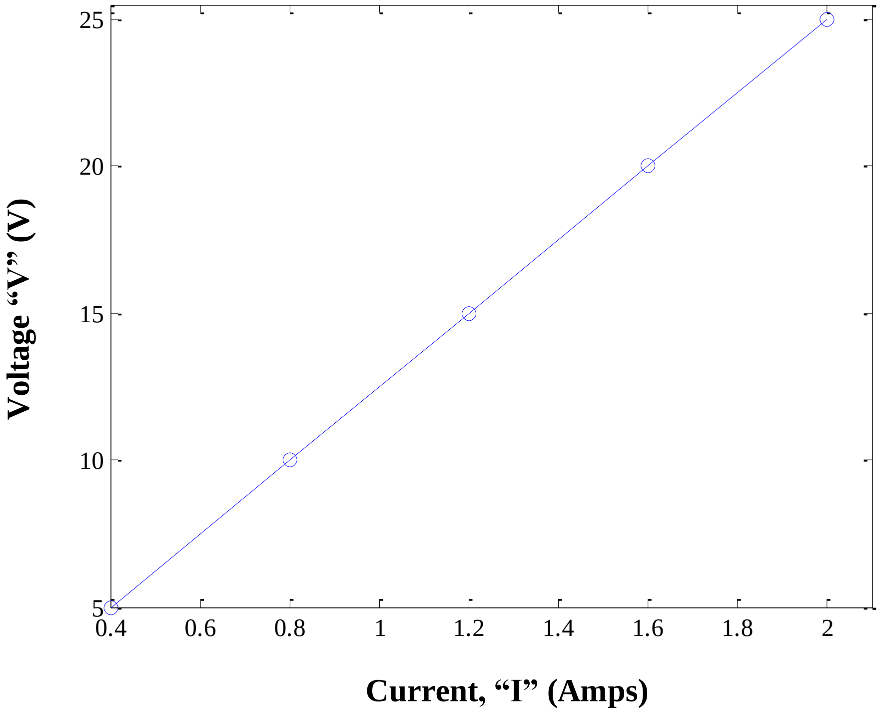

Figure 3.17: Plot of voltage vs. current for the heater developed and used in the present study.

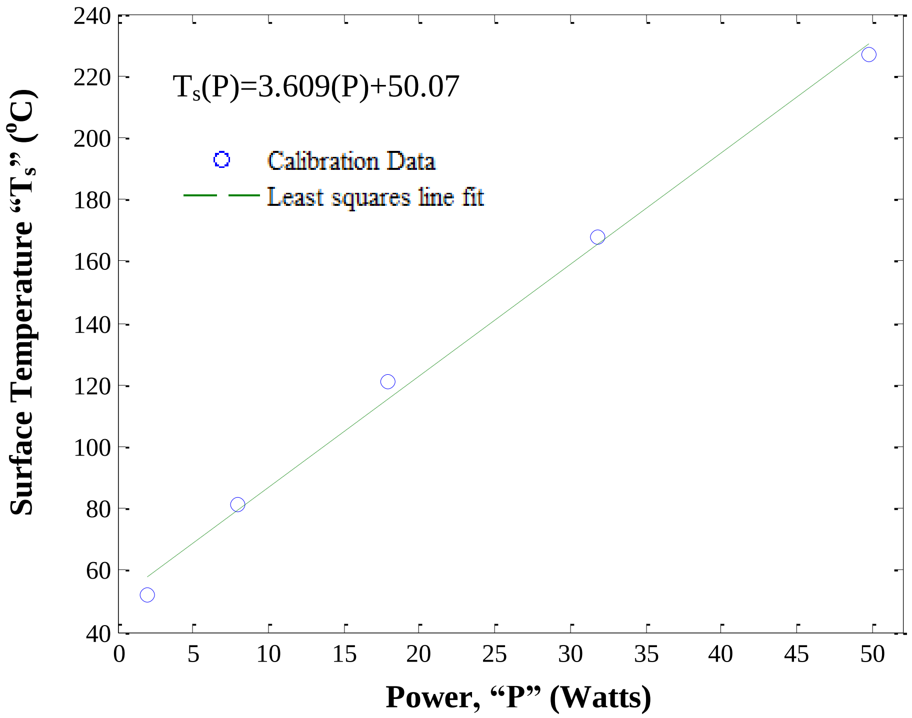

Figure 3.18: Calibration plot of surface temperature vs. power for the heater developed and used in the present study.

Figure 3.17 presents a plot of voltage vs. current for the heater during testing. The trend of the plot obeys Ohm's law of a linear resistance. The slope of the line in is 12.5 Ω. Figure 3.18 provides a plot of surface temperature vs. input power and the linear regression expression obtained. Figure 3.19 is a photograph of the heater mounted in the heater chamber. The heater chamber used was also developed by (Davis, 2010). The process discussed for calculating the total uncertainty is applied to the calibration procedures for all the measuring tools used in the present study.

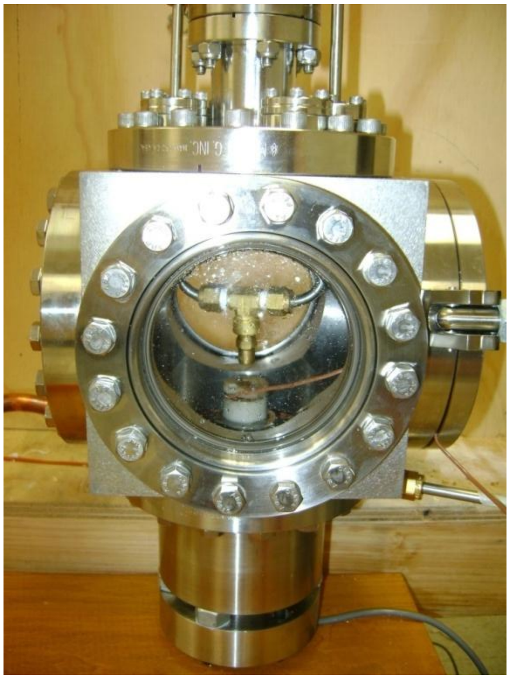

Figure 3.19: Photograph of the heater installed in the heater chamber used in the present study.

3.9 Flow Measuring Device Selection Process

A variety of flow meter device types were considered for the present study. Decision matrices were developed and used as a down selecting tool in the selection process. The most important requirement for selecting the flow meter for the present study was to know exactly how the device operates.

The requirements for the flow meter were as follows:

1. The flow meter was required to have a linear output voltage signal.
2. The flow meter must be able to monitor flow rate for the working fluid.

3. The flow meter must be able to monitor flow rate for the flow rate range of the heat transfer loop.

The next section presents a discussion on the type of flow meters that were considered.

3.9.1 Flow Meters Device Types Considered

There are a variety of methods to measure flow rate. Table 3.2 provides a list of commonly used flow meter device types that are used in spray cooling applications. Table 3.3 presents the decision matrix that was developed and used as a down selecting tool for the flow meter device type selection process. From the decision matrix listed in Table 3.3, a linear flow metering device type was deemed to be the most suitable flow metering device type for the present study. The following presents a discussion on the reason why the alternative choices were not used.

Table 3.2: List of flow measuring device types and specifications.

Mechanism	Nominal Accuracy*	Flow-sensitive or summing element	Operating Range
Restriction flow meters	Dependent on the differential pressure device	Nozzle type opening	4.0:1.0 Range
Linear flow meters	0.05	Float type, turbine, vortex, and electromagnetic	0.25-160 l/min
Traversing Methods	0.20	Thermal anemometers	0-38,100 l/min

Restriction flow meters for internal flow are based on acceleration of a fluid stream through a diverging area in which the differential pressure is measured using a pressure measuring instrument. The flow rate can then be inferred using a theoretical analysis or an experimental correlation device. The most popular restriction flow metering devices are orifice and Venturi meters. An orifice meter consists of an orifice plate with a machined hole in the center. The orifice plate is positioned between two straight pipes in length, usually flanged. When the fluid enters the orifice, it must accelerate due to the flow area being reduced.

Table 3.3: Decision matrix for selecting the flow metering device type.

Criteria	**Weight, W%**	**Flow metering device types**		
		(1)	**(2)**	**(3)**
Accuracy	35	20 **35**	10 **35**	5 **35**
Functionality	25	5 **25**	15 **25**	5 **25**
Cost	25	5 **25**	15 **25**	5 **25**
Ease of Use/ Stability	15	5 **15**	15 **15**	15 **15**
Total	**100**	35 **100**	55 **100**	30 **100**
Selection Models: (1) Restriction flow meters, (2) Linear flow meters, and (3) Traversing methods.				

The Bernoulli's equation describes the corresponding pressure drop that takes place and is also used to correlate the theoretical mass flow rate. An orifice meter was not used because a manufactured orifice meter requires at least 12 feet (3.658 m) of piping from the pipe connection adapters to achieve the correct pressure drop to correlate a flow rate reading. As a result, the orifice meter is not space accommodating. The Venturi meter consists of a conical entrance and exit section connected by a reduced cross sectional area in length. The reduced area section is recognized as the throat of the Venturi.

Similar to the orifice meter, the Venturi meter is also based on the reduction of flow pressure accompanied by an increase in velocity. The pressure drop experienced is used to measure the rate of flow through the Venturi meter. On the discharge side of the meter the fluid velocity is decreased and the original pressure is recovered. Because of the shape of the Venturi element, the pressure losses in a Venturi meter are less than in an orifice meter. The derivation and clarification of the correlation between theoretical mass flow rate and pressure drop can be found in (Fox R., 2004). A Venturi meter was not used because a Venturi meter requires molding and casting of the Venturi element. The facilities used for machining parts for the present study were not capable of casting or molding a Venturi element. For the present study it was preferred to select a flow metering device type that could be purchased commercially rather than develop a flow meter that is complicated to machine and fabricate. Aside from the complication of fabricating and providing space for restriction flow meters in the loop, the main disadvantage of restriction flow meters is that the measured pressure drop is not linear with flow rate.

Hot-wire anemometers were considered for traversing methods. Hot-wire anemometers measure local instantaneous flow velocities. The hot-wire anemometer, which is primarily a technique for measuring local fluctuation velocity in a flow, has always been an exceptionally vital flow measuring instrument in the study of laminar and turbulent flows. The fundamental principle behind the performance of the hot-wire anemometer is the heat transfer between the fluid stream and the wire in the flow field can be used to infer a flow velocity measurement. The hot-wire anemometer can be either a constant temperature system setup or a constant heat flux system setup. A more extensive explanation and review of hot-wire anemometry can be found in Fox R., 2004. A hot-wire anemometer was not used mainly due to the cost of commercially available hot-wire anemometers. Also when considering fabricating hot-wire anemometers for the present study, the long fabrication time is not worth the effort.

In many applications, including the present study, it is advantageous to use linear flow meters that produce output signals linear to flow rate. Several linear flow meters are available commercially. Among the most simple and easy to use linear flow meters are the electromagnetic flow meters. The electromagnetic flow meter uses the principle of magnetic induction. A magnetic field is produced across the pipe and when a conductive fluid passes through the field, a voltage is generated at right angles to the flow field and velocity vectors. Electrodes are placed on the outer perimeter of the pipe to detect the output voltage signal. The output voltage signal is proportional to the average axial velocity when the profile is axisymmetric. Electromagnetic flow meters may be used in applications where the fluid has an electrical conductivity above 100 microsiemens per meter (1 Siemen = 1 Ampere per volt). An electromagnetic flow meter was used for the present study due to its accuracy, cost, functionality, and ease of use. Table 3.4 presents the decision matrix used for selecting the electromagnetic flow meter used for the present study.

Table 3.4: Decision Matrix for selection the flow metering device.

Criteria	**Weight, W%**	**Flow Metering Device Model Selection**	
		(1)	**(2)**
Accuracy	35	20 **35**	20 **35**
Functionality	25	15 **25**	5 **25**
Cost	25	15 **25**	5 **25**
Ease of Use/ Stability	15	5 **15**	15 **15**
Total	**100**	55 **100**	45 **100**
Selection Models: (1) Ifm Efector SM6000 and (2) Ifm Efector SU series ultra sonic flow meter.			

From the decision matrix provided in Table 3.4, the SM6000 flow meter deemed to be the most suitable choice for the application when considering the accuracy, functionality, cost, and ease of use. Before the electromagnetic flow meter was selected, the expected flow rate range of the heat transfer loop had to be known. For this study, the expected flow range was obtained by performing a mass balance on the heated surface. The mass balance was done in order to obtain the required mass flow rate to maintain the desired heat flux. The flow analysis can be found in Appendix C. The next section presents a discussion on the calibration procedures developed and used for the electromagnetic flow meter used.

3.9.2 Flow Meter Calibration

The calibration technique of the SM6000 electromagnetic flow meter involved a dynamic flow calibration. The SM6000 contains an LED display which allows instantaneous reading of volumetric flow rate. The calibration setup consisted of a fluid pump and control valve as shown in Figure 3.20. The pump forced the fluid through the control valve and flow meter. The control valve was used to control the rate of flow. As a result, different flow settings were achieved, and the output signal was recorded with the data acquisition in comparison with the reading of the LED display. The flow rate reading of the LED display was also verified using a digital stop watch which was used to time the flow as it entered a beaker. A plot of the calibration data and linear regression expression is presented in Figure 3.21. The uncertainty measurements obtained from the calibration tests are discussed. The manufacturer stated accuracy of the Ifm Efector SM6000 series electromagnetic flow meter was 0.2% (F.S.), and the uncertainty from the measurements was found to be ±0.013 l/min. The residual from the calibration plot was found to be 0.9863. The maximum error in the simplistic fit is 0.06913 l/min. The next section will discuss the temperature measuring devices used.

Figure 3.20: Photograph of the flow meter calibration setup developed and used in the present study.

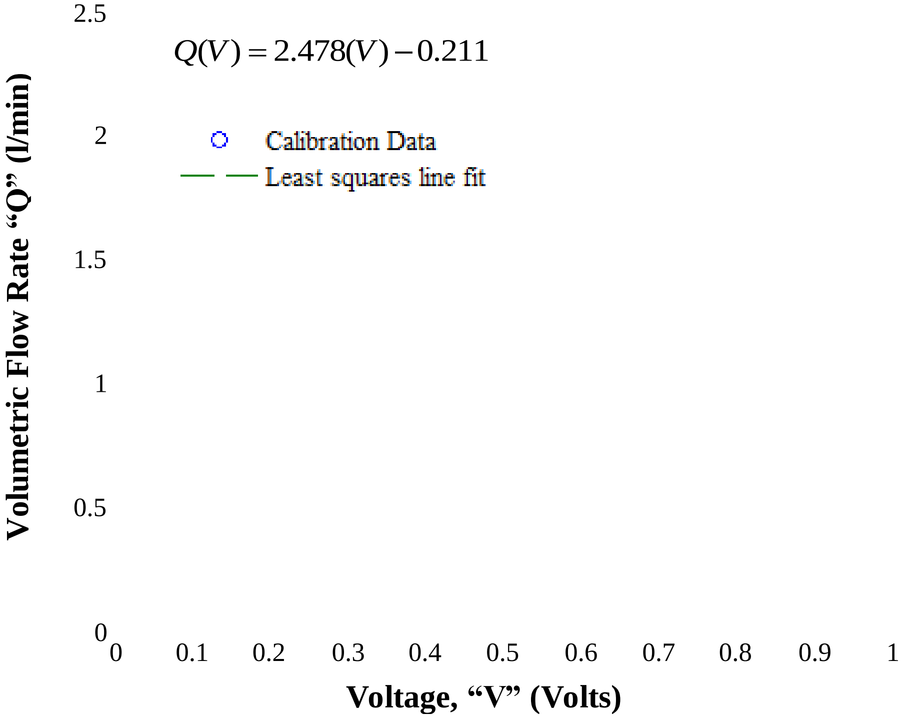

Figure 3.21: Calibration plot of the 0-25 l/min Ifm Efector SM6000 series electromagnetic flow meter.

3.10 Temperature Measuring Device Selection

An extensive variety of measuring instruments are available to acquire temperature measurements. A number of these instruments convert temperature directly to an electrical signal while others can be used in combination with an electrical transducer to convert the temperature signal into an electrical form. In addition to accuracy, special attention must be provided for: response time, linearity, noise sensitivity, long-term stability, and ambient conditions when temperature systems are designed or utilized. The most common temperature measuring instruments are listed in Table 3.5. The instruments used to measure temperature in the present study were K-type thermocouples.

Table 3.5: List of temperature measuring device types and specifications.

Mechanism	Nominal Accuracy*	Operating Range
Bi-metallic strips	0.10	-40°C to 500°C
Thermocouples	0.40	-270°C to 2800°C
Resistance-temperature detectors (RTDs)	0.03	-270°C to 850°C
Thermistors	0.01	-270°C to 600°C
Semiconductor temperature sensors	0.01	-100°C to 300°C
Radiation pyrometer	0.025	-50°C to 10,000°C

Thermocouples are widely used in spray cooling applications due to the temperature range and measurement sensitivity range requirements. The operating principle of a thermocouple is based on two dissimilar metal wires joined together at a point. The point of joining is heated or cooled and a voltage difference is generated across the remaining unheated ends. This principle is referred to as the Seebeck Effect. The magnitude of the resultant voltage difference due to the Seebeck Effect is quite small (on the order of millivolts). For example, a K-type thermocouple develops approximately 0.04 mV/^{o}C. The thermocouples wires used in the present study were TT-K-30 insulated duplex wires supplied by Omega Engineering. Six ten foot long thermocouple wires were cut and welded using a Hotspot thermocouple welder. A photograph of the thermocouple welder is provided in Figure 3.22. The following section presents a discussion on the procedures developed and used to make the thermocouples.

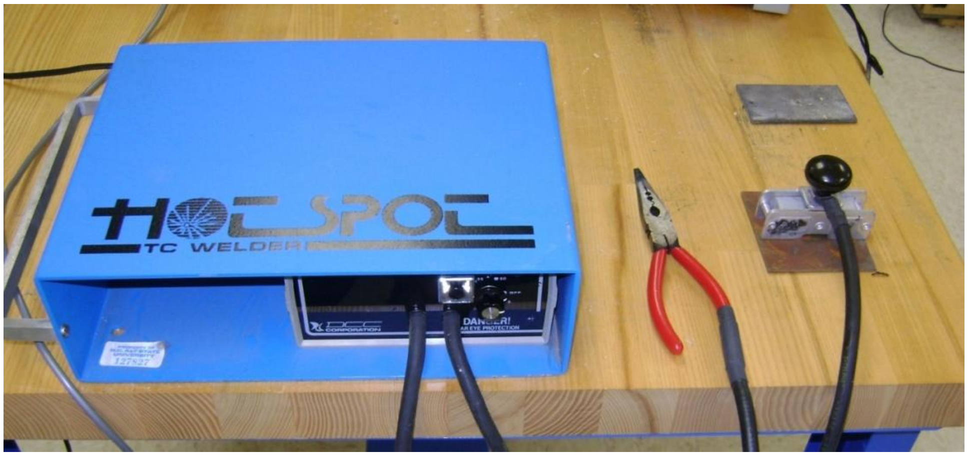

Figure 3.22: Photograph of the DCC Corporation Hotspot thermocouple welder.

For welding preparation purposes, approximately 12 mm of wire insulation were stripped from the thermocouple wires. The bare wires were then twisted together. Using side cutters, the wire ends were cut off square leaving sufficient un-insulated material, providing approximately 1 mm of wire protrusion for gripping the wires with welding pliers. The wires were held side by side in the welding pliers to ensure that the wires were in firm contact with each other and trimmed off square before welding. The following section presents a step by step procedure for welding the thermocouple wires:

1. Turn the system on and set the energy level to the desired value. The energy level required to weld the thermocouple wires are different for different wire gauge sizes.
2. Prepare the wires to be welded and gripped in the pliers, leaving about 1 mm or more of protruding wire.
3. Position the wires 0.005 or 0.006 m (5 or 6 mm) in front of the ground plate on the welder, whilst steadying the hand.
4. Press the “weld” button and slowly work towards the ground until the wires are stuck on the ground plate by electric spark/shock.
5. Release the “weld” button and remove the work for examination.

The six thermocouples were tested for measurement uncertainty against a manufactured thermocouple supplied by Omega Engineering. All seven of the thermocouples were exposed to a copper plate heated by a hotplate to a temperature range of 23-100^{o}C. The temperature measurements for all seven thermocouples were recorded with a data acquisition system. A plot of the temperature measurement vs. input temperature for the thermocouples is provided in Figure 3.23. From Figure 3.23, all of the data points for the seven thermocouples appear to lie on top of each other. Table 3.6

provides a list of the uncertainties of the thermocouple measurements and the corresponding resolution of the linear fit.

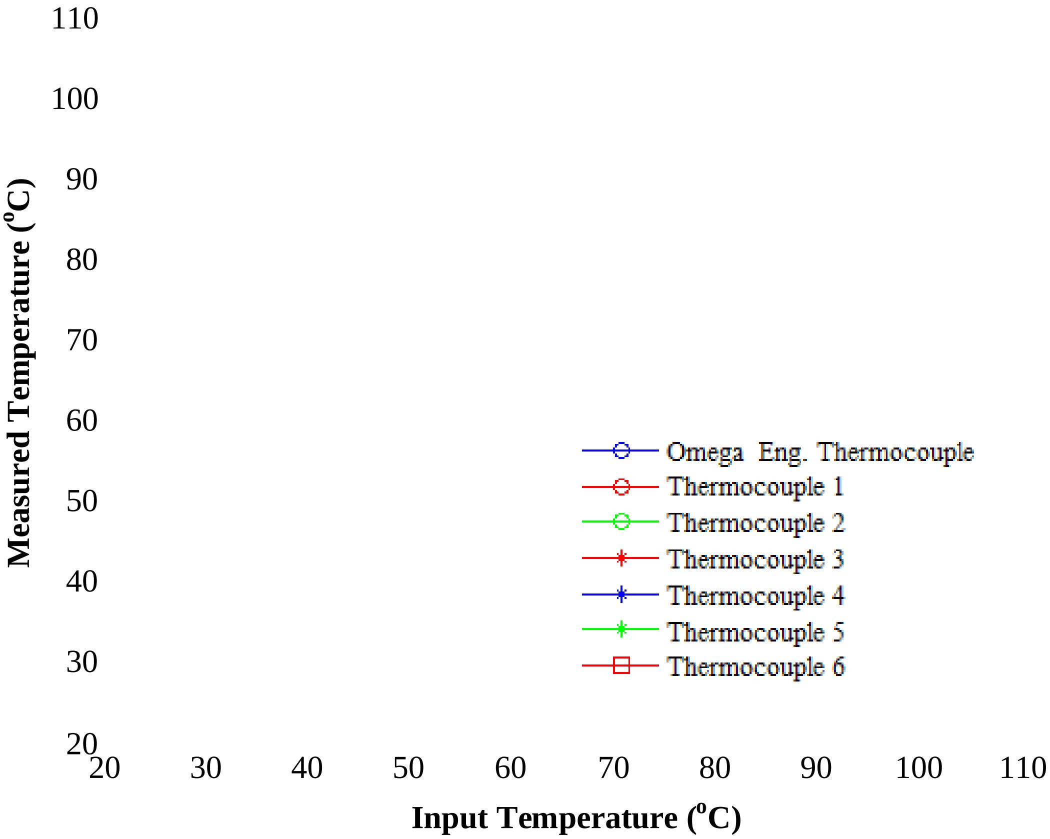

Figure 3.23: Calibration plot of measured temperature vs. input temperature for the TT-K-30 thermocouples.

From Table 3.6, the average measurement uncertainty of the thermocouple wires is approximately 0.738^{o}C. Five of the thermocouples were placed in the locations of the loop as specified in Figure 3.1. Thermowells were used to house the thermocouples at various locations of the loop.

Table 3.6: List of the thermocouple wire uncertainties.

Thermocouple	Total Measurement Uncertainty	Maximum Residual
1	0.760^{o}C	0.9998
2	0.738^{o}C	0.9998
3	0.742^{o}C	0.9998
4	0.723^{o}C	0.9998
5	0.729^{o}C	0.9998
6	0.734^{o}C	0.9998

A photograph of one of the thermowells that were used is provided in Figure 3.24. The remaining two thermocouples were used to monitor surface temperature of the heater and the ambient temperature of the heater chamber. The next section will discuss the pressure measuring devices used.

Figure 3.24: Photograph of one of the thermowells used in the present study.

3.11 Pressure Measuring Device Selection and Calibration

Three pressure transducers were considered for the present study and are presented in Figure 3.25. The three pressure transducers considered were unused pressure transducers which were purchased prior to the present study. Decision matrices were developed and used as a down selecting tool in the selection process to determine which pressure transducer was the most suitable choice for the present study. The most important requirements for selecting the pressure transducers for the present study were the operating specifications. The requirements for the pressure transducers were as follows:

1) The pressure transducer must be able to measure pressures within the heat transfer loop operating pressure range.
2) The pressure transducer must have a linear output voltage signal.
3) The output signal of the pressure transducer must be compatible with the data acquisition system.

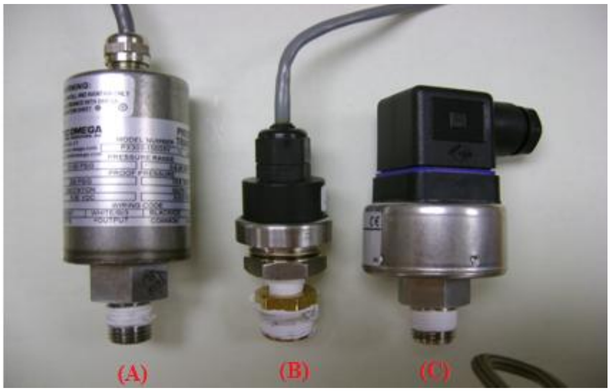

Figure 3.25: Photograph of the pressure transducers. (A) PX303-100GV, (B) PX480A-300GV, and (C) WIKA model ECO-1.

The following discussion presents an explanation on pressure transducer specifications and the pressure transducer selection process for the present study. Three pressure specifications typically appear on the specification sheet of a pressure transducer. The pressure range is the normal operating region in which the data sheet specifications are applicable. The burst pressure is the maximum pressure at which the pressure transducer may be exposed for two minutes without rupture and results in component separation or application fluid leakage. The burst pressure is specified as a multiple of the upper limit of the pressure transducer's operating range. The proof pressure is the maximum pressure at which a pressure transducer may be exposed after which it will return to its normal operating pressure range and perform within specification. Similar to burst pressure, the proof pressure is specified as a multiple of the upper limit of the pressure transducer's operating range (e.g., 1.5X for a 0-0.689 MPa (0-100 psi) pressure transducer would mean a proof pressure of 1.03 MPa (150 psi)). It is not definite that the pressure transducer will function within specification when returned to its normal operating range after being exposed to a pressure above its proof pressure. Choosing a pressure transducer should be based on the output signal, application pressure range, device pressure range, proof pressure, burst pressure, and device accuracy.

The highest accuracy is attained only when the normal operating pressure of the pressure transducer is matched to the application. In order to understand the effect of using a pressure transducer to measure pressures which are in a smaller range than the devices full scale reading, it is useful to look at an example. Assume there is a requirement to measure pressures in the range 0-0.345 MPa (0-50 psi) and a 0-0.689 MPa

(0-100 psi) pressure transducer has been selected. The device accuracy (static error and total error bands) is specified as a percentage of full scale reading (F.S.) and, in this example, is ±0.75% (F.S.). If the full scale of the application is only 0-0.345 MPa (0-50 psi), the accuracy would be represented as a percentage of the application's full scale and would be (0.689 MPa/0.345 MPa)*±0.75% (F.S.) = ±1.5% (F.S.). In general, the accuracy in a measuring instrument application is given by:

$$A_{app} = A_{dev} \cdot \frac{F.S._{dev}}{F.S._{app}} \tag{3.8}$$

where:

A_{pp} = application accuracy
A_{dev} = device accuracy
$F.S._{dev}$ = device full scale reading
$F.S._{app}$ = application full scale reading

The maximum pressure limit of the heat transfer loop was determined by the rotary pump pressure specification. The rotary pump used in the present study has a pressure operation limit of 0.26 MPa (40 psi). The maximum operating pressure of the pump was not expected to be met in the present study. As a result, a high accuracy pressure transducer was needed that could measure small pressure changes. However, a transducer that was capable of measuring pressures above the application range, and could still measure small pressure changes was sufficient. For example, a transducer that has a pressure range of 0-0.207 MPa (0-300 psi), and has an accuracy of 0.25% (F.S.) can measure pressure differences as small as 0.0052 MPa (0.75 psi). However, one would still need to take into account the application accuracy.

When considering the application accuracy and utilizing Eqn. 3.8 the application accuracy is found to be 0.0052 MPa (0.75 psi). A safety margin of 0.345 MPa (50 psi) was added on for cases in which pressure build up may occur in sections of the loop where valves are used to control the flow. As a result, a pressure transducer that has at least a maximum pressure limit of 0.76 MPa (100 psi) had to be considered during the selection process. However, the theoretical accuracy of the application and pressure transducer range accuracy had to show good agreement for the final selection. Table 3.7 lists the application and device accuracy for the three pressure transducers considered. Table 3.8 presents the decision matrix that was developed and used to select the pressure transducer used.

Table 3.7: Pressure transducer device and application accuracy results.

Range	Model Number	Device Accuracy	App. Accuracy
0-0.69 MPa	PX303-100GV	0.25% (F.S.)	0.25% (F.S.)
0-2.07 MPa	PX480A-300GV	0.30% (F.S.)	0.90% (F.S.)
0-3.45 MPa	WIKA Model ECO-1	0.50% (F.S.)	2.50% (F.S.)

From the decision matrix listed in Table 3.8, the PX303-100GV pressure transducer deemed to be the most suitable pressure transducer for the present study when considering the alternative choices. The application accuracy of the PX303-100GV pressure transducer is 0.25% (F.S.) which means that the device and application is matched to measuring pressure changes in a range of 0.0017 MPa (0.25 psi) in a full span application range of 0-0.689 MPa (0-100 psi). All three of the pressure transducers were calibrated for the present study. The calibration data is presented. The next section will discuss the pressure transducer calibration procedures developed and used.

Table 3.8: Decision matrix for selecting the flow metering device type.

Criteria	**Weight, W%**	**Pressure Transducers Models**		
		(1)	**(2)**	**(3)**
Accuracy	35	40 **45**	10 **45**	5 **45**
Functionality	25	35 **35**	15 **35**	5 **35**
Ease of Use/ Stability	15	20 **20**	20 **20**	20 **20**
Total	**100**	95 **100**	45 **100**	30 **100**
Selection Models: (1) PX303-100GV model pressure transducer, (2) PX480A-300GV model pressure transducer, and (3) WIKA ECO-1 model pressure transducer.				

Calibration of a pressure transducer is a direct comparison between indications of the transducer and the indications of the standards. For pressure transducer calibration two standards are used; one for the input and another for the output signal. The standards for the input are pressure standards. The calibration technique that was developed and used in the present study consisted of a dead weight tester for the pressure input and a data acquisition system for recording the output voltage signal. The dead weight tester used to calibrate the pressure transducers in this investigation consisted of a precision machined piston and cylinder, in which weights were added to provide a number of predetermined pressures within the cylinder. The cylinder was screwed on to a base plate supported by leveling screws and the base plate fitted with a bull's eye level as shown in the schematic provided in Figure 3.26a. The weights supplied were 227.3 kg (2.23 N) weights, and the piston weight 0.5 kg (2.0 N).

As shown in Figure 3.26, a gauge is linked to the cylinder, by a flexible tube and leakage past the piston is taken to drain, which is drilled opposite to an annular recess at the top of the cylinder. For the pressure transducer calibration tests the transducer was mounted where the dial pressure gauge is shown in Figure 3.26a. The pressure generated by the piston and weights is equal to the force exerted on the cylinder divided by the piston area. The area is obtained by:

$$A_{piston} = \frac{\pi d_{piston}{}^{2}}{4} \tag{3.9}$$

where: A, is the piston cross section area = 0.00025 m^2 (2.5 cm^2).

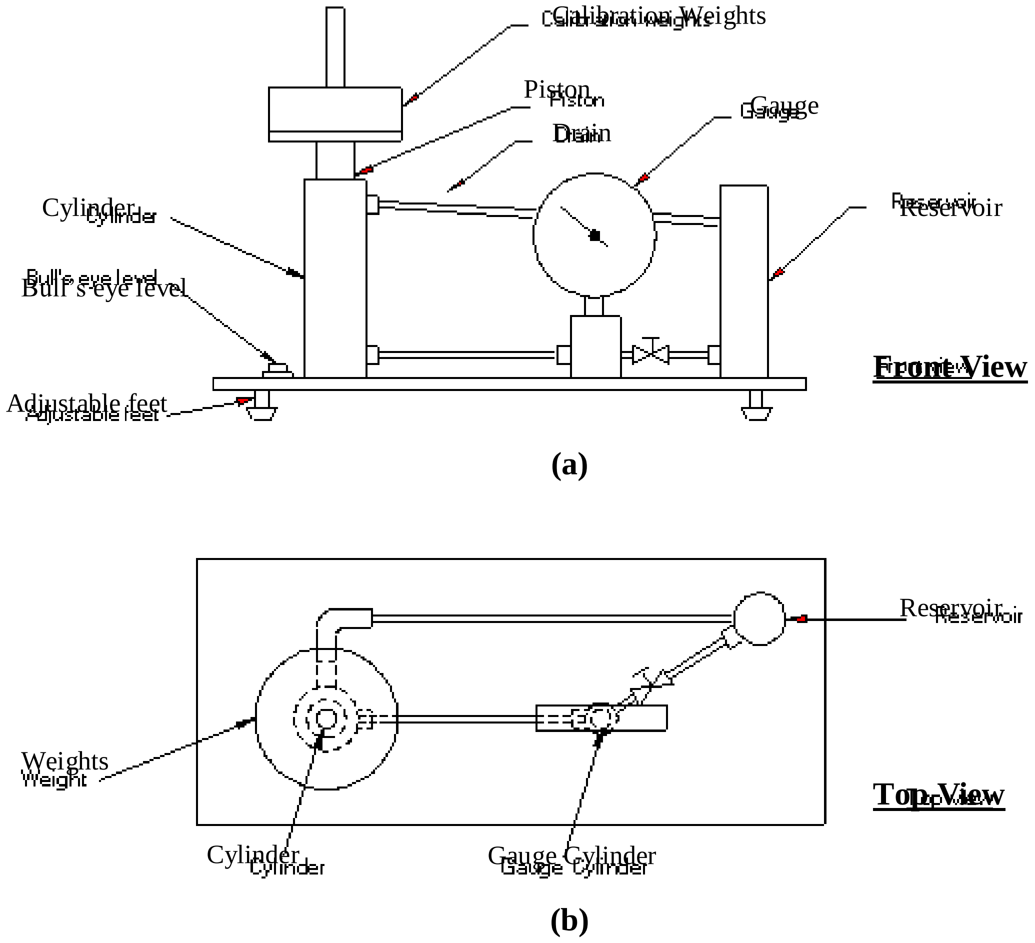

Figure 3.26: Schematic of the dead weight tester apparatus: (a) Front view, (b) Top view.

$$P = \frac{F}{A_{cylinder}} \tag{3.10}$$

where: P is the pressure in N/m^2

This pressure P is transmitted to the transducer and a comparison between input pressure and voltage was made. In order to obtain good calibration results, precautions had to be taken into account. The transducer was first cleaned, and then the dead weight tester and transducer had to be maintained at least six hours before the start of the calibration in order to reach thermal equilibrium. During the calibrating of the pressure transducers, it was necessary to ensure that no vibrations, shocks, or electromagnetic radiation were in vicinity of the transducers.

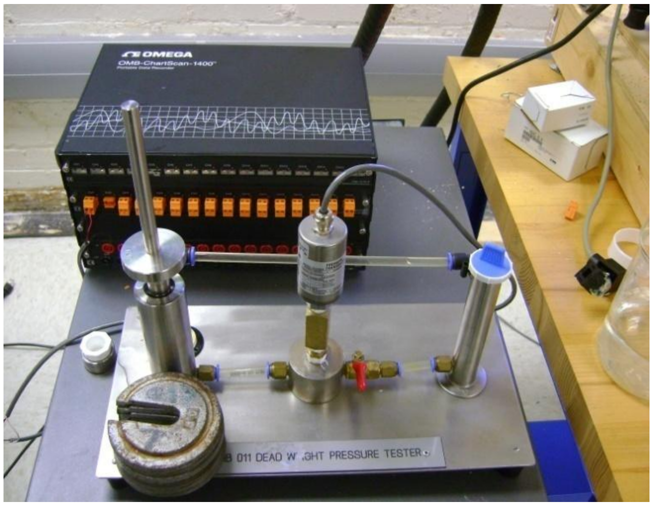

Figure 3.27: Photograph of the pressure transducer calibration setup used in the present study.

The procedure for calibrating the pressure transducers were as follows:

1. Place the pressure transducer on the tester and ensure that the connection is tight.
2. Remove the piston and fill the cylinder and the reservoir with the clean (preferably distilled) water to half full and take the “zero” gauge reading.
3. Insert the piston into the cylinder and open the ball valve to allow air bubbles to move into the reservoir. Adjust the piston so that the wing is about 0.025 m (25 mm) above the cylinder then close the ball valve.

4. Spin the piston to minimize friction effect and take the gauge reading due to piston weight.
5. Add additional weight on the piston and record reading until all weights are used or maximum gauge reading is reached.
6. If the piston wing is too low i.e. less than 0.015 m (15 mm) above the cylinder, repeat (3).
7. Remove the weight and record pressure for every weight.
8. Record the voltage output using the data acquisition system. Plot a calibration graph of pressure vs. voltage.

The PX303-100 GV model pressure transducer was the first transducer that was calibrated. The output voltage signal was recorded as weights were added. The calibration plot of pressure vs. voltage for the PX303-100-GV pressure transducer is presented in Figure 3.28. A least squares fit was performed and the calibration equation was obtained. The calibration equation is also presented in Figure 3.28.

The manufacturer stated accuracy of the PX303-100GV model is 0.00172 MPa (0.25 psi) and the uncertainty from the measurements was found to be ±0.00019 MPa (0.027 psi). The residual from the calibration plot is 0.999. The maximum error in the simplistic fit is 0.02913 MPa. The second pressure transducer calibrated was the PX480A-300GV model. The plot of pressure vs. voltage and the calibration equation obtained from the least squares fit for the PX480A-300GV pressure transducer is presented in Figure 3.29.

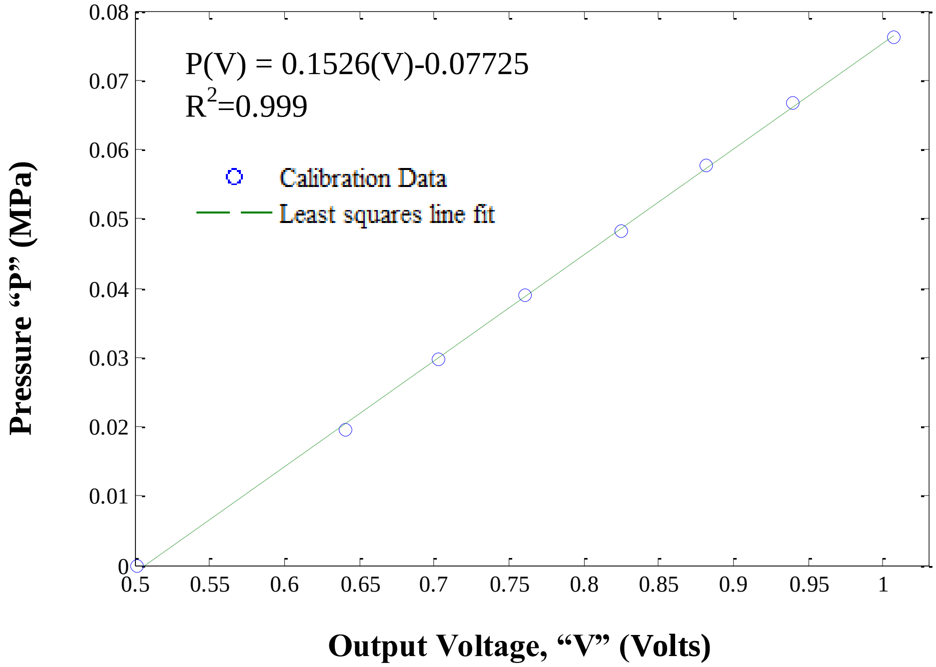

Figure 3.28: Calibration plot of the Omega Engineering model PX303-100GV (0–0.689 MPa range pressure transducer) calibrated and used for the present study.

The manufacturer stated accuracy of the PX480A-300GV model is 0.0062 MPa, (0.9 psi) and the uncertainty from the measurements was found to be ±0.0026 MPa (0.377 psi). The residual from the calibration plot is 0.998. The maximum error in the simplistic fit is 0.0735 MPa. The last pressure transducer calibrated was the Wiki model ECO-1. The plot of pressure vs. voltage and calibration equation for the Wiki model ECO-1 pressure transducer is presented in Figure 3.30.

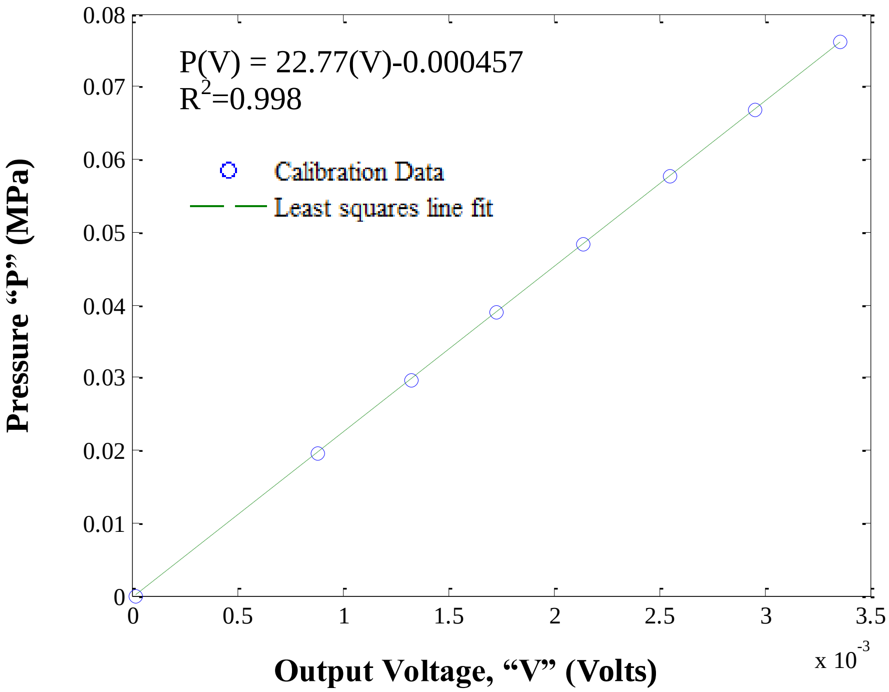

Figure 3.29: Calibration plot of the Omega Engineering PX480A-300GV (0–2.07 MPa range pressure transducer) calibrated for the present study.

The manufacturer stated accuracy of the WIKA model ECO-1 is 0.017 MPa (2.5 psi), and the uncertainty from the measurements was found to be ±0.0034 MPa (0.493 psi). The residual from the calibration plot is 0.999. The maximum error in the simplistic fit is 0.076 MPa. After data reduction and analysis was performed to obtain the uncertainties and residuals, additional test runs were performed implementing the calibration regression equations obtained from the calibration plots into the data acquisition collection software program to insure the repeatability. The generated pressures from the weights and the response from the data acquisition proved to be in good agreement for each pressure transducer. The next section presents a discussion on the process developed for designing the void fraction sensor used in the present study.

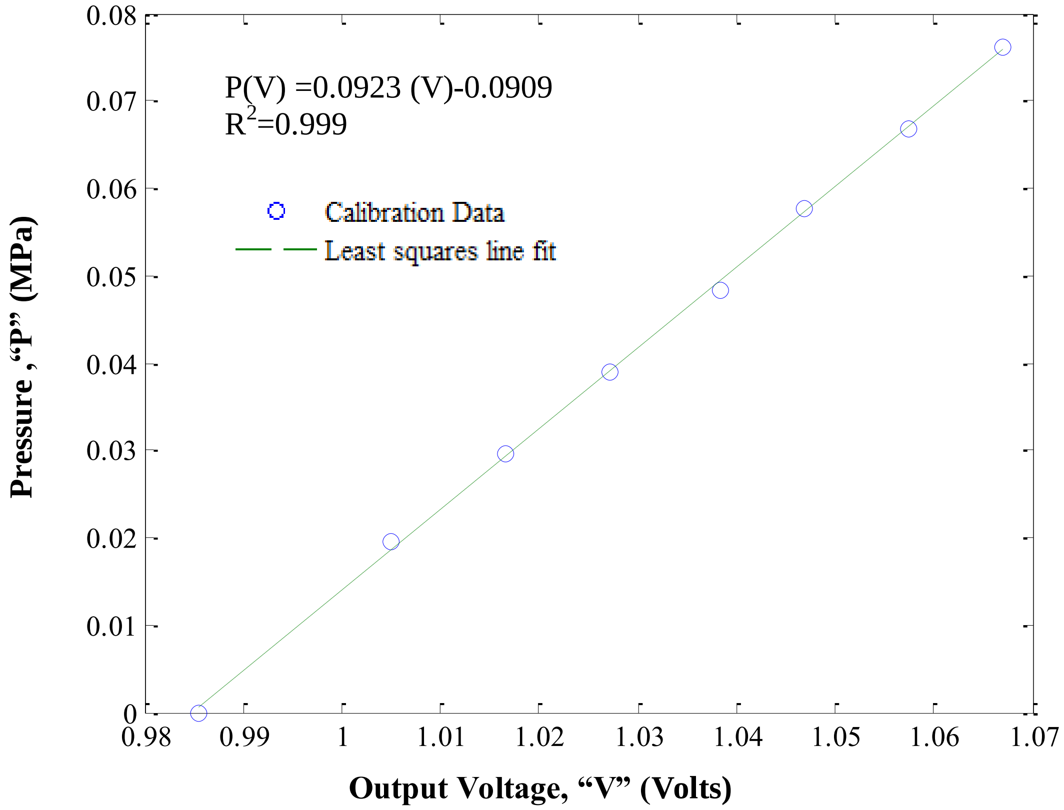

Figure 3.30: Calibration plot of the WIKA ECO-1 model (0–3.45 MPa range pressure transducer) calibrated for the present study.

3.12 Void Fraction Sensor Design Process

For the design of the void fraction sensor used in the present study, a decision matrix was generated for selecting the most suitable technique of measuring void fraction. The decision matrix is provided below in Table 3.9. Three main factors were considered for down selecting the most suitable technique of measuring void fraction. These factors were: functionality, size, cost, and ease of use/stability. The review of literature of void fraction measuring techniques presented in Chapter 2 was helpful in the decision making process. From Table 3.9 capacitance measuring techniques was deemed be the cheapest and simplest technique of measuring void fraction.

Table 3.9: Decision matrix for selecting the method of measuring void fraction.

Criteria	**Weight, W%**	**Void Fraction Measuring Techniques**			
		(1)	**(2)**	**(3)**	**(4)**
Accuracy	**35**	10 **35**	5 **35**	10 **35**	13 **35**
Functionality	**25**	9 **25**	6 **25**	5 **25**	13 **25**
Cost	**25**	20 **25**	5 **25**	5 **25**	15 **25**
Ease of Use/ Stability	**15**	15 **15**	5 **15**	5 **15**	17 **15**
Total	**100**	54 **100**	21 **100**	25 **100**	58 **100**
Selection Models: (1) QCV, (2) Radiation Attenuation, (3) Conductance probes, and (3) Capacitance methods.					

When considering the alternatives, QCVs provide an accurate void fraction measurement by “visual observation” and are useful for calibrating void fraction sensors or comparing QCV void fraction readings against sensor output voltage signals. Also, QCV methods are not a sensible means to measure void fraction for continuous flows. Radiation attenuation methods require a priori knowledge of the flow regime and require complex signal analysis. When considering size and ease of use for radiation attenuation methods, the design of the sensor must incorporate an external wall or channel boundary electrode design for high sensitivity sensor-induced flow disturbances. In a more general sense, the channel boundary design requires that the channel and the electrode be unified. A major drawback in conductance probes is the effect of flow pattern identification based on the relationship between the sensor signal and void fraction. Another disadvantage is electrolysis which introduces hydrogen to the flow stream by a chemical reaction due to the induced current flow. For these reasons, a capacitance void fraction sensor was developed and used to measure void fraction in the loop for the present study.

3.12.1 Void Fraction Sensor Design Requirements

In the process of designing a capacitive void fraction sensor for obtaining void fraction measurements in a circular tube, the distance between the probe and the ground-reference target (ground electrode) depends on the tube or pipe diameter and may not be small in comparison with the electrode dimensions. This is so that the sensor may have the best measurement sensitivity. The capacitive method for measuring bubble concentration is based on the change in dielectric in the presence of bubbles within the sensing area. For example, in a liquid/gas flow, because bubbles have a lower dielectric constant than the liquid, the measured capacitance increases with the diameter of the bubble. A linear expression for the change in voltage in relation to a change in void fraction of a two-phase flow is assumed. The following section presents the design requirements for the void fraction sensor developed for the present study.

The void fraction sensor was required to be:

1. Non-intrusive and introduce no flow disturbance.
2. Functional with Water and Novec 7000 as the working fluid.
3. Highly sensitive for a continuous flow field.
4. Insensitive to vibrations, and be able to withstand loop operating pressure ranges of 0-0.689 MPa (0-100 psi).

Several designs of void fraction sensor electrode and conduit configurations were considered for the present study. These designs consisted of a circular fluid-flow cross-section, a rectangular fluid-flow cross-section, and multiple sensor electrode configurations. These designs are presented in Appendix E. A discussion on the first and final design of the void fraction sensor is presented respectively. These two designs are referred to as design A and B respectively. A CAD drawing of design A is presented in Figure 3.31.

The void fraction sensor developed for the present study is a capacitance measuring device. That is, the sensor measures the capacitance of the mixture by its dielectric constant. The dielectric constant is a dimensionless quantity. The dielectric constant of air is approximately 1. Similarly, the dielectric constant of the vapor phase of any dielectric substance is taken to be 1 (Pitzer, 1983; Fernandez, et al., 1995). However, the dielectric constant of the liquid state of any dielectric fluid varies. Therefore, void fraction can be used to infer a quality measurement by capacitive techniques.

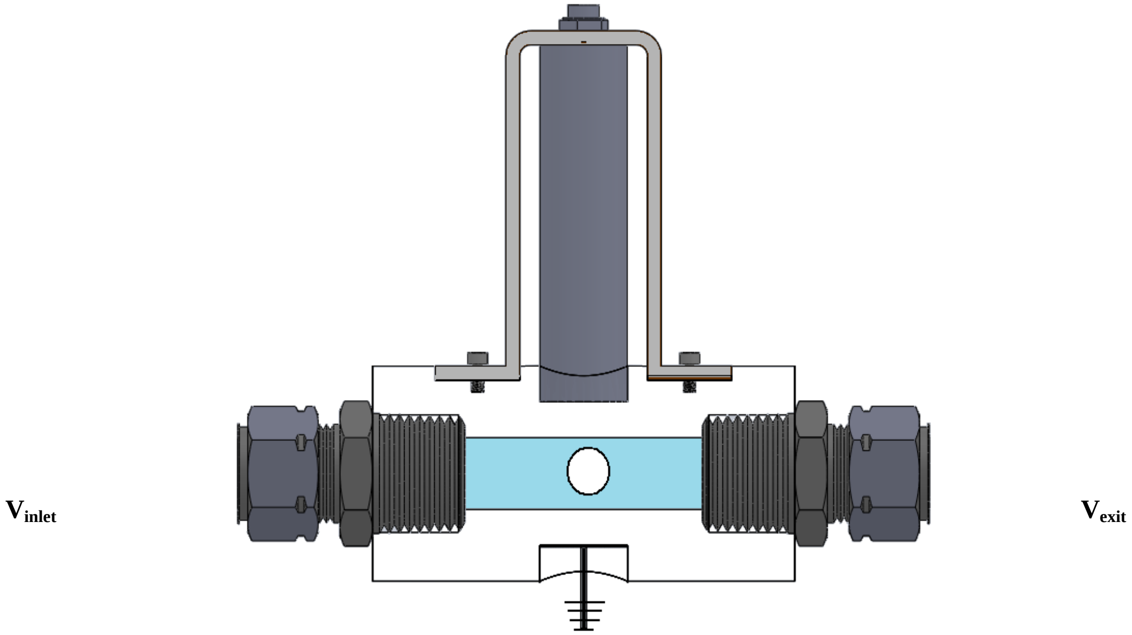

Figure 3.31: CAD Drawing of void fraction sensor Design A. The electric field lines are represented by arrows and the flow field is directed from left to right as shown by the velocity inlet and exit arrows. The round circle in the middle represents the passing of an air bubble.

For the present study, the change of voltage in the electrostatic field produced in the dielectric environment was sensed by a sensing probe and a high resolution impedance amplifier (MTI Accumeasure 500 system). A high frequency excitation waveform was used. Design A consisted of a cylindrical capacitance probe with a 6.25 mm (0.246 in) diameter, 0.254 mm (0.01 in) thick copper plate which served as the ground-reference target. The cylindrical capacitance probe and ground-referenced target is similar to a parallel plate capacitor setup. A side view of the sensor is presented in Figure 3.31. A cylindrical well was cut in place for the probe to be mounted. The probe was secured by a metal u-shaped clamp, which was screwed to the body of the sensor. The polycarbonate material between the electrodes serves as a transparent shield to afford a non-contact relationship between the probe face and the flow field. A photograph of design A is presented in Figure 3.32.

Figure 3.32: Photograph of void fraction sensor Design A used in the present study.

Several problems were observed from Design A. First, the probe was unable to sense the presence of liquid without the ground-reference target being in contact with the liquid. Also, since the ground-referenced target had to be in contact with the liquid, there was no way of mounting the circular ground plate inside the flow conduit without the fluid flow moving it. A modified ground-reference target was needed that could remain stationary and be capable of sensing the presence of the liquid. Design B consisted of the same probe setup, except the ground-referenced target geometry was modified for measurement sensitivity as shown in Figure 3.33. The ground-reference target consisted of a 0.0127 m (0.5 in) diameter copper pipe with a half cylinder opening in the middle for the probe sensing. The next section presents a discussion on the sensitivity and calibration procedures for the void fraction sensor.

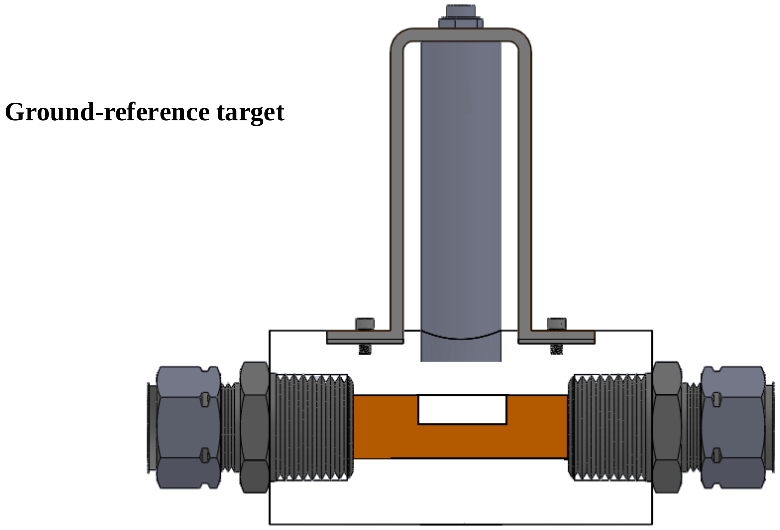

Figure 3.33: CAD drawing of void fraction sensor Design B.

3.12.2 Void Fraction Sensor Sensitivity

In the process of validating the sensitivity of the void fraction sensor design developed and used for the present study, basic equations which describe capacitance and impedance in a parallel plate capacitor were solved where possible. These solutions, which depend on the ratio of fluid to air as well as sensor geometry and dielectric properties of the fluid and air, provided independent predictions of the relationship between void fraction and sensor output voltage signals. Several studies have utilized Possion’s Equation and the Laplace Equation to study the electric field potential of a capacitive void fraction sensor. However, to perform such a study requires knowledge of the surface charge density of the dielectric material. The surface charge density is not a material property, but a measured quantity that may or may not in some instances be uniform throughout the dielectric material. A discussion on surface charge density can be found in (Mankin & Callan, 1977; Reedyk & Perlman, 1968; Johann & Soergel, 2009). The present study was focused on the basic equations which describe the change in output voltage as a result of the change in air and liquid levels. The changes in air and liquid levels were converted to a volume averaged void fraction measurement that was compared to the change in output voltage.

The capacitance measuring device that was used in the present study was an MTI Accumeasure 500 measuring system. The Accumeasure 500 system measures the electrical impedance of the capacitance between a sensing probe and a ground-referenced target. The magnitude of the impedance is proportional to the reciprocal of the capacitance value as defined by the relationship:

$$Z_c = \frac{1}{\varpi C} \tag{3.11}$$

where ω is proportional to the frequency at which the capacitance measurement is being measured. Substituting the equation for capacitance into the impedance equation shows that the impedance is directly proportional to the gap value, as shown in the following equation:

$$Z_c = \frac{d}{\omega \kappa A_p} \quad \textbf{(3.12)}$$

The Accumeasure probe amplifier produces a DC voltage that is linearly proportional to the average value of the probe gap impedance, and an AC voltage variation from the DC voltage that is directly proportional to the amplitude of the target vibration. The amplifier electronic circuitry eliminates the effects of both the probe cable capacitance and the stray capacitance at the edge of the probe sensing area that could cause non-linearity of the gap and vibration measurements. A plot of the manufacturer calibration data is provided in Figure 3.34. The plot indicates that the trend of the calibration data is linear. This is because the only change that results in a change in output voltage is a change in distance of the sensing probe and ground–reference target.

The manufacturer reported that the uncertainty in the measurements was 0.07%. All measurements relating to the calibration report were certified traceable to the United States National Institute of Standards and Technology and provide a measurement uncertainty of less than one-fourth of the specification of the unit under test. From the obtained calibration results, one can see that the plot indicates a sensitivity of 2.7 mV/µm. The uncertainty measurements in the probe reported by the manufacturer were taken to have the same value for the calibration of the void fraction sensor. The capacitance probe used in the present study is capable of measuring capacitance with air between the probe face and ground-reference target at a maximum distance of 3.8 mm (0.15 in). This can be verified from the plot presented earlier in Figure 3.34.

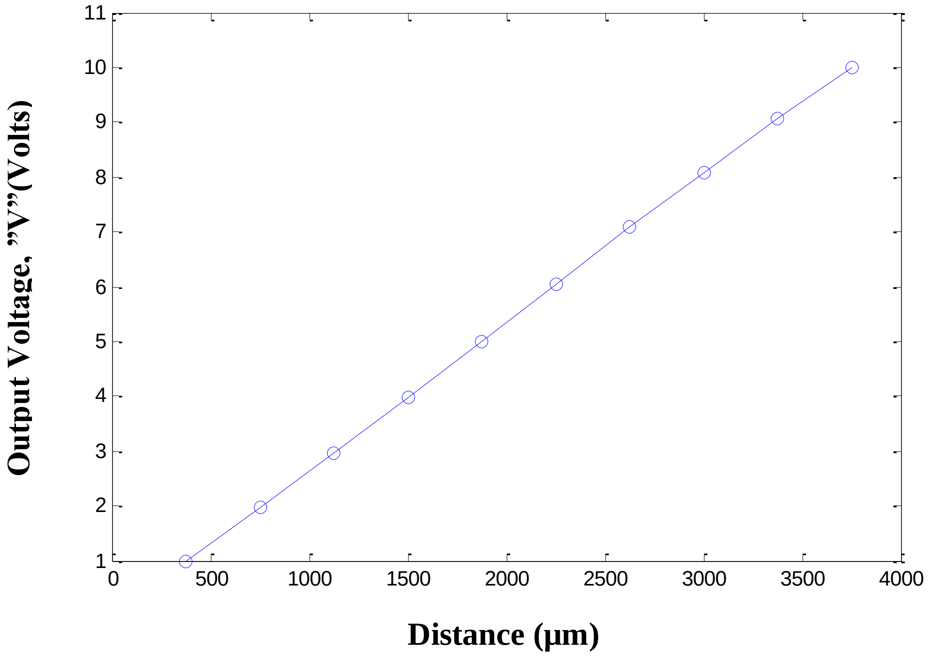

Figure 3.34: Manufacturer calibration plot for the capacitance probe and amplifier.

This means that the amplification of the measurement system is of the order 3X. The amplifier range is sensitive by the dielectric constant of the material between the probe face and the grounded target. The manufacturer calibration results were based on air as the dielectric material. The dielectric constant of air is 1, and the standard measurement range of a standard probe provided by MTI Inc, is 1.8 mm (0.071 in). For example, the dielectric constant of water is 80. As a result the measurement range of the probe with water as the dielectric would be 3.8 mm*80=304 mm (11.97 in).

Figure 3.35 presents a schematic of the static calibration setup of the void fraction sensor used in the present study. As shown Figure 3.35, the dashed lines represent the control volume where the liquid levels are changed to produce a local void fraction measurement. The liquid height is increased while the air gap is decreased and a change in the output voltage signal will occur. A Matlab script file was produced to model this effect and provide a prediction of the voltage output for the range of void fractions. This was done in order to obtain a priori knowledge of the sensor's output voltage behavior for a liquid level increase.

As shown in Figure 3.35, from the sensor face to the grounded plate, three different dielectric materials are present. These materials are: the polycarbonate material separating the sensor face, the fluid, and air. Since there are three materials between the two plates, two of which are changing as a function of height, the equivalent capacitance would be a summation of the individual capacitance values of the: the polycarbonate material, the working fluid, and air. Figure 3.36 provides the equivalent circuit diagram describing the individual capacitors in series. The equation used to model this effect is described as:

$$\frac{1}{C} = \frac{1}{C_p} + \frac{1}{C_a} + \frac{1}{C_f} \tag{3.13}$$

The three materials separating the plates are treated as individual capacitors in a circuit. All three of these capacitors are treated as capacitor in series. Eqn. 3.13 was used in the Matlab script to model the predicted output voltage signal as a function of liquid level increase.

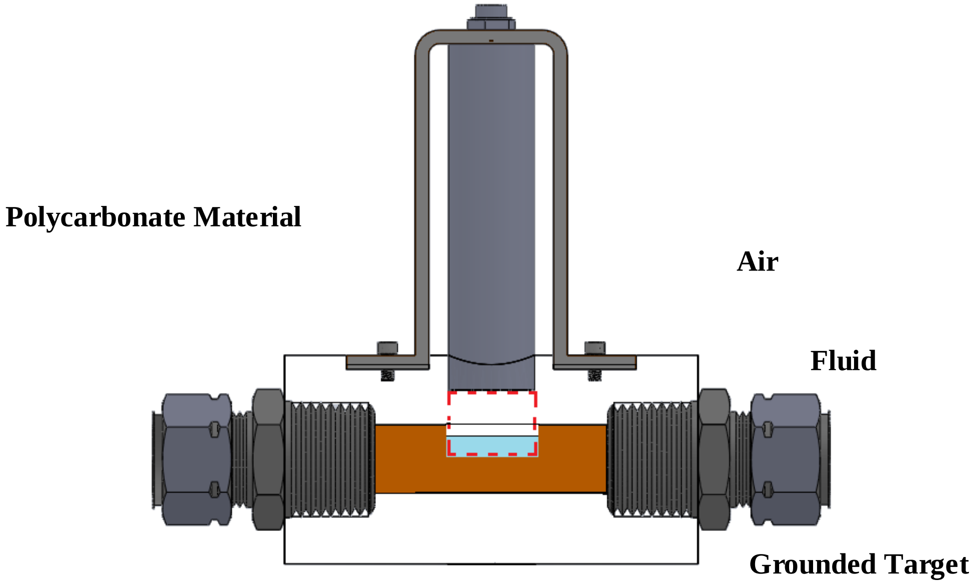

Figure 3.35: Schematic of the void fraction sensor calibration setup.

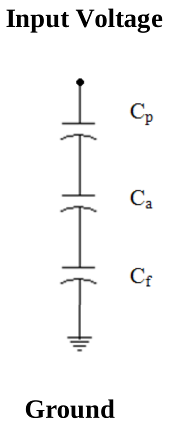

Figure 3.36: Schematic of the equivalent circuit diagram used in the present study that relates the fluid to air ratio (void fraction) to individual capacitors.

A plot of output voltage vs. void fraction was generated as prediction of the sensitivity of the void fraction sensor. The plot of the predicted output voltage vs. void fraction is presented in Figure 3.37. The input voltage for the capacitance measuring transducer is 12 V. From Figure 3.37, void fraction measurements ranging from 0 to 1 result in a voltage output from 6.75 to 9.55 V. The plot in Figure 3.37 has a linear trend, and is generated excluding any kind of fringing, stray capacitance or other effects that may be present in the system. Variables such as frequency, current, and resistance are held constant. The only change that takes place is impedance due to a change in measured capacitance. From the obtained results, one can expect at least a 9.55 V output for pure air, and a 6.7 V output for pure fluid.

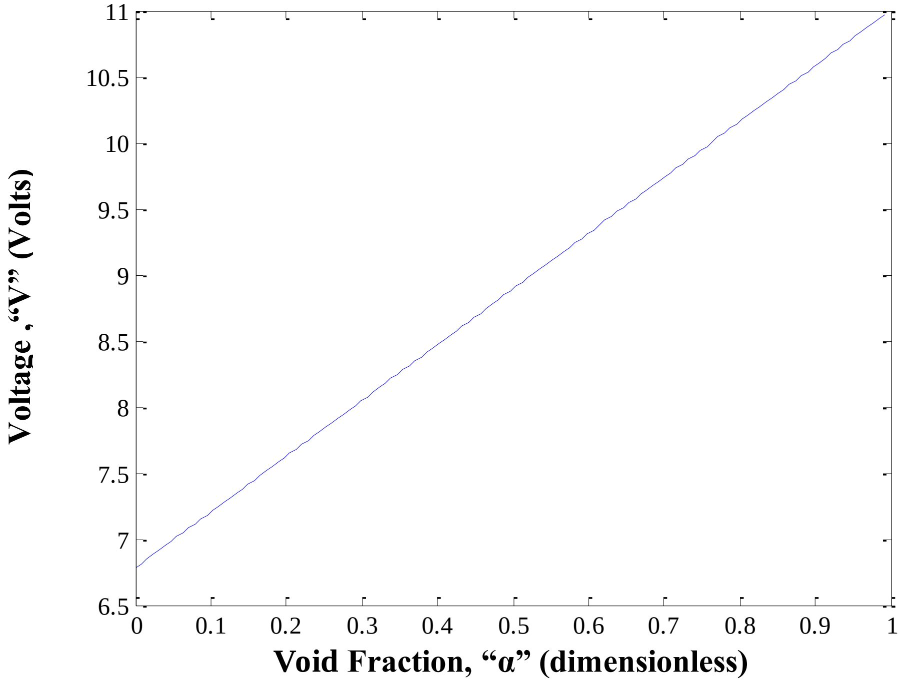

Figure 3.37: Plot of the predicted output voltage vs. void fraction values.

3.12.3 Void Fraction Sensor Calibration

Calibration of a capacitive void fraction sensor may be done statically or dynamically. When a static calibration is done, liquid is incrementally added as the output voltage is recorded. Dynamic tests involve comparing sensor output voltage signals to visual readings with the use of a high speed camera. Another approach is to use beads or phantom acrylic rods to simulate air with water surrounding the beads or rods. This approach is used in the calibration of bubby and annular flows.

A number of tests with the capacitive void fraction sensor used in the present study were done which involved static calibrations. Figure 3.38 provides the calibration plot of the full range of void fraction vs. output voltage values for the static calibration test. The results shown in Figure 3.38 are for the sensor oriented in a horizontally. From Figure 3.38, the sensor output signal is nonlinear for the full range of void fraction measurements with water and Novec 7000 as the working fluid. This is partially attributed to the electrode configuration, dielectric properties, degradation of the fluid, and the molecular geometry of both fluids.

Due to the surface tension of water, it was impossible to maintain uniform dispersion of water along the total length of the ground-referenced target at higher void fractions for water as the working fluid. From the obtained results in Figure 3.38, the experimental calibration results and predicted void fraction calibrations results for a zero void fraction measurement were proven to be within 10% difference.

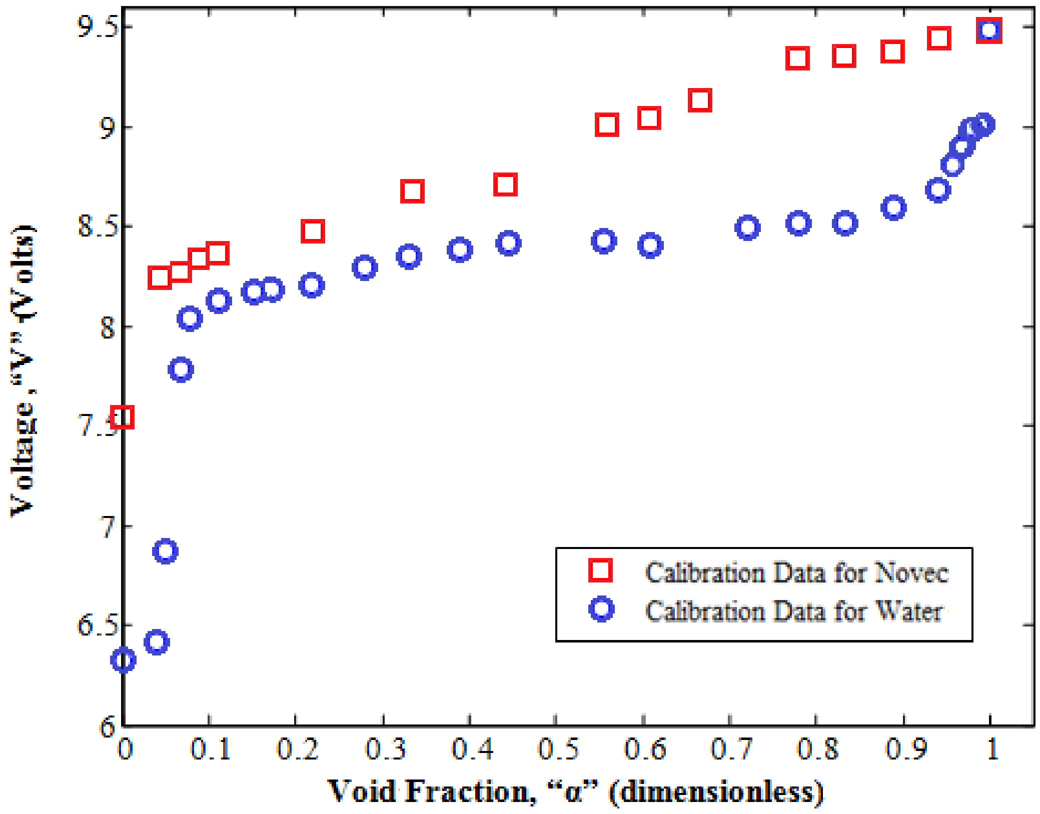

Figure 3.38: Calibration plot for the full range of void fraction measurements for Water and Novec 7000.

For pure air, the experimental and predicted values are approximately the same. A regression analysis was done to obtain an expression for void as a function of output voltage for both Water and Novec 7000 static calibration data. From the results shown in Figure 3.39 and Figure 3.40, the data range of void fraction vs. output voltage data is nonlinear. A series of regression fits were applied to the data and a third order polynomial fit proved to be the best fit for Novec 7000. The corresponding residual fit for both Water and Novec 7000 was 0.972 and 0.993.

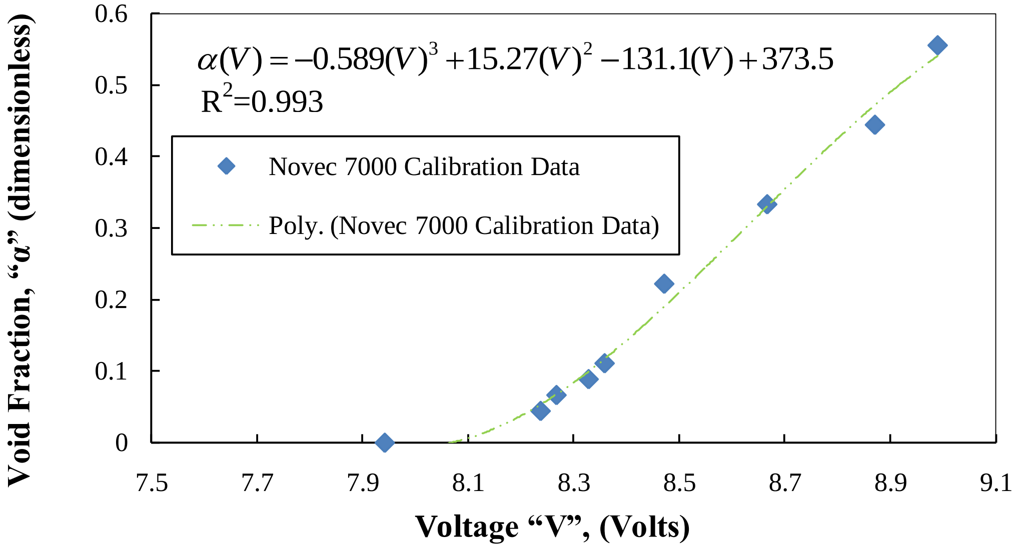

Figure 3.39: **Polynomial regression analysis for Novec 7000 void fraction calibration data.**

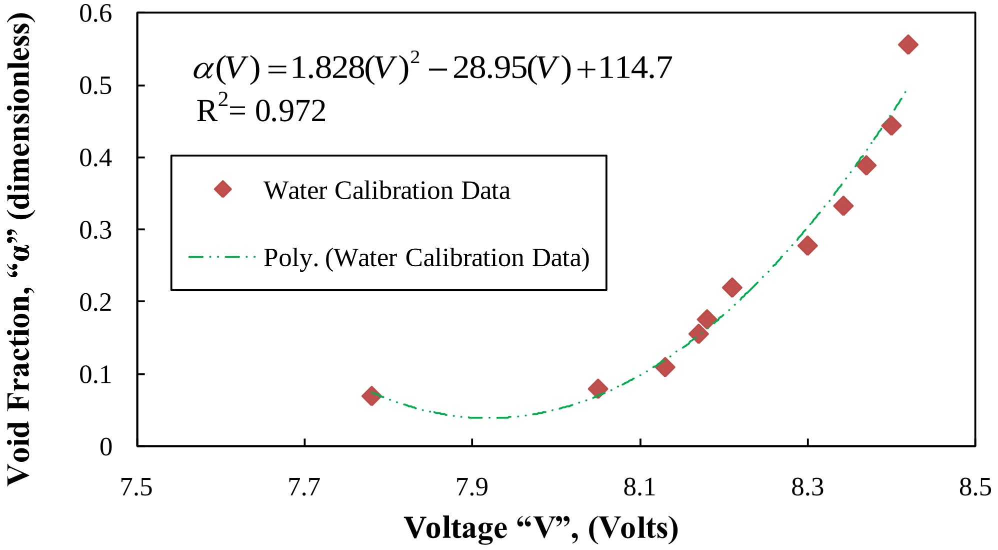

Figure 3.40: **Polynomial regression analysis for water-void fraction calibration data.**

A photograph of the finalized heat transfer loop with all the measuring instruments installed and instrumented is present in Figure 3.41. Chapter 4 presents a discussion on the results of the measuring instruments during loop performance for the present study.

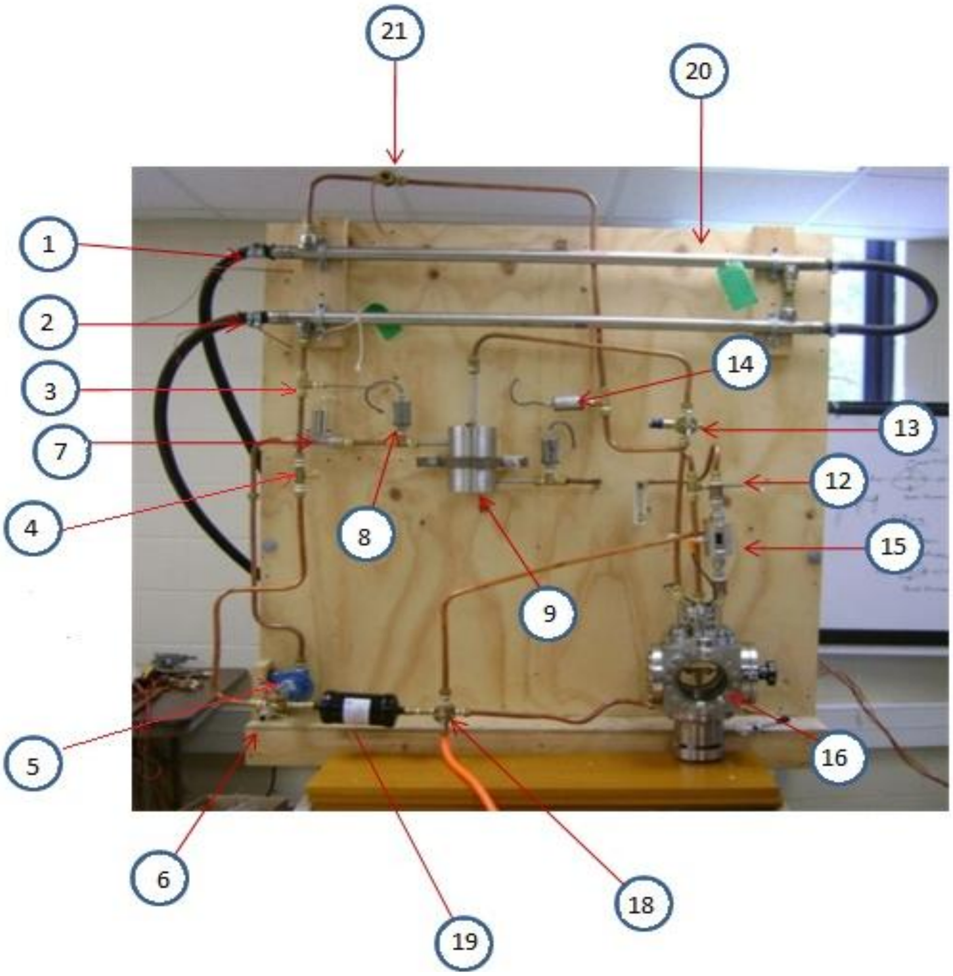

Figure 3.41: Photograph of the finalized heat transfer loop in the present study with all the measuring tools installed and instrumented. (1, 2, 3, 12, and 21) are the thermocouples, (5) is the rotary pump, (7) is the void fraction sensor, (8,10, and 14) are pressure transducers, (4, 6, 11, 13, and 18) are control valves, (15) is the flow meter, (16) is the high heat flux heater chamber, (19) is one of the two liquid storage tanks, and (20) is the heat exchanger used.

CHAPTER 4

RESULTS AND DISCUSSION

In Chapter 4 the performance results of the measuring tools used in the thermal loop are presented and discussed. Two dynamic loop test runs were performed to test the performance of the instruments. Measurement performance and data analysis for each instrument is presented accordingly. The performance of the high heat flux heater is also discussed. The next section will discuss the flow meter performance.

4.1 Flow Meter Performance

The flow meter was used to measure volumetric liquid flow rate for the two loop test runs. A photograph of the flow meter installed in the loop is presented in Figure 4.1. When the loop was not running the flow meter appeared to have a fluctuating voltage output signal and LED display reading. The LED screen displayed a fluctuating voltage signal between a negative flow rate reading and zero flow rate reading. However, during transient and steady state loop runs the flow meter was observed to have a constant output voltage signal and positive flow rate reading. The flow meter was operated at its minimum flow setting for the first test and the maximum flow setting for the second test. The minimum and maximum flow rate for the flow meter is 0.15 and 25 l/min. Figure 4.2 and Figure 4.5 presents a plot of the flow meter output voltage signal for both the minimum and maximum flow rate.

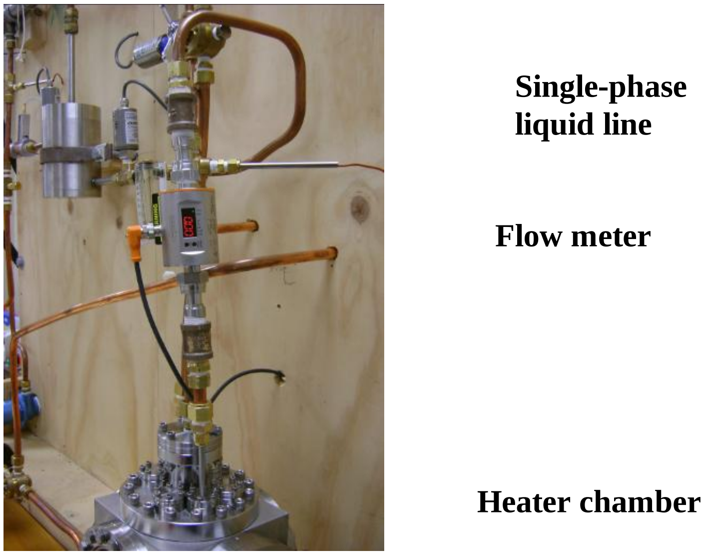

Figure 4.1: Photograph of the flow meter mounted on the liquid pipeline of the heat transfer spray cooling loop developed and used in the present study.

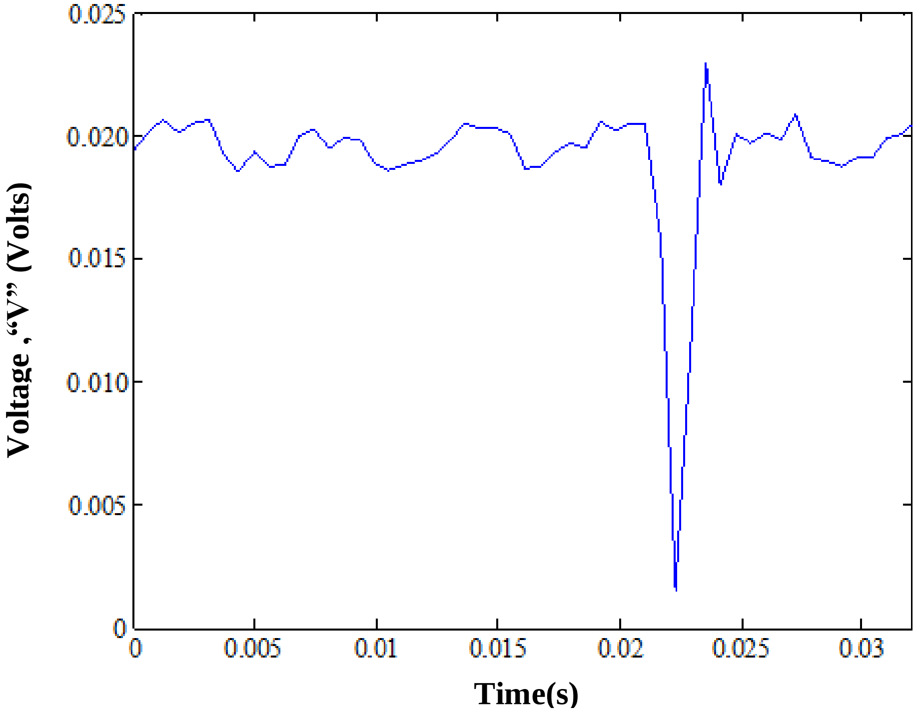

Figure 4.2: Plot of the flow meter output voltage signal vs. time at 0.15 l/min.

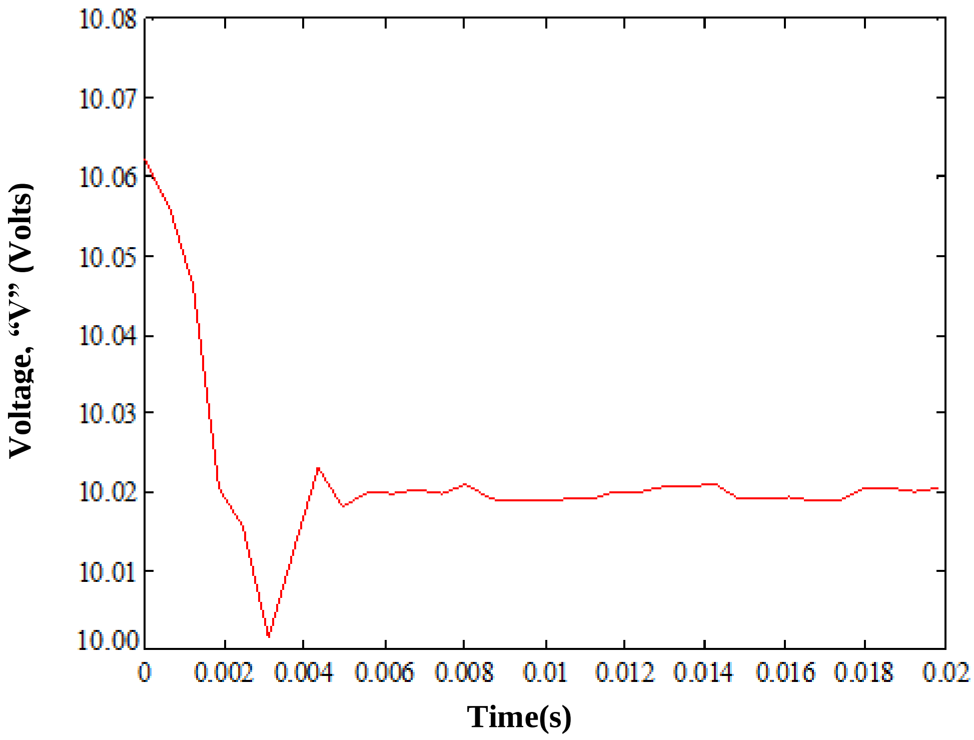

Figure 4.3: Plot of flow meter output voltage signal vs. time at 25 l/min.

The minimum and maximum flow settings were required to create a full measurement span for the high heat flux heater subjected to liquid spray cooling. The measurement span provides information about the measurement accuracy of the heater and its minimum and maximum attainable heat flux and corresponding excess temperature. Figure 4.4 presents a plot of the Fast Fourier Transform (FFT) vs. Frequency for the flow meter output voltage signal at the maximum flow rate setting (0.25 l/min). The FFT resolves a time waveform into its sinusoidal components. The FFT takes a block of time domain data and returns the frequency spectrum of the data. The FFT is a digital implementation of the Fourier transform. Thus, the FFT does not yield a continuous spectrum. As an alternative, the FFT returns a discrete spectrum in which the frequency content of the waveform is resolved into a finite number of frequency lines or bins.

The FFT for the flow meter signal was calculated using the data acquisition software and using the linear, peak-to-peak, and Gaussian settings. The purpose of using the FFT is to determine whether noise and vibrations have an influence on the measurements. Therefore, since a full measurement span for the high heat flux heater subjected to liquid spray cooling at the minimum and maximum flow settings was desired, the maximum flow rate (25 l/min) and corresponding frequency of the pump at this flow rate was the parameter which was expected to have the greatest effect on the measurements as far as vibrations are concerned. From Figure 4.4, the highest frequency peak spectrum of the flow meter signal at 25 l/min is at a frequency of approximately 167 Hz. The angular frequency of the rotary pump at 25 l/min was found to be 55.8 Hz.

The pump rotor has three blades. Each blade is considered to introduce a frequency of 55.8 Hz to the output signal of the void fraction sensor. The sum of the frequency of each blade is equal to 167.4 Hz. From Figure 4.4, it is evident that the pump has an effect on measurement performance. In a more elaborate since, the vibrations present in the loop have an effect on the flow meter performance. The next section will discuss the void fraction sensor performance.

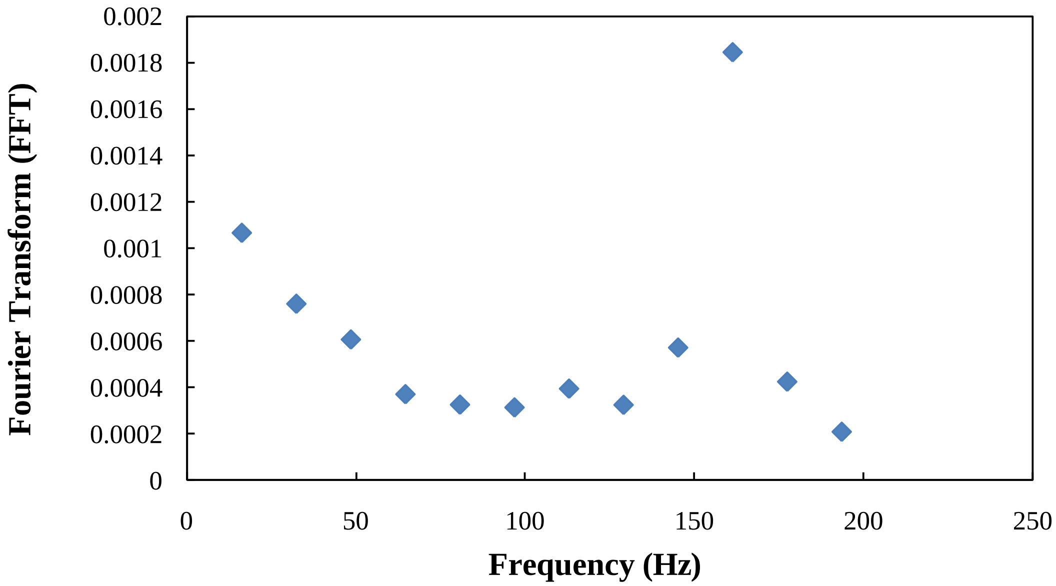

Figure 4.4: Plot of Fast Fourier Transform vs. frequency for the flow meter at 25 l/min.

4.2 Void Fraction Sensor Performance

The void fraction sensor was used to measure the void fraction of the flow field for the two dynamic loop test runs. Figure 4.5 presents a photograph of the void fraction sensor installed in the loop. After the sensor was installed a preliminary test was done to insure that the sensors output signal would be similar in comparison to the results obtained for the calibration tests mentioned in Chapter 3. During the preliminary test, the sensors output signal was observed to be affected by the connections of the copper piping to other metallic components in the loop.

Figure 4.5: Photograph of the void fraction sensor installed in the heat transfer loop developed and used in the present study.

The impedance amplifier requires adequate grounding. As a result, the measurement performance of the sensor is affected by poor grounding. The sensor ground-reference target is connected by two brass bushings which are also in contact with the brass pipe compression adapters. The bushings and brass compression adapters allows the flow of resistance through the copper pipes and other various metallic loop components. In this case, the entire loop is considered to be the ground, and the void fraction measurements would be skewed. In this case the sensor would need to be recalibrated, or modifications to the sensor adapters have to be made. To eliminate the effect of poor grounding, two plastic compression adapters were installed on the inlet and exit pipelines connecting the void fraction sensor to the loop. By installing plastic compression adapters, the flow of resistance is not transferred from the ground-reference target to other metallic components and copper piping throughout the loop, thus eliminating the effect of poor grounding on the output voltage signal.

A plot of the void fraction sensor output voltage signal vs. time is presented in Figure 4.6. The output voltage signal in Figure 4.6 was obtained at a flow rate of 25 l/min. The void fraction reading at 25 l/min was 0.0799. The average voltage over the total sampling time is 7.9160 V. However, it can be seen that the signal fluctuates about the mean due to random noise. Random noise can cause void fraction values slightly greater or less than the actual reading.

The amplifier was custom designed to be amplified on the order of 3X (three times the measurement span of a stock amplifier). The amplifier is highly sensitive when a dielectric is present in the electrostatic field created between the probe and ground-reference target. External influences such as surrounding dielectric materials, grounding issues, and vibrations can contribute to measurement uncertainty. Figure 4.7 and provides a plot of the Fast Fourier Transform vs. frequency for the void fraction sensor at a flow rate 25 l/min.

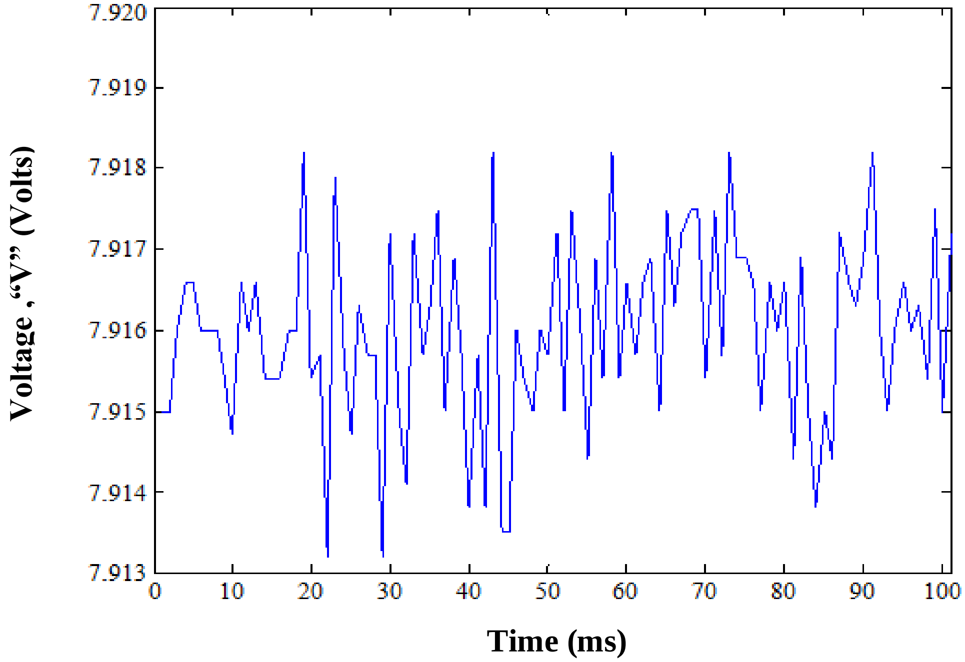

Figure 4.6: Plot of voltage output signal vs. time for Water.

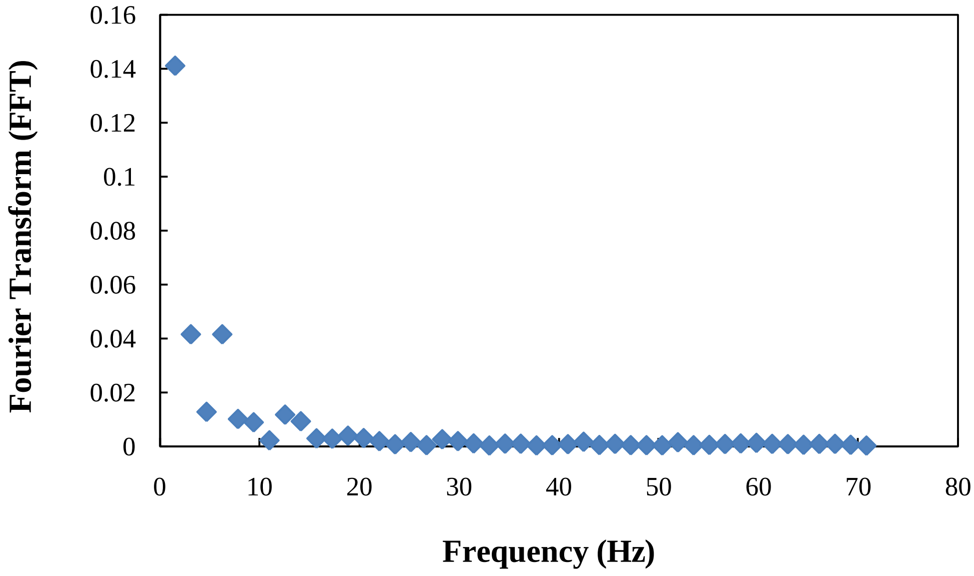

Figure 4.7: Plot of the Fast Fourier Transform vs. Frequency at 25 l/min for a frequency of 0-70 Hz for the void fraction sensor.

From Figure 4.7, the highest frequency peak spectrum of the void fraction sensor signal at 25 l/min is at a frequency of 1 Hz. The frequency of the rotary pump appears to not have the greatest effect on the void fraction sensor signal. The greatest effect is at 1 Hz. The effect of the frequency at 1 Hz could be due to the flow regime having an effect on the output signal or external influences such as grounding issues. The next section will discuss the pressure transducer performance.

4.3 Pressure Transducer Performance

The pressure transducers monitored pressure for both the minimum and maximum flow setting for the two loop test runs. A plot of the output voltage signal for the three pressure transducers at its minimum and maximum flow setting is presented in Figure 4.8 and Figure 4.9. The average pressure at the minimum flow setting (0.15 l/min) was found to be 0.0345 MPa (5 psi), and the average pressure at the maximum flow setting (25 l/min) was 0.124 MPa (18 psi).

Figure 4.10 presents a plot of the Fast Fourier Transform vs. frequency for the pressure transducers at a flow rate 25 l/min. From Figure 4.10, it is evident that the highest frequency peak spectrum of the pressure transducer output signal at 25 l/min is at a frequency of 8 Hz. The x-axis in the plot provided in Figure 4.10 was condensed to show the magnitude of the frequency spectrum. As the frequency increases, the magnitude of the FFT continues to decrease. As a result, the pump frequency does not have an effect on the pressure transducer signal. The effect of the frequency at 8 Hz could be due to flow regime or small spikes in the pressure transducer.

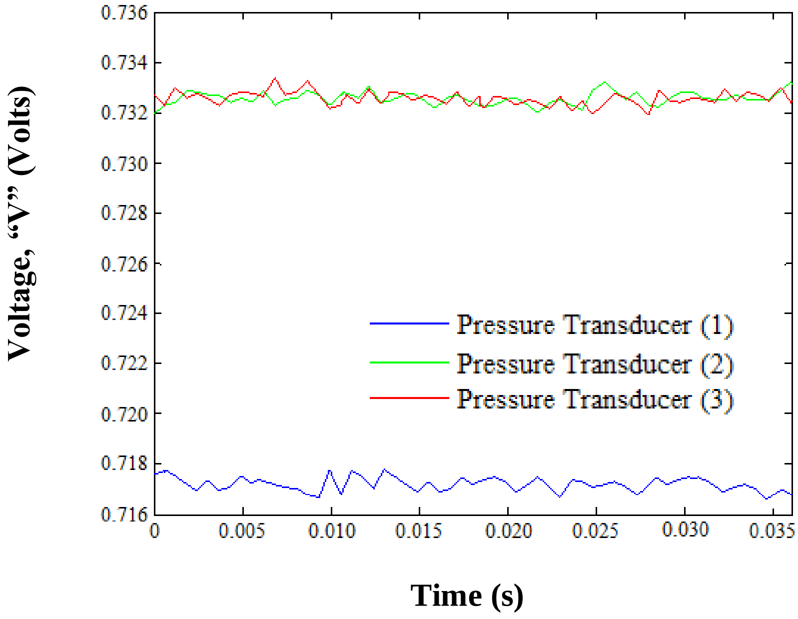

Figure 4.8: **Plot of output voltage signal vs. time for the pressure transducers at 0.15 l/min.**

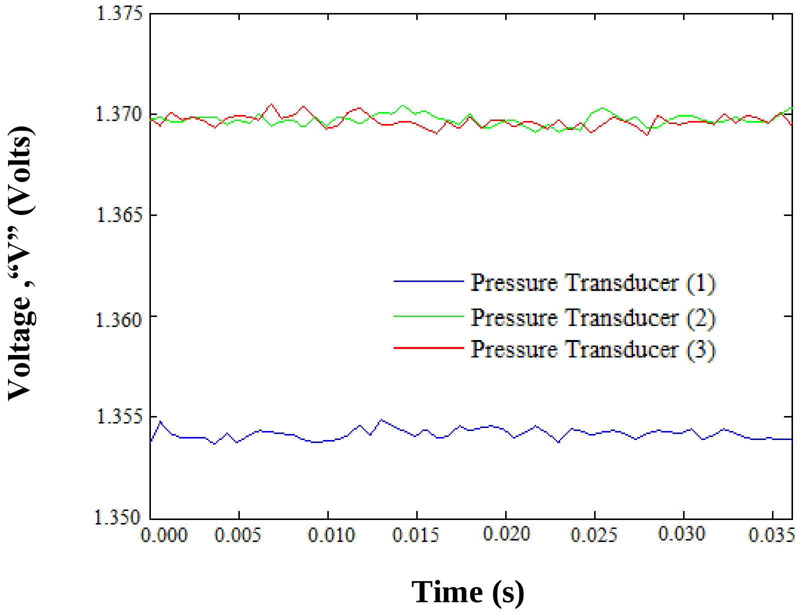

Figure 4.9: **Plot of output voltage signal vs. time for the pressure transducers at 25 l/min.**

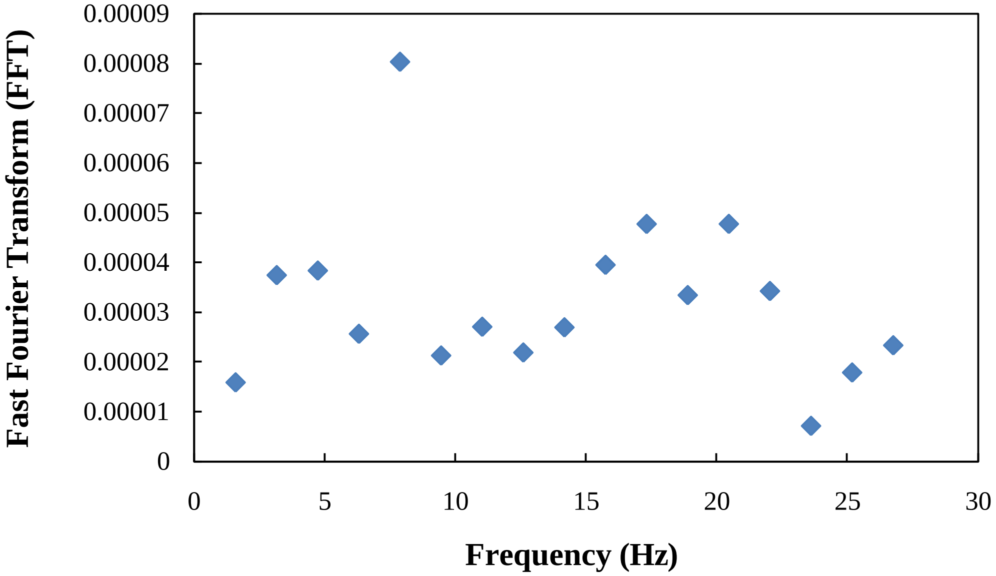

Figure 4.10: Plot of the Fast Fourier Transform vs. Frequency at 25 l /min for a frequency of 0-30 Hz for the pressure transducers.

4.4 Heater Performance

The spray cooling curve surface temperature vs. time for water flow rates of 0.15 l/min and 25 l/min are presented in Figure 4.11 and Figure 4.12 respectively. For the loop test runs the chiller was not used because the heat losses to the environment were sufficient. As a result, there was no need to run the heat exchanger. Five heat flux settings were used in the present study ranging from 180 to 3280 kW/m^2 (18-328 W/cm^2) as shown in both Figure 4.11 and Figure 4.12. The power supply used was only able to produce a maximum power of 0.328 kW (328 W). Heat flux is defined as the total power divided by the heated surface area.

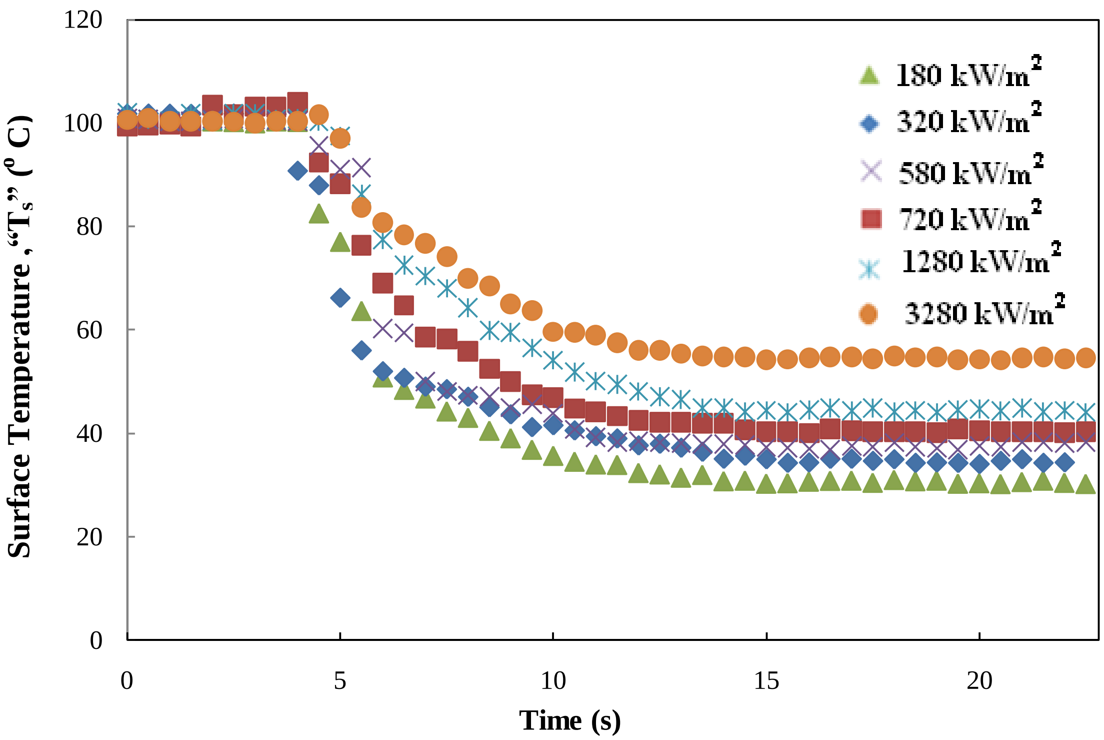

Figure 4.11: Spray cooling curve for the heater at 0.15 l/min.

For the minimum flow rate setting (0.15 l/min) the heater was allowed to reach a temperature of 100^{o}C before the liquid spray impingement process began. After the spray process began, the data acquisition system recorded the surface temperature "T_s" of the heater and ambient temperature "T_a" of the chamber control volume. For the maximum flow setting (25 l/min) and power settings ranging from 0.018-0.058 kW (18-58 W), the heater was allowed to reach its maximum surface temperature.

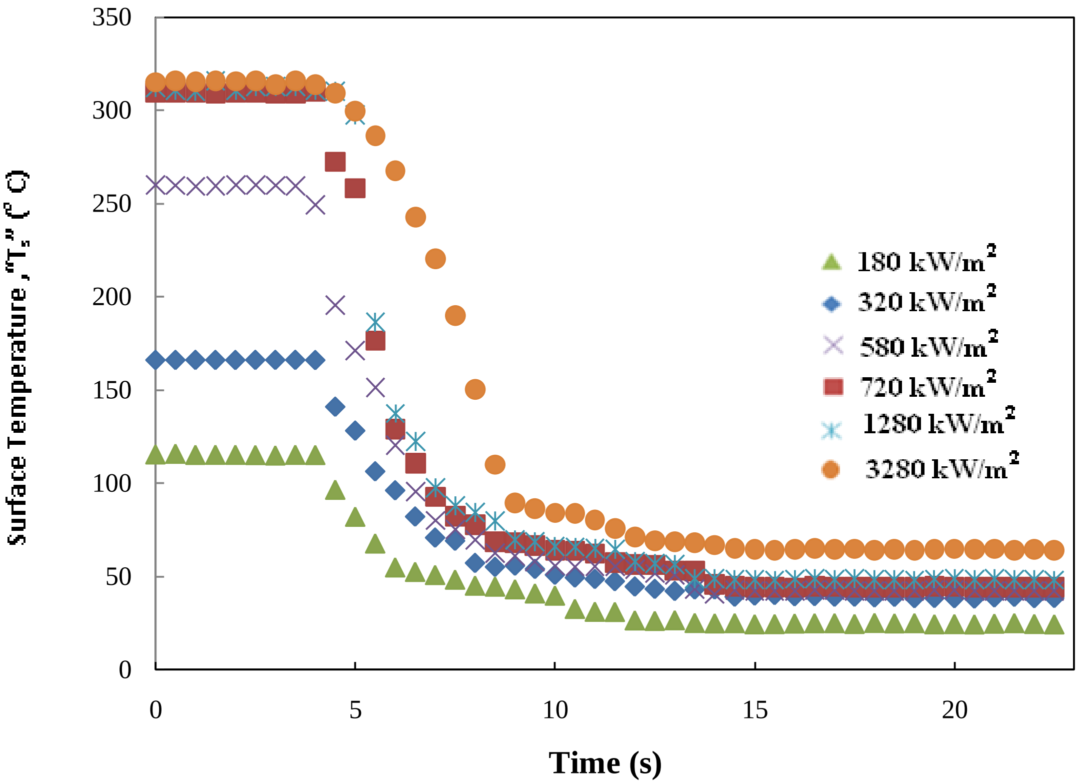

Figure 4.12: Spray cooling curve for the heater at 25 l/min.

A plot of the heat flux vs. excess temperature for the minimum and maximum flow rate setting is provided in Figure 4.13. For higher power settings ranging from 0.0728-0.328 kW (72-328 W), the maximum temperature that the heater was allowed to reach was 300°C. The excess temperature is defined as the difference in the surface temperature and the ambient temperature of the heater chamber control volume. As shown in Figure 4.13 the excess temperature increases with an increase of the heat flux. Also in Figure 4.13, the slope of the curve varies with heat flux. In the lower excess temperature region (T_s-T_a) less than 18°C for the maximum flow setting, the slope of the curve is relatively small. In this case, the heat transfer is mainly ruled by convection along with evaporation from the surface liquid film through slight nucleate boiling existing. As the surface temperature exceeds a point around 19°C, the slope of the curve becomes steeper.

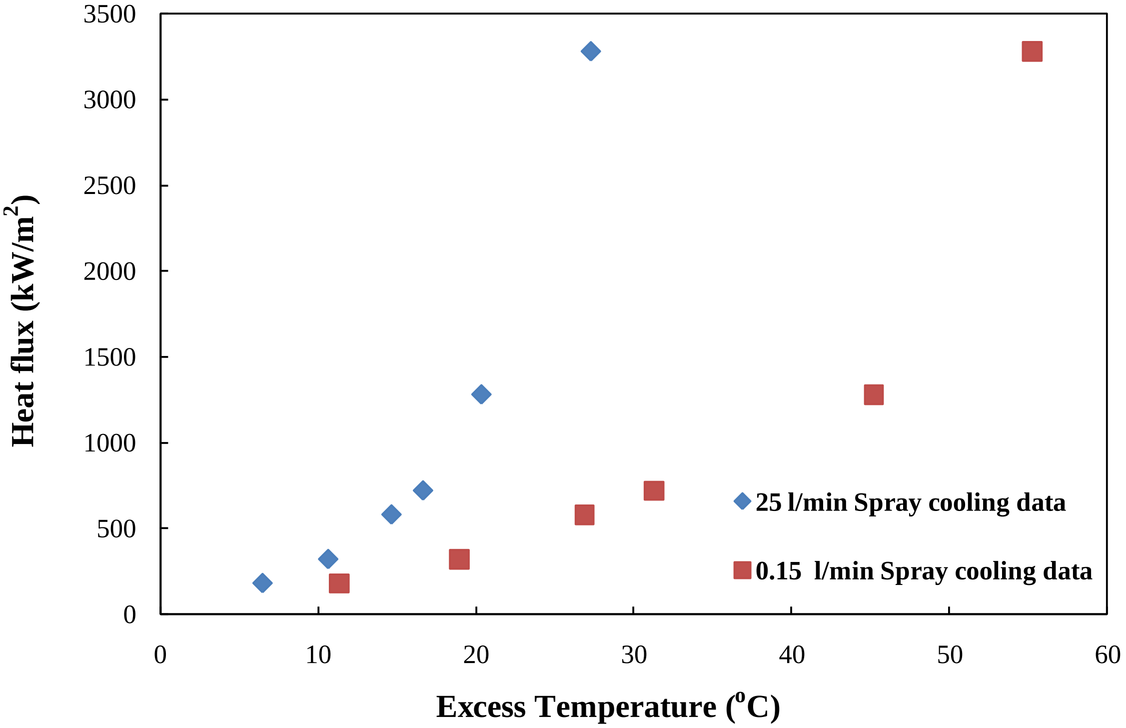

Figure 4.13: Plot of heat flux vs. excess temperature at 0.15 l/min.

For the minimum flow rate, in the excess temperature region (T_s-T_a) less than 33°C, the slope of the curve is relatively small. As the excess temperature exceeds a point around 33°C, the slope of the curve becomes steeper. Temperature data was also collected from the thermocouples placed at the inlet and exit of the heat exchanger. The minimum and maximum flow rate settings provided the necessary conditions to create a full measurement span for the high heat flux heater subjected to liquid spray cooling. The measurement span for the heater and its minimum and maximum flow settings suggests that the minimum attainable heat flux and excess temperature at a power setting of 180 kW (18 W) and a flow rate setting of 0.15 l/min is 180 kW/m^2 and 6.48^{o}C. The maximum attainable heat flux and corresponding excess temperature at a power setting of 3280 kW (328 W) is 3280 kW/m^2 (328 W/cm^2) and 55.3^{o}C.

CHAPTER 5

CONCLUSION

5.1 Conclusion

The specific objectives were formulated to provide the necessary measuring instruments and instrumentation for designing an efficient diagnostics and measuring system for the heat transfer spray cooling loop. The selected measuring tools proved to be suitable for measuring system parameters. The errors present were controllable enough to allow meaningful data collection. A discussion of the design criteria and results from a number of tests and experimental runs conducted has been presented.

From these tests, the following conclusions can be drawn:

1. The nonlinearity previously seen with the final void fraction sensor design during the calibration stages of the present study was due to the unequal lengths of the electrodes. This problem can be eliminated by making the ground-reference target length/diameter equal to the capacitance probe diameter.
2. Capacitance measurements during calibration of the void fraction sensor with water as the working fluid were found to be affected by the purity of water. Degradation of the media (working fluid) will cause an increase in conductance which will affect the measured capacitance. As a result, de-ionized or distilled water should be used for any calibrations that require water as the working fluid for future loop operation.

3. Design C (high heat flux heater) was sufficient in eliminating heat losses and providing sufficient heat to the heated surface area. Although the heater proves to be efficient, a better surface insulating material that can withstand the pressure and thermal shock of the liquid spray impingement process is needed for future studies.
4. Also thick film resistors have a small operational window; that is they can’t operate in the range above 190 to 260^{o}C or they will fracture. The thermal resistance of the copper plate and the thick film resistors substrate increased the backside temperature of the thick film resistors and caused the solder of the electrode leads to stick to the resistors. As a result, special attention should be afforded to mounting the resistors when using thick film resistors as the heating source for future studies.

5.2 Future Work

Some additional work needs to be conducted to improve the linearity of the void fraction sensor. Future studies should focus on improving the electrode design by making the ground electrode length the same as the diameter of the capacitance probe. Also, a high speed camera should be used for dynamic calibrations of the void fraction sensor for future studies. A full measurement span of the high heat flux heater ranging from the lowest power setting to its maximum setting of 10,000 kW/m^2 (1000 W/cm^2) was not achieved. Future studies would be focused on testing the heater at its maximum setting using the Agilent Technologies 6030-A power supply. Also an emergency shutdown switch for the heat transfer loop should be designed and implemented into the loop for safe operation.

REFERENCES

Abouelwafa, M. S. A., & Kendall, E. J. M. (1979), "Determination Of The Theoretical Capacitance Of A Concave Capacitance Sensor," *Review of Scientific Instruments, 50*(9), 1158-1159.

Abouelwafa, M. S. A., & Kendall, E. J. M. (1980), "The Use Of Capacitance Sensors For Phase Percentage Determination In Multiphase Pipelines," IEEE Transactions On Instrumentation And Measurement, 29(1), 24-27.

Aguilar, C., Lucia, J. F., & Simon, M. A. (2001), "An emerging role for interferon in haemophiliacs with chronic hepatitis C. Haemophilia," 7(1), 6-8.

Aguilar, G., Franco, W., Liu, J., Svaasand, L. O., & Nelson, J. S. (2005), "Effects of hypobaric pressure on human skin: Implications for cryogen spray cooling (part II)," Lasers in Surgery and Medicine, 36(2), 130-135.

Aguilar, G., Majaron, B., Pope, K., Svaasand, L. O., Lavernia, E. J., & Nelson, J. S. (2001), "Influence of nozzle-to-skin distance in cryogen spray cooling for dermatologic laser surgery," Lasers in Surgery and Medicine, 28(2), 113-120.

Ahmed, W. H. (2006). "Capacitance sensors for void-fraction measurements and flow-pattern identification in air-oil two-phase flow," IEEE Sensors Journal, 6(5), 1153-1163.

Bao, Z. Y., Fletcher, D. F., & Haynes, B. S. (2000). "Flow boiling heat transfer of Freon R11 and HCFC123 in narrow passages," International Journal of Heat and Mass Transfer, 43(18), 3347-3358.

Basinger, B., Aguilar, G., & Nelson, J. S. (2004). "Effect of skin indentation on heat transfer during cryogen spray cooling," Lasers in Surgery and Medicine, 34(2), 155-163.

Bertsch, S. S., Groll, E. A., & Garimella, S. V. (2009). "Effects of heat flux, mass flux, vapor quality, and saturation temperature on flow boiling heat transfer in microchannels," International Journal of Multiphase Flow, 35(2), 142-154.

Bostanci, H., Rini, D. P., Kizito, J. P., & Chow, L. C. (2009). "Spray Cooling With Ammonia on Microstructured Surfaces: Performance Enhancement and Hysteresis Effect," Journal of Heat Transfer-Transactions of the ASME, 131(7).

Caniere, H., T'Joen, C., Willockx, A., & De Paepe, M. (2008). "Capacitance signal analysis of horizontal two-phase flow in a small diameter tube," Experimental Thermal and Fluid Science, 32(3), 892-904.

Caniere, H., T'Joen, C., Willockx, A., De Paepe, M., Christians, M., van Rooyen, E., et al. (2007). "Horizontal two-phase flow characterization for small diameter tubes with a capacitance sensor," Measurement Science & Technology, 18(9), 2898-2906.

Chen, R. H., Chow, L. C., & Navedo, J. E. (2002). "Effects of spray characteristics on critical heat flux in subcooled water spray cooling," International Journal of Heat and Mass Transfer, 45(19), 4033-4043.

Cho, J., Perlin, M., & Ceccio, S. L. (2005). "Measurement of near-wall stratified bubbly flows using electrical impedance," Measurement Science & Technology, 16(4), 1021-1029.

Costigan, G., & Whalley, P. B. (1997). "Slug flow regime identification from dynamic void fraction measurements in vertical air-water flows," International Journal of Multiphase Flow, 23(2), 263-282.

Cutnell. J, K. J. (1998). Physics 4th Edition. John Wiley & Sons, Inc.

Das, R. K., & Pattanayak, S. (1993). "Electrical-Impedance Method For Flow Regime Identification In Vertical Upward Gas-Liquid 2-Phase Flow," Measurement Science & Technology, 4(12), 1457-1463.

Davis, A. (2010). "Design and Integration of System Components for a High Heat Flux Thermal Loop," Master of Science Thesis, North Carolina A&T State University.

Devia, F., & Fossa, M. (2003). "Design and optimisation of impedance probes for void fraction measurements," Flow Measurement and Instrumentation, 14(4-5), 139-149.

dos Reis, E., & Goldstein, L. (2005). "A non-intrusive probe for bubble profile and velocity measurement in horizontal slug flows," Flow Measurement and Instrumentation, 16(4), 229-239.

Dounan Jai, Z. W., Zhenwan Yu, and Dongming Qui. (1985). "Experimental Study of Void Fraction in Vertically Upward and Downward Liquid-gas Two-phase flow at low velocity," Two-phase Flow and Heat Transfer: China-U.S. Progress, Hemisphere Publishing Corporation, Washington D.C., p. 63-70.

Durst, F., Haddad, K., Al-Salaymeh, A., Eid, S., & Unsal, B. (2008). "Mass flow-rate control unit to calibrate hot-wire sensors," Experiments in Fluids, 44(2), 189-197.

Elkow, K. J., & Rezkallah, K. S. (1996). "Void fraction measurements in gas-liquid flows using capacitance sensors," Measurement Science & Technology, 7(8), 1153-1163.

Elkow, K. J., & Rezkallah, K. S. (1997). "Void fraction measurements in gas-liquid flows under 1-g and mu-g conditions using capacitance sensors," International Journal of Multiphase Flow, 23(5), 815-829.

F.P. Incropera, D. P. D., T.L. Bergman, A.S. Lavine. (2007). Fundamentals of Heat and Mass Transfer. New York: John Wiley & Sons.

Fernandez, D. P., Mulev, Y., Goodwin, A. R. H., & Sengers, J. (1995). "A Database For The Static Dielectric-Constant Of Water And Steam," Journal of Physical and Chemical Reference Data, 24(1), 33-69.

Fox R., M., A.,Pritchard P. Introduction to Fluid Mechanics, Second Edition. John Wiley & Sons, Inc.

G. W. Govier, M. M. (1962). "The Horizontal Pipeline Flow of Air-Water Mixtures," The Canadian Journal of Chemical Engineering, 40, 93.

Gao H. H., Z. F. D., and Chen X. J. (1985). "Void Fraction Measurement Using the Conductance-Probe Technique in Air-Water Two-phase Flow," Two-phase Flow and Heat Transfer: China-U.S. Progress, Hemisphere Publishing Corporation, Washington D.C., p. 57-62.

Geraets, J. J. M., & Borst, J. C. (1988). "A Capacitance Sensor For 2-Phase Void Fraction Measurement And Flow Pattern Identification," International Journal of Multiphase Flow, 14(3), 305-320.

Golnabi, H., & Azimi, P. (2008). "Simultaneous measurements of the resistance and capacitance using a cylindrical sensor system," Modern Physics Letters B, 22(8), 595-610.

Horacek, B., Kim, J., & Kiger, K. T. (2004). "Spray cooling using multiple nozzles: Visualization and wall heat transfer measurements," IEEE Transactions on Device and Materials Reliability, 4(4), 614-625.

Hosler, E. R., & Westwater, J. W. (1962). "Film Boiling On A Horizontal Plate," Ars Journal, 32(4), 553-558.

Hsu Y, G. R. (1976). Transport Processes in Boiling and Two-Phase Systems.

Jaworek, A., Krupa, A., & Trela, M. (2004). "Capacitance sensor for void fraction measurement in water/steam flows," *Flow Measurement and Instrumentation, 15*(5-6), 317-324.

Jiang, Y. J., & Rezkallah, K. S. (1993). "A Study On Void Fraction In Vertical Cocurrent Upward And Downward 2-Phase Gas-Liquid Flow .1," Experimental Results. *Chemical Engineering Communications, 126*, 221-243.

Johann, F., & Soergel, E. (2009). "Quantitative measurement of the surface charge density," *Applied Physics Letters, 95*(23).

Kelessidis, V. C., & Dukler, A. E. (1989). "Modeling Flow Pattern Transitions For Upward Gas-Liquid Flow In Vertical Concentric And Eccentric Annuli," *International Journal of Multiphase Flow, 15*(2), 173-191.

Keska, J. K., Smith, M. D., & Williams, B. E. (1999). "Comparison study of a cluster of four dynamic flow pattern discrimination techniques for multi-phase flow," *Flow Measurement and Instrumentation, 10*(2), 65-77.

Keska, J. K., & Williams, B. E. (1999). "Experimental comparison of flow pattern detection techniques for air-water mixture flow," *Experimental Thermal and Fluid Science, 19*(1), 1-12.

Kew, P. A., & Cornwell, K. (1997). "Correlations for the prediction of boiling heat transfer in small-diameter channels," *Applied Thermal Engineering, 17*(8-10), 705-715.

Lamarre, E., & Melville, W. K. (1992). "Instrumentation For The Measurement Of Void-Fraction In Breaking Waves - Laboratory And Field Results," *IEEE Journal of Oceanic Engineering, 17*(2), 204-215.

Lazarek, G. M., & Black, S. H. (1982). "Evaporative Heat-Transfer, Pressure-Drop And Critical Heat-Flux In A Small Vertical Tube With R-113," *International Journal of Heat and Mass Transfer, 25*(7), 945-960.

Lee, H. J., & Lee, S. Y. (2001). "Heat transfer correlation for boiling flows in small rectangular horizontal channels with low aspect ratios," *International Journal of Multiphase Flow, 27*(12), 2043-2062.

Lin, S., Kew, P. A., & Cornwell, K. (2001). "Two-phase heat transfer to a refrigerant in a 1 mm diameter tube," *International Journal Of Refrigeration-Revue Internationale Du Froid* , 1(24), 51-56.

Lowe, D., & Rezkallah, K. S. (1999). "A capacitance sensor for the characterization of microgravity two-phase liquid-gas flows," *Measurement Science & Technology, 10*(10), 965-975.

Mankin, R. W., & Callahan, P. S. (1977). "Derivation Of Equations Which Relate Effective Surface-Charge Density Of A Dielectric Or Electret To Measurable Parameters," Journal of Applied Physics, 48(3), 1372-1374.

Ming T Shu, C. B. W., and Young H. Lee. (1982). "A Simple Capacitance Sensor for Void Fraction Measurement in Two-Phase Flow," Ind. Eng. Chemi. Fundam, 21(2).

Mudawar, I., & Estes, K. A. (1996). "Optimizing and predicting CHF in spray cooling of a square surface," Journal of Heat Transfer-Transactions of the ASME, 118(3), 672-679.

Oddie, G., & Pearson, J. R. A. (2004). "Flow-Rate measurement in two-phase flow," Annual Review of Fluid Mechanics, 36, 149-172.

Ong, C. L., & Thome, J. R. (2009). "Flow boiling heat transfer of R134a, R236fa and R245fa in a horizontal 1.030 mm circular channel," Experimental Thermal and Fluid Science, 33(4), 651-663.

Ortiz, L., & Gonzalez, J. E. (1999). "Experiments on steady-state high heat fluxes using spray cooling," Experimental Heat Transfer, 12(3), 215-233.

Pitzer, K. S. (1983). "Dielectric-Constant Of Water At Very High-Temperature And Pressure," Proceedings of the National Academy of Sciences of the United States of America-Physical Sciences, 80(14), 4575-4576.

Ravigururajan, T. S. (1998). "Impact of channel geometry on two-phase flow heat transfer characteristics of refrigerants in microchannel heat exchangers," Journal of Heat Transfer-Transactions of the ASME, 120(2), 485-491.

Reedyk, C. W., & Perlman, M. M. (1968). "Measurement Of Surface Change," Journal of the Electrochemical Society, 115(1), 49-55.

S.J Kline, F. A. M. (1953). "Describing uncertainties in single-sample experiments," Mech. Eng. , 75 (1), 3-8.

Silk, E. A., Kim, J., & Kiger, K. (2006). "Spray cooling of enhanced surfaces: Impact of structured surface geometry and spray axis inclination," International Journal of Heat and Mass Transfer, 49(25-26), 4910-4920.

Su, J., & Chwang, A. T. (2007). "Estimation of heat transfer coefficient of cryogen spray cooling with Alifanov's iterative regularization method," Numerical Heat Transfer Part a-Applications, 51(8), 781-794.

Svaasand, L. O., Randeberg, L. L., Aguilar, G., Majaron, B., Kimel, S., Lavernia, E. J., et al. (2003). "Cooling efficiency of cryogen spray during laser therapy of skin," Lasers in Surgery and Medicine, 32(2), 137-142.

Taitel, Y., Bornea, D., & Dukler, A. E. (1980). "Modeling Flow Pattern Transitions For Steady Upward Gas-Liquid Flow In Vertical Tubes," AICHE Journal, 26(3), 345-354.

Taitel, Y., & Dukler, A. E. (1976). "Model For Predicting Flow Regime Transitions In Horizontal And Near Horizontal Gas-Liquid Flow," AICHE Journal, 22(1), 47-55.

Taitel, Y., Lee, N., & Dukler, A. E. (1978). "Transient Gas-Liquid Flow In Horizontal Pipes - Modeling Flow Pattern Transitions," AICHE Journal, 24(5), 920-934.

Tollefsen, J., & Hammer, E. A. (1998). "Capacitance sensor design for reducing errors in phase concentration measurements," Flow Measurement and Instrumentation, 9(1), 25-32.

Tran, T. N., Wambsganss, M. W., & France, D. M. (1996). "Small circular- and rectangular-channel boiling with two refrigerants," International Journal of Multiphase Flow, 22(3), 485-498.

Wambsganss, M. W., France, D. M., Jendrzejczyk, J. A., & Tran, T. N. (1993). "Boiling Heat-Transfer In A Horizontal Small-Diameter Tube," Journal of Heat Transfer-Transactions of the ASME, 115(4), 963-972.

Wang, L. H., Chen, M., & Groll, M. (2009). "Flow Boiling Heat Transfer Characteristics of R134a in a Horizontal Mini Tube," Journal of Chemical and Engineering Data, 54(9), 2638-2645.

Warrier, G. R., Dhir, V. K., & Momoda, L. A. (2002). "Heat transfer and pressure drop in narrow rectangular channels," Experimental Thermal and Fluid Science, 26(1), 53-64.

Wen, D. S., Yan, Y. Y., & Kenning, D. B. R. (2004). "Saturated flow boiling of water in a narrow channel: time-averaged heat transfer coefficients and correlations," Pergamon-Elsevier Science Ltd

Yan, Y. Y., & Lin, T. F. (1999). "Evaporation heat transfer and pressure drop of refrigerant R-134a in a plate heat exchanger," *Journal of Heat Transfer-Transactions of the ASME, 121*(1), 118-127.

Yu, W., France, D. M., Wambsganss, M. W., & Hull, J. R. (2002). "Two-phase pressure drop, boiling heat transfer, and critical heat flux to water in a small-diameter horizontal tube," *International Journal of Multiphase Flow, 28*(6), 927-941.

Zhou, D. W., & Lee, S. J. (2007). "Forced convective heat transfer with impinging rectangular jets," *International Journal of Heat and Mass Transfer, 50*(9-10), 1916-1926.

APPENDIX A

HEATER SCALING ANALYSIS

The following analysis is applied to the heater schematic and coordinate axis presented in Figure 3.14 of Chapter 3.

$$\frac{\partial u}{\partial x}+\frac{\partial v}{\partial y}=0 \tag{A.1}$$

$$\rho\left(u\frac{\partial u}{\partial x}+v\frac{\partial u}{\partial y}\right)=-\frac{\partial P}{\partial x}+\mu\left(\frac{\partial^2 u}{\partial x^2}+\frac{\partial^2 u}{\partial y^2}\right) \tag{A.2}$$

$$\rho c_p\left(u\frac{\partial T}{\partial x}+v\frac{\partial T}{\partial y}\right)=k\left(\frac{\partial^2 T}{\partial x^2}+\frac{\partial^2 T}{\partial y^2}\right) \tag{A.3}$$

$$A=\frac{L}{H}=\frac{0.0254}{0.0018}=14.11$$

To non-dimensionalize these equations, divide the length and the height by a reference length "L" and height "H" and all the velocities by a reference velocity, V and V_∞. Make the pressure non-dimensional by dividing by $\rho V_\infty^{\ 2}$ (twice the freestream dynamic pressure). The non-dimensional temperature is presented as $T-T_S/T_\infty-T_S$. Denoting non-dimensional quantities with asterisks, the following expressions can be obtained:

$$x^*=\frac{x}{L},y^*=\frac{y}{H},u^*=\frac{u}{V_\infty},v^*=\frac{v}{V},P^*=\frac{P}{\rho V_\infty^{\ 2}},T^*=\frac{T-T_S}{T_\infty-T_S}$$

To illustrate the procedure for non-dimensionalizing the equations, consider the partial derivative terms in the equations:

$$u\frac{\partial u}{\partial x}=\left(u^{*}V_{\infty}\right)\frac{\partial(u^{*}V_{\infty})}{\partial(x^{*}L)}=u^{*}\frac{V_{\infty}{}^{2}}{L}\frac{\partial u^{*}}{\partial x^{*}} \tag{A.4}$$

$$v\frac{\partial u}{\partial y}=\left(v^{*}V\right)\frac{\partial(u^{*}V_{\infty})}{\partial(y^{*}H)}=v^{*}\frac{V_{\infty}V}{H}\frac{\partial u^{*}}{\partial y^{*}}=v*\frac{V_{\infty}\left(V_{\infty}H/L\right)}{H}\frac{\partial u*}{\partial y*}=\frac{V_{\infty}{}^{2}}{L}v*\frac{\partial u*}{\partial y*} \tag{A.5}$$

$$v\frac{\partial T}{\partial y}=\left(v^{*}V\right)\frac{\partial(T^{*}(T_{\infty}-T_{S})+T_{S})}{\partial(y^{*}H)}=v^{*}\frac{VT_{\infty}}{H}\frac{\partial T^{*}}{\partial y^{*}} \tag{A.6}$$

$$\frac{\partial^{2}u}{\partial x^{2}}=\frac{\partial}{\partial x}\left(\frac{\partial u}{\partial x}\right)=\frac{\partial}{\partial(x^{*}L)}\frac{\partial(u^{*}V_{\infty})}{\partial(x^{*}L)}=\frac{V_{\infty}}{L^{2}}\frac{\partial^{2}u^{*}}{\partial x^{*2}} \tag{A.7}$$

$$\frac{\partial^{2}u}{\partial y^{2}}=\frac{\partial}{\partial y}\left(\frac{\partial u}{\partial y}\right)=\frac{\partial}{\partial(y^{*}H)}\frac{\partial(u^{*}V_{\infty})}{\partial(y^{*}H)}=\frac{V_{\infty}}{H^{2}}\frac{\partial^{2}u^{*}}{\partial y^{*2}} \tag{A.8}$$

$$\frac{\partial P}{\partial x}=\frac{\partial(\rho P^{*}V_{\infty}{}^{2})}{\partial(x^{*}L)}=\frac{\rho V_{\infty}{}^{2}}{L}\frac{\partial P^{*}}{\partial x} \tag{A.9}$$

$$\frac{\partial^{2}T}{\partial x^{2}}=\frac{\partial}{\partial x}\left(\frac{\partial T}{\partial x}\right)=\frac{\partial}{\partial(x^{*}L)}\frac{\partial(T^{*}(T_{\infty}-T_{s})+T_{s})}{\partial(x^{*}L)}=\frac{T_{\infty}}{L^{2}}\frac{\partial^{2}T^{*}}{\partial x^{*2}} \tag{A.10}$$

$$\frac{\partial^{2}T}{\partial y^{2}}=\frac{\partial}{\partial y}\left(\frac{\partial T}{\partial y}\right)=\frac{\partial}{\partial(y^{*}H)}\frac{\partial(T^{*}(T_{\infty}-T_{s}+T_{s})}{\partial(y^{*}H)}=\frac{T_{\infty}}{H^{2}}\frac{\partial^{2}T^{*}}{\partial y^{*2}} \tag{A.11}$$

By following this procedure, the continuity equation can be written as:

$$\left(\frac{V_{\infty}}{L}\frac{\partial u^{*}}{\partial x^{*}}+\frac{V}{H}\frac{\partial v^{*}}{\partial y^{*}}\right)=0 \tag{A.12}$$

To satisfy the continuity equation, the constants must be equal to reduce the equation to zero. Therefore: $\frac{V_{\infty}}{L}=\frac{V}{H},V=\frac{V_{\infty}H}{L}$, $V=\frac{V_{\infty}H}{L}=V_{\infty}A$

Substituting: $V=V_{\infty}H/L$ yields:

$$\left(\frac{V_\infty}{L}\frac{\partial u^*}{\partial x^*}+\frac{\frac{V_\infty H}{L}}{H}\frac{\partial v^*}{\partial y^*}\right)=0$$

(A.13)

The continuity equation reduces to:

$$\left(\frac{V_\infty}{L}\frac{\partial u^*}{\partial x^*}+\frac{V_\infty}{L}\frac{\partial v^*}{\partial y^*}\right)=0$$

(A.14)

Dividing by V_∞/L yields:

$$\frac{\partial u^*}{\partial x^*}+\frac{\partial v^*}{\partial y^*}=0$$

(A.15)

Following the same procedure for the x-momentum and energy equation yields:

$$\rho\left(u\frac{\partial u}{\partial x}+v\frac{\partial u}{\partial y}\right)=-\frac{\partial P}{\partial x}+\mu\left(\frac{\partial^2 u}{\partial x^2}+\frac{\partial^2 u}{\partial y^2}\right)$$

(A.16)

$$\rho\left(u^*\frac{V_\infty{}^2}{L}\frac{\partial u^*}{\partial x^*}+v^*\frac{V_\infty\frac{(V_\infty H)}{L}}{H}\frac{\partial u^*}{\partial y^*}\right)=-\frac{\rho V_\infty{}^2}{L}\frac{\partial P^*}{\partial x}+\mu\left(\frac{V_\infty}{L^2}\frac{\partial^2 u^*}{\partial x^{*2}}+\frac{V_\infty}{H^2}\frac{\partial^2 u^*}{\partial y^{*2}}\right)$$

(A.17)

$$\frac{\rho V_\infty{}^2}{L}\left(u^*\frac{\partial u}{\partial x}+v^*\frac{\partial u}{\partial y}\right)=-\frac{\rho V_\infty{}^2}{L}\frac{\partial P^*}{\partial x^*}+\mu V_\infty\left(\frac{1}{L^2}\frac{\partial^2 u^*}{\partial x^{*2}}+\frac{1}{H^2}\frac{\partial^2 u^*}{\partial y^{*2}}\right)$$

(A.18)

$$\frac{\rho V_\infty{}^2}{L}\left(u^*\frac{\partial u}{\partial x}+v^*\frac{\partial u}{\partial y}\right)=-\frac{\rho V_\infty{}^2}{L}\frac{\partial P^*}{\partial x^*}+\frac{\mu V_\infty}{H^2}\frac{L^2}{L^2}\left(\frac{H^2}{L^2}\frac{\partial^2 u^*}{\partial x^{*2}}+\frac{\partial^2 u^*}{\partial y^{*2}}\right)$$

(A.19)

Substituting the aspect ratio: $A=L/H$, yields:

$$\left(u^*\frac{\partial u}{\partial x}+v^*\frac{\partial u}{\partial y}\right)=-\frac{\partial P^*}{\partial x^*}+\frac{\mu L}{\rho V_\infty H^2}\frac{L^2}{L^2}\left(\frac{1}{A^2}\frac{\partial^2 u^*}{\partial x^{*2}}+\frac{\partial^2 u^*}{\partial y^{*2}}\right)$$ **(A.20)**

$$\frac{H^2}{L^2}\left(u^*\frac{\partial u}{\partial x}+v^*\frac{\partial u}{\partial y}\right)=-\frac{\partial P^*}{\partial x^*}+\frac{1}{\mathrm{Re}}\left(\frac{1}{A^2}\frac{\partial^2 u^*}{\partial x^{*2}}+\frac{\partial^2 u^*}{\partial y^{*2}}\right) \tag{A.21}$$

The Energy equation becomes:

$$\rho c_p\left(u^*\frac{V_\infty T_\infty}{L}\frac{\partial T^*}{\partial x^*}+v^*\frac{VT_\infty}{H}\frac{L}{L}\frac{\partial T^*}{\partial y^*}\right)=k\left(\frac{T_\infty}{L^2}\frac{\partial^2 T^*}{\partial x^{*2}}\frac{H^2}{H^2}+\frac{T_\infty}{H^2}\frac{\partial^2 T^*}{\partial y^{*2}}\right) \tag{A.22}$$

divide by T_∞ yields:

$$\frac{\rho c_p}{L}\left(u^* V_\infty\frac{\partial T^*}{\partial x^*}+v^*\frac{\frac{V_\infty H}{L}\,L}{H}\frac{\partial T^*}{\partial y^*}\right)=\frac{k}{H^2}\left(\frac{\partial^2 T^*}{\partial x^{*2}}\frac{H^2}{L^2}+\frac{\partial^2 T^*}{\partial y^{*2}}\right) \tag{A.23}$$

$$\frac{\rho c_p}{L}\left(u^* V_\infty\frac{\partial T^*}{\partial x^*}+v^* V_\infty\frac{\partial T^*}{\partial y^*}\right)=\frac{k}{H^2}\left(\frac{\partial^2 T^*}{\partial x^{*2}}\frac{H^2}{L^2}+\frac{\partial^2 T^*}{\partial y^{*2}}\right) \tag{A.24}$$

$$\frac{V_\infty \rho c_p}{L}\left(u^*\frac{\partial T^*}{\partial x^*}+v^*\frac{\partial T^*}{\partial y^*}\right)=\frac{k}{H^2}\left(\frac{H^2}{L^2}\frac{\partial^2 T^*}{\partial x^{*2}}+\frac{\partial^2 T^*}{\partial y^{*2}}\right) \tag{A.25}$$

$$\frac{V_\infty \rho c_p}{L}\left(u^*\frac{\partial T^*}{\partial x^*}+v^*\frac{\partial T^*}{\partial y^*}\right)=\frac{k}{H^2}\left(\frac{1}{A^2}\frac{\partial^2 T^*}{\partial x^{*2}}+\frac{\partial^2 T^*}{\partial y^{*2}}\right) \tag{A.26}$$

$$\left(u^*\frac{\partial T^*}{\partial x^*}+v^*\frac{\partial T^*}{\partial y^*}\right)=\frac{kL}{\rho c_p H^2 V_\infty}\frac{L^2}{L^2}\left(\frac{1}{A^2}\frac{\partial^2 T^*}{\partial x^{*2}}+\frac{\partial^2 T^*}{\partial y^{*2}}\right) \tag{A.27}$$

$$\left(u^*\frac{\partial T^*}{\partial x^*}+v^*\frac{\partial T^*}{\partial y^*}\right)=\frac{\alpha L^2}{H^2 V_\infty L}\left(\frac{1}{A^2}\frac{\partial^2 T^*}{\partial x^{*2}}+\frac{\partial^2 T^*}{\partial y^{*2}}\right) \tag{A.28}$$

$$\frac{H^2}{L^2}\left(u^*\frac{\partial T^*}{\partial x^*}+v^*\frac{\partial T^*}{\partial y^*}\right)=\frac{1}{Pe}\left(\frac{1}{A^2}\frac{\partial^2 T^*}{\partial x^{*2}}+\frac{\partial^2 T^*}{\partial y^{*2}}\right) \tag{A.29}$$

The Reynolds number: $\mathrm{Re} = V_{\infty} L / \nu$, and in Eqn. A.29 there is the Peclet number $V_{\infty} L / \alpha$. However, the Peclet number is replaced by the product of the Reynolds and Prandtl number, $Pe = \mathrm{Re}\,\mathrm{Pr}$

$$\frac{1}{A^2}\left(u^* \frac{\partial T^*}{\partial x^*} + v^* \frac{\partial T^*}{\partial y^*} \right) = \frac{1}{\mathrm{Re}\,\mathrm{Pr}}\left(\frac{1}{A^2}\frac{\partial^2 T^*}{\partial x^{*2}} + \frac{\partial^2 T^*}{\partial y^{*2}} \right) \qquad \textbf{(A.30)}$$

APPENDIX B

UNCERTAINTY ANALYSIS

Each of the measuring tools used in the present study has a linear voltage output. As a result, the measuring parameter of interest at any intermediate voltage can be obtained from:

$$\frac{N - N_{\min}}{N_{\max} - N_{\min}} = \frac{V_{out} - V_{\min}}{V_{\max} - V_{\min}} \qquad \textbf{(B.1)}$$

where N is the parameter measured from the measuring instrument and V is the voltage output of the measuring instrument. For each measuring instrument a least squares line fit was obtained through calibration data. The curve fit is of the form:

$$N(V) = c_1(V) + c_2 \qquad \textbf{(B.2)}$$

Eqn. B.1 can be manipulated into the form of Eqn. B.2; a direct curve fit to the calibration data has the potential of being more accurate. After a curve fit to Eqn. B.2 is obtained, the residual of the fit is computed at each point of the calibration data set. The residual for each data point "i" is:

$$r_i = N_{fit,i} - N_i \qquad \textbf{(B.3)}$$

The uncertainty in using the calibration equation is due to the accuracy of the measuring instrument and the ability of the curve fit to represent calibration data.

$$c_1 = \frac{N_{\max} - N_{\min}}{V_{\max} - V_{\min}} \qquad c_2 = \frac{N_{\min} N_{\max} - N_{\max} V_{\min}}{V_{\max} - V_{\min}}$$

A conservative interpretation of this error specification is that the calibration data supplied with the measuring instrument is accurate to within:

$$u_{calibration} = (N_{max} - N_{min}) \times \text{maximum full scale error specification} \qquad \textbf{(B.4)}$$

The error using the conversion equation is denoted u_{fit} and is used to predict the calibration data. If the curve fit from the preceding section is used, then $u_{fit} = r_{\max}$. The $u_{calibration}$ and u_{fit} errors are assumed to be uncorrelated, therefore the two can be combined to form the root-sum-squared method. The uncertainty of other instrumental errors in the procedure is denoted u_n. Thus, the total uncertainty in the measuring instrument is:

$$u_{total} = \sqrt{u^2{}_{calibration} + u^2{}_{fit} + \ldots u_n{}^2} \qquad \textbf{(B.5)}$$

A Matlab script file was used which implemented the uncertainty equations and the output voltage values of each measuring instrument to obtain the measurement uncertainties.

APPENDIX C

FLOW ANALYSIS

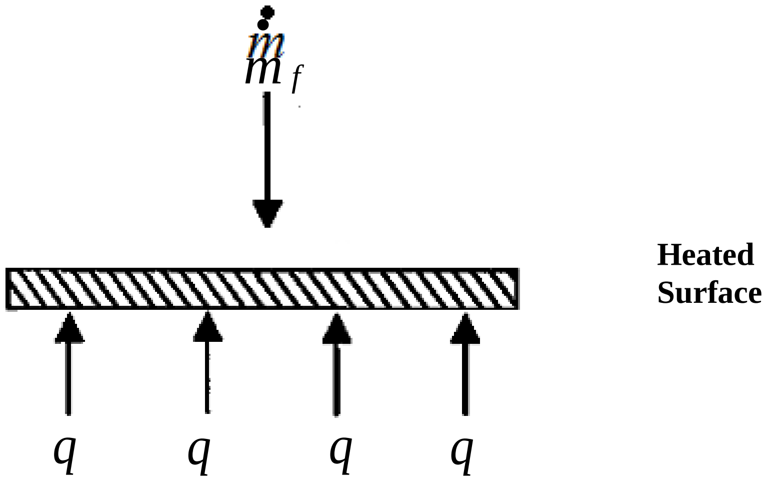

Figure C.1: Schematic of the heated surface with an evenly distributed heat flux balanced by an incoming mass flow rate.

In this analysis, the heated surface is cooled by an incoming liquid mass flow rate under steady-state operation. The incoming liquid mass flow rate “m_f” is continuously flowing into the heater chamber and then exits the chamber as a vapor-phase at the same mass flow rate. The known parameters are the heat flux and the fluid properties. The unknown in this case is the mass flow rate required to maintain the heat flux. The conditions of the system and surroundings are provided accordingly.

Conditions:

1. The flow analysis is based on a steady-flow process since there is no change with time at any point and thus $\Delta m_{CV}=0$ and $\Delta E_{CV}=0$.
2. The kinetic and potential energies are negligible, thus $ke \cong pe \cong 0$.

3. There is no work interaction involved.

Analysis:

The schematic of the heated surface shown in Figure C.1 is the control volume. There is only one inlet and one exit, thus:

$$\dot{m}_{in} = \dot{m}_{out} \ (kg/s) \tag{C.1}$$

Noting that the energy can be transferred by heat, work, and mass only, the energy balance in Eqn. C.2 for a general steady-state flow system can also be written more explicitly as:

$$\dot{Q}_{in} + W_{in} + \sum_{in} \dot{m}\theta = \dot{Q}_{out} + W_{out} + \sum_{out} \dot{m}\theta \tag{C.2}$$

where:

$$\theta = \left(h + \frac{V^2}{2} + gz \right) \tag{C.3}$$

$$\dot{Q}_{in} + W_{in} + \sum_{in} \dot{m}\left(h + \frac{V^2}{2} + gz \right) = \dot{Q}_{out} + W_{out} + \sum_{out} \dot{m}\left(h + \frac{V^2}{2} + gz \right) \tag{C.4}$$

Applying the conditions of the system to the energy balance yields:

$$\dot{Q}_{in} + \dot{W}_{in} + \sum_{in} \dot{m}\left(h + \frac{V^2}{2} + gz \right) = \dot{Q}_{out} + \dot{W}_{out} + \sum_{out} \dot{m}\left(h + \frac{V^2}{2} + gz \right) \tag{C.5}$$

From Eqn. C.2, the mass flow rate of the fluid and vapor are considered to be the same. The heat load“ Q ”, can be written as: $Q = qA_{hs}$. The energy balance from Eqn. C.5 reduces to:

$$\dot{q}\,A_{hs} = \dot{m}_f\, h_{fg} \tag{C.6}$$

Solving for the fluid mass flow rate yields:

$$\dot{m}_f = \frac{\dot{q}\,A_{hs}}{h_{fg}} \tag{C.7}$$

The energy balance relation is intuitive in nature and is easy to use when the magnitudes and directions of heat and work transfer are known. The flow was considered to be a steady-flow process and the control volume is constant; thus, there is no boundary work involved. The work required to push mass into and out of the control volume is taken care of by using enthalpies for the energy of fluid streams instead of internal energies. For the heat transfer, it is assumed that the system is well insulated and $Q_{in} = Q_{out} = 0$. The mass flow rate required to maintain a heat flux of 10,000 kW/m^2 (1000 W/cm^2) is obtained using Eqn. C.7 is found to be:

$$m_f = \frac{qA_h}{h_{fg}} = \frac{\left(1000\frac{W}{cm^2}\right)\times\left(1cm^2\right)}{\left(142\frac{kJ}{kg}\right)\times\left(\frac{1000J}{1kJ}\right)} = 0.007\frac{kg}{s} \tag{C.8}$$

From continuity, the following expression is true:

$$m_f = (\rho_f V_f A_p) \tag{C.9}$$

Solving for the fluid velocity yields:

$$V_f = \frac{m_f}{(\rho_f \times A_p)} = \frac{\left(0.007\frac{kg}{s}\right)}{\left(1400\frac{kg}{m^3}\times 0.000127m^2\right)} = 0.04\frac{m}{s} \tag{C.10}$$

The corresponding volumetric flow rate is obtained using the following equation:

$$Q_f = V_f A_p = \left(0.004\frac{m}{s} \times 0.00127 m^2\right) = 5 \times 10^{-6}\frac{m^3}{s} \quad \textbf{(C.11)}$$

From the results obtained from the above analysis, a flow meter was needed to measure a volumetric flow rate of at least 5x10^{-6} m^3/s (0.3 l/min) to maintain a heat flux of 10,000 kW/m (1000 W/cm^2) with Novec 7000 as the working fluid. When considering water as the working fluid a flow meter capable of reading as low as 0.19 l/min was needed.

APPENDIX D

PHYSICS OF A CAPACITANCE MEASURING SYSTEM

The measured capacitance of a capacitor is affected by the geometry of the electrodes and the properties of the dielectric material within the electric field. Capacitance sensors electronically measure the capacitance between two or more electrodes separated by a dielectric material. If a dielectric material is placed within the electric field between the plates of a parallel plate capacitor, the capacitance increases. Figure D.1 demonstrates the effect of a dielectric material in the presence of an electric field. In part (a) the sensing control volume is empty and therefore the electric field is not affected. In a parallel plate capacitor, the electric field lines are oriented from the positive charged plate to the negative charged plate. In part (b), the effect of the electric field by inserting a dielectric material between the plates is demonstrated.

Since the capacitor has no applied voltage, the charge on the plate remains constant as the dielectric is inserted. Due to surface charge effects on the dielectric, not all the electric field lines will pass through the dielectric material. As shown in Figure D.1c, several field lines will result to the negative charged surface and initiate again on the positive charged surface. While maintaining a constant charge on both plates, the electric field inside the dielectric is less than the electric field inside vacuum. The reduction in the electric field is due to the dielectric constant κ, which is expressed as:

$$\kappa = \frac{E_o}{E} \qquad \textbf{(D.1)}$$

where E_o is the electric potential in vacuum and E is the electric potential in the presence of a dielectric material. The dielectric constant is a dimensionless quantity. The magnitude of the electric field inside the dielectric is given as:

$$E = \frac{E_o}{\kappa} = \frac{V}{d} \qquad \textbf{(D.2)}$$

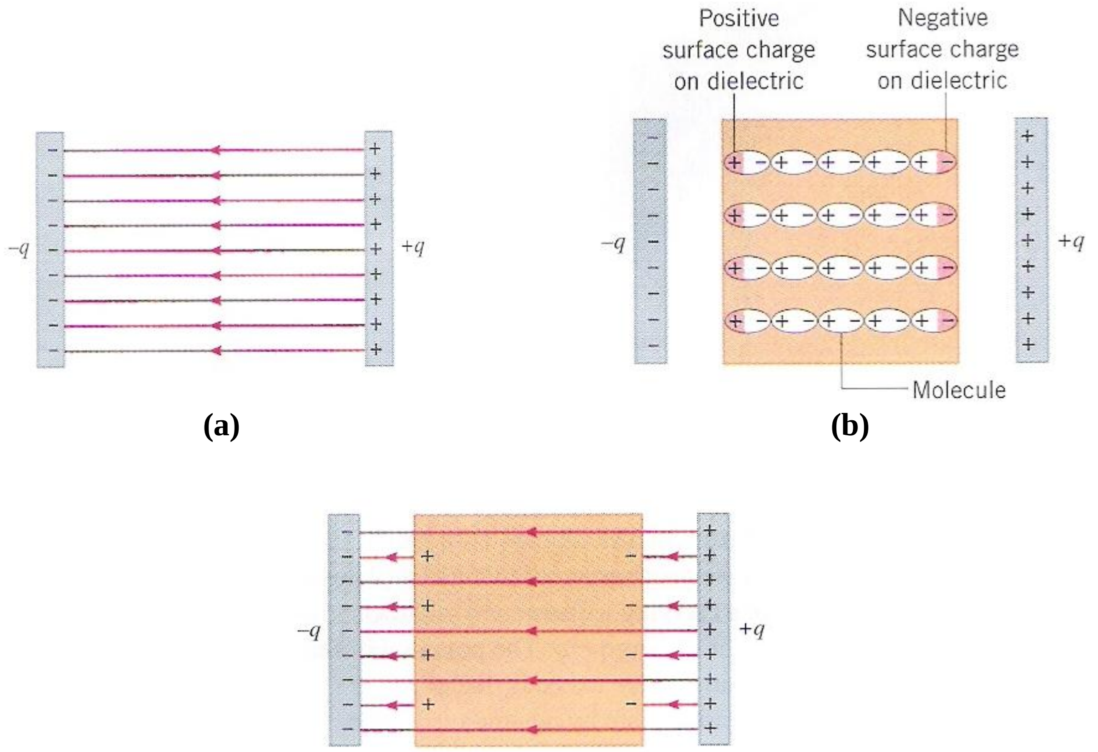

(a) **(b)**

(c)

Figure D.1: Schematic of the effect of the electric field potential by the insertion of a dielectric. Obtained from (Cutnell. J, 1998)

The electric field expression between a parallel plate capacitor can also be described as:

$$E = \frac{\sigma_c}{\varepsilon_o} = \frac{q}{\varepsilon_o A_p} \tag{D.3}$$

where σ_c is the magnitude of surface charge density on either plate, ε_o is the permittivity of free space (i.e. a vacuum), and A_p is the area of each plate. Since the electric field of a parallel plate capacitor in vacuum is $E_o = q/(\varepsilon_o A_p)$, it follows that $q/(\kappa\varepsilon_o A_p) = V/d$, which when solved for q yields:

$$q = \left(\frac{k\varepsilon_o A_p}{d}\right) \cdot V \tag{D.4}$$

A relationship of this expression with $q = CV$ substituted in Eqn. D.4 reveals that the capacitance is:

$$C = \frac{q}{V} = \varepsilon_o \frac{A_p}{d} \tag{D.5}$$

Capacitance has units of coulomb per volt $(C \cdot V^{-1})$ where $1\,(C \cdot V^{-1})$ is equal to 1 farad, F. A significant amount of fringing of the electric field lines may occur at the edges of the electrodes. Fringing occurs when the electric field travels outside the space between the electrodes. This phenomenon may be eliminated by maintaining the distance between the electrodes small relative to the electrode dimensions. As stated earlier, the dielectric constant, κ is the ratio of E_o to E. The dielectric constant can also be expressed as the ratio of the measured capacitance C to C_o where C_o is the capacitance of the capacitor in vacuum.

An additional occurrence which could also occur in parallel plate capacitive sensors is induced charges on the plates. Due to the reduction in the potential difference between the plates as discussed earlier, induced charges may occur on the opposite sides of the dielectric. This is assuming that no charge has “leaked off” the electrodes. In close proximity of the positively charged electrode, induced negative charges will emerge. In close proximity of the negatively charged electrode, induced positive charges will also emerge. This is very important when considering water molecules or other materials which are polarized. In various materials (e.g. water), the molecules contain permanent dipole moments. A dipole moment exist, due to one end of a molecule having an significant overload of negative charges while the opposing end has an significant overload of positive charge. When these molecules are present in proximity of the charged plates, an attraction of polarity of both plates takes place. As a result, the dipolar molecules are likely to adjust themselves back-to-back, as shown in part b of Figure D.1.

Regardless of whether a molecule posses a permanent dipole molecule, the electric field may cause the electrons to shift positions within a molecule, forcing one end to be slightly negative and the opposing end slightly positive. Once again, the result is similar to that in Figure D.1b. Due to the end-to-end orientation, the left surface of the dielectric becomes positively charged, and the right surface becomes negatively charged. The charge surfaces are shown in red. In the past, alternating charge/discharge circuits have been used to eliminate this effect. Advanced commercially available impedance amplifiers capable of measuring capacitance are now available which have proven to be more immune to stray capacitance and fringing effects. These amplifiers are used for high resolution capacitive sensing techniques. However electrode geometry can have an effect on stray capacitance and fringing effects.

APPENDIX E

VOID FRACTION SENSOR DESIGNS

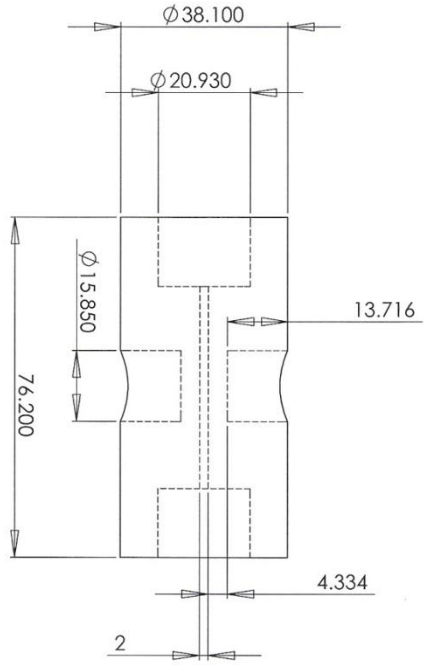

All dimensions are in (mm)

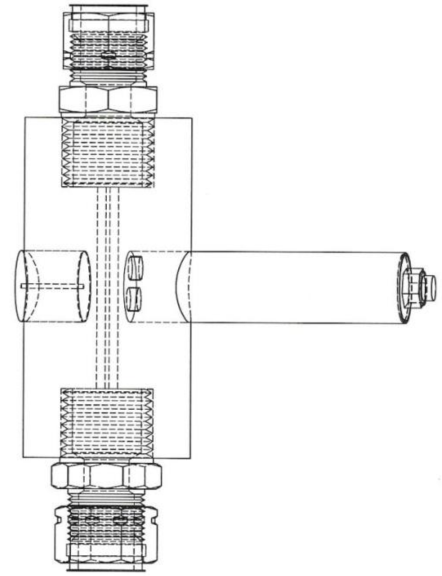

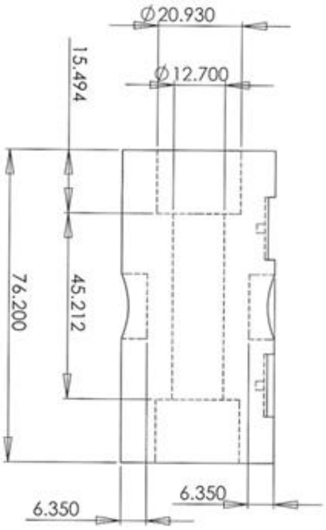
Ø20.930
Ø12.700
15.494
45.212
76.200
6.350
6.350